Doctoral theses at NTNU, 2022:155

Leon Li

In the wake of turbulence

A study on the effects of freestream turbulence on the flow around simple and complex geometries

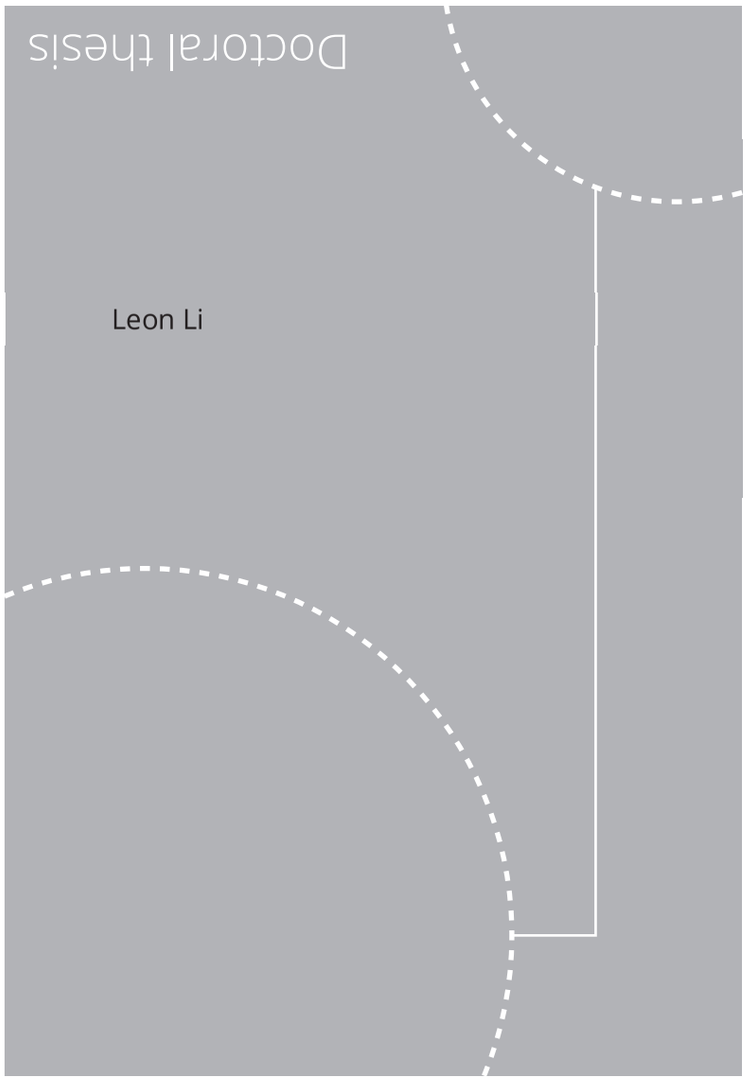

ISBN 978-82-326-5477-2 (printed ver.)
ISBN 978-82-326-6035-3 (electronic ver.)
ISSN 1503-8181 (printed ver.)
ISSN 2703-8084 (electronic ver.)

NTNU
Norwegian University of
Science and Technology

NTNU
Norwegian University of
Science and Technology
Thesis for the degree of
Philosophiae Doctor
Faculty of Engineering
Department of Energy and Process Engineering

Doctoral theses at NTNU, 2022:155

NTNU
Norwegian University of
Science and Technology

Doctoral theses at NTNU, 2022:155

NTNU

Leon Li

In the wake of turbulence

A study on the effects of freestream turbulence on the flow around simple and complex geometries

Thesis for the degree of Philosophiae Doctor

Trondheim, May 2022

Norwegian University of Science and Technology
Faculty of Engineering
Department of Energy and Process Engineering

NTNU
Norwegian University of
Science and Technology

NTNU
Norwegian University of Science and Technology

Thesis for the degree of Philosophiae Doctor

Faculty of Engineering
Department of Energy and Process Engineering

ISBN 978-82-326-5477-2 (printed ver.)
ISBN 978-82-326-6035-3 (electronic ver.)
ISSN 1503-8181 (printed ver.)
ISSN 2703-8084 (electronic ver.)

Doctoral theses at NTNU, 2022:155

PRINTED IN NORWAY
NO - 1598

NORDIC SWAN ECOLABEL
Printed matter
2041 0731

Printed by Skipnes Kommunikasjon AS

Abstract

With the growing demand of global energy consumption and a need to reduce pollution caused by energy production from fossil fuels, renewable sources of energy are becoming increasingly necessary for the future sustainable development of our society. Wind energy offers an attractive option as one of the renewable sources, and a large body of work is currently ongoing to widen its implementation. This thesis seeks to contribute to this growing body through experimental investigations into how turbulent flows interact with wind turbines, both in part and in whole, and from that, gain insights into how the interactions impact their performance. The complex and turbulent environment of atmospheric boundary layers, in which wind turbines operate, presents an intriguing challenge. The work is divided into three main investigative topics: the spatial development of a turbulent boundary layer under decaying freestream turbulence, the effect of freestream turbulence on the performance of a wind turbine airfoil, and lastly, the near-field of a model wind turbine under turbulent shear flows.

The first investigation examined how a turbulent boundary layer evolves in the streamwise direction under the influence of decaying freestream turbulence. The experiment was performed in the new water channel facility at the Norwegian University of Science and Technology. The objective was to gain insight into the physics of a representative background flow that can be expected for wind turbines. Laser Doppler velocimetry was used to characterize both the freestream turbulence and the boundary layer. The main finding is that the effects of decaying freestream turbulence on the properties of the turbulent boundary layer diminish as they co-evolve downstream. This is reflected in both the behaviour of the wake region in the boundary layer, as well as the peak in the velocity fluctuations near the wall.

The second set of experiments looked into how freestream turbulence affects the

pressure and lift characteristics of a wind turbine airfoil. Pressure distributions are taken at different angles of attack and for different incoming turbulence intensities. It is found that increasing the freestream turbulence intensity generally increases the maximum lift for this airfoil, but it does not noticeably change the stall angle. Lift within the linear operating range also shows improvement with increasing turbulence intensity. However, for low turbulence intensities, a decrease in lift in the linear region is observed. Further analysis into the pressure fluctuation spectra near the trailing edge reveals the presence of periodic pressure fluctuations for these cases.

Lastly, moving from the component to the system level, a model wind turbine was placed in different turbulent shear flows generated by an active grid. Particle image velocimetry was used to capture the near-field around the model. It was found that the near-wake velocity deficit can be decomposed into a velocity deficit profile caused by a uniform inflow plus the incoming shear profile. The combined profile shows higher shear gradient on the high-velocity side of the incoming shear flow, and this in turn leads to higher turbulence production and thus higher velocity fluctuations. The turbine power fluctuations were found to be proportional to turbulence intensity, regardless of the shear profile, and the kinetic energy available in the flow for downstream turbines was also found to be mainly dependent on the incoming turbulence intensity.

Overall, this thesis examines the influence of turbulent flows on a wind turbine from the perspective of the background flow level, the component level, and lastly, the system level. The work provides new insights into how these three levels are affected by the presence of turbulence, and it is the hope of the author that it will contribute meaningfully to the field of wind energy and turbulence research, and become a building block upon which other works can be advanced upon.

Dedication

To my maternal grandfather Shi Xiaode:
though not possessing a formal engineering degree,
you possess an engineering prowess that no pieces of paper can convey.

Preface

This thesis is submitted to the Norwegian University of Science and Technology (NTNU) for partial fulfilment of the requirements for the degree of philosophiae doctor. The doctoral work has been carried out in the Thermo Fluids Group at the Department of Energy & Process Engineering (EPT), from February 2018 until March 2022. The research work has been supervised by Associate Professor R. Jason Hearst and Associate Professor Nicholas Worth.

The project was funded by the Department of Energy & Process Engineering at NTNU.

This thesis consists of three chapters and three scientific articles. Motivation and background information are provided in Chapter 1, while Chapter 2 describes the experimental facilities and methods. Chapter 3 summarizes the three research articles, which are included in full text at the end of the thesis. All three research articles have been published in peer-reviewed journals. They are:

Article I
Spatial development of a turbulent boundary layer subjected to freestream turbulence
Yannick Jooss, Leon Li, Tania Bracchi and R. Jason Hearst
J. Fluid Mechanics, Volume 911, A4, 25 January 2021

Author contributions: YJ, LL, and RJH conceived of the idea for this work. LL designed and constructed the active grid, and was responsible for the construction and commissioning of the new water channel. LL generated the active grid actuation protocols. YJ conducted the experiments with help from LL. YJ performed the analysis and was the primary author of the manuscript with support from TB and RJH. All authors read and contributed to the manuscript.

Article II

The influence of freestream turbulence on the temporal pressure distribution and lift of an airfoil

Leon Li and R. Jason Hearst

J. Wind Engineering & Industrial Aerodynamics, Volume 209, February 2021

Author contributions: LL and RJH conceived of the idea for this work. LL conducted the experiments, performed the analysis, and was the primary author of the manuscript with support from RJH. RJH supervised the project. All authors read and contributed to the manuscript.

Article III

The near-field of a lab-scale wind turbine in tailored turbulent shear flows

Leon Li, R. Jason Hearst, Manuel A. Ferreira and Bharathram Ganapathisubramani

Renewable Energy, Volume 149, April 2020

Author contributions: BG and RJH conceived of the idea for this work. MAF designed the model turbine. RJH conducted the experiments with help from MAF. LL performed the analysis and was the primary author of the manuscript with support from RJH. All authors read and contributed to the manuscript.

Acknowledgement

During my master's studies, I told myself that I would never ever do a PhD. And yet here I am, nine years later, completing my doctoral degree, and I would be amiss if I do not express my gratitude to everyone who has helped me along the way.

First and foremost, I would like to thank my main supervisor, Associate Professor R. Jason Hearst. I knew Jason when he was a PhD student himself at the University of Toronto. Even from that time, he was supporting and guiding me in my own studies for a master's degree. This fortunately continued when he took me on as his first PhD student. From day one, Jason has provided guidance and support in his usual welcoming and humorous manner, not only for my research project, but also for taking care that I transition well into life in Norway. The past four years of my PhD degree has been some of the greatest times of my life, and I thank Jason for making that happen in the first place. I would also like to thank my co-supervisor Associate Professor Nicholas Worth, as well as Professor James R. Dawson, for putting the lab together all those years ago and for providing a nurturing and supportive environment for research.

I would like to thank the technical staff at EPT, Bård Aslak Brandåstrø, Trygve Opland, Arnt Egil Kolstad, Halvor Haukvik, Sander Kvernmo, Stein Kristian Skånøy, Sondre Hoelstad Nubdal, Kent Andre Ross, Bjørn Selnes-Volseth, Eugen Uthaug, Morten Grønli, and Per Bjønaas, who have helped me immensely with setting up the facilities and experiments. This PhD would not have been possible without their work and expertise.

The fluids group would not be the fluids group without all the great people in it. Magnus, Olav, Yannick, and Masoud, you guys simply made life in this group rock! All the Fluids Bowls and other outings provided much needed respite from the days in the lab, and yet at the same time, lab days are filled with laughter when you guys

are around. A special shout-out to Yannick and Masoud, who once helped me out of a “tight” situation in the water channel. I would also like to thank the post-docs in the fluids group, Zaman, Pim, and Ingrid. For however long you have worked with me, I thank you for your support in and outside of the lab. Special thanks to Pim and Yannick for all the ~~regrettable~~ unforgettable off-piste skiing experiences.

To all the other friends I’ve made at work over my PhD years, Dirren, Yi Hao, Loïc, Marek, Ben, Jackie, Eirik, Andreas, Thomas, Anna, Håkon, Øyvind, Melissa, Girish, Srikar, Elena + Rafael, Sam + Maddy, Frida: you guys are the reasons why the past four years have been the best years of my life so far. Too many memories and anecdotes to reminisce, so I’ll just leave it here.

A special thanks to my two long term flatmates at Persaunet, José and Philip. As amazing as that house was, you guys injected life and soul into that place and made it something else entirely. All the shenanigans we did around the house, the BBQing, the parties, the cooking (for one of us it was attempted cooking), or just relaxing on the couch, their memories will stay with me.

To the Hefley family - Daniel, Signy, Calem, Emma Joy, and Mikayla, as well as Oddmund and Leah: you have formed a family for me away from Canada, and have walked with me through the hills and the valleys of my time here. I am truly blessed to have you in my life. Also a very big gratitude to the entire Gustad clan, who have warmly invited me to your homes for two Christmases when I couldn’t go back to mine. You have made me feel like I wasn’t really missing home for those days. And of course this part would not be complete without a big shout-out to Stefan Williams and all the Chinese food we cooked up together!

To my friends back in Canada and the US, even though it was sad to leave you four years ago, you have nevertheless not ceased to support me. To Hannah, Curt, William + Sally, Matt, Dave, Jeff, John, Rosary, Brandon, Deanna, Monica, Jason, Steve, Tiff, Linh, Jim + Bev, Ye: all of you have been with me for so many years through the thick and thin. And there are so many others that I can’t realistically name all of you here, so I say sorry in true Canadian fashion!

Before thanking my family, I would like to quickly acknowledge Pizzabakeren Nedre Singsaker for providing sustenance for all those long lab days, and of course for the unforgettable twelve free pizzas that I won. Also thanks to all of you who have shared a *nr. 22 Chorizo Spesial* with me.

So at last to my family, words escape me so I will simply say thank you for raising me to be the man I am today, across three continents. Couldn’t have gotten here without you. And if I can be half as good to my own family in the future as you have been to me, I would count myself to have lived well.

Contents

Chapter 1

Introduction

1.1 Motivation

As we advance in the development of our society, increasing global energy consumption is unavoidable. From the earliest days, we have taken elements from the Earth to extract usable energy, whether it be making fire for warmth, or powering a mill with wind or water. Ever since the first industrial revolution, the development of energy production has grown drastically to meet the rapidly growing energy demands of the collective industrial machines. At first, these developments were focused purely on energy production efficiency and quantity, with no regard towards their environmental impact. However, as we became more aware of the detrimental effects unrestrained energy production has on our planet, greener and more sustainable energy sources have become increasingly necessary. It is estimated that by the year 2050, the global annual electricity demand will be more than 38,000 TWh (terrawatt-hours), compared to 25,000 TWh in 2017 (Veers et al. 2019). Such development would put emphasis on the demand for greener energy generation methods. Wind energy is an attractive option as a renewable energy source. This project wishes to contribute to this growing field of research as the world moves towards more sustainable and renewable energy sources. Veers et al. (2019) identified three grand challenges in the future development of wind energy research:

1. "Improved understanding of atmospheric and wind power plant flow physics"
2. "Aerodynamics, structural dynamics, and offshore wind hydrodynamics of enlarged wind turbines"
3. "Systems science for integration of wind power plants into the future electricity grid"

Similarly, van Kuik et al. (2016) presented eleven challenges in wind energy research, the first three of which are material and structures, wind and turbulence, and aerodynamics. Both of these reviews have identified the flow physics around wind turbines and wind farms within the top three challenges, and it is clear that much work still needs to be done on them. The review by Porté-Agel et al. (2020) specifically lists the need for further investigations into the nature of atmospheric boundary layers (ABL) and their interactions and effects on the operations of wind turbines and wind farms. Therefore, the practical application and motivation of this project is to investigate the interaction of turbulent flow phenomena with the flow physics around wind turbines in an effort to contribute to these challenges.

The fact that turbulence is ubiquitous in nature adds an additional dimension of complexity to wind energy research. At its core, the problem of turbulence is one of chaos, where the instantaneous flow field at any given point in time and space are highly dependent on the initial and boundary conditions. The system is chaotic to such a degree that it is impossible, in an experimental setting, to reproduce an exact temporal and spatial replica of a turbulent flow field. Turbulence is considered the hardest unsolved problem in classical physics, and this is reflected by the fact that the proof for the existence and smoothness of the governing equations, the Navier-Stokes Equations, constitutes one of the seven Millennium Prize Problems. Perhaps the most succinct summary of the fiendishly elusive nature of turbulence is the possibly apocryphal quote attributed to both Werner Heisenberg, the father of quantum mechanics, and Horace Lamb, the British applied mathematician, and it goes to the effect of "when I die and meet God, I would like to ask for enlightenment on two questions. Why relativity (or quantum electrodynamics)? And why turbulence? About the former I am quite optimistic."

While this project is not ultimately about the fundamentals of turbulence, it nevertheless provides an intriguing and motivating challenge. Incorporating turbulence research into the topic of wind energy flow physics is necessary as that is a more realistic representation of what is found in the real world. It is the need to advance wind energy development, combined with the challenges that turbulence presents, that provides the motivation for this work.

1.2 Background

The following section summarizes the historical research as well as some of the outstanding questions relevant to this project. As mentioned in the previous section, this project seeks to focus on the effect of turbulence on topics related to wind turbines. Therefore, it is logical to first examine the type of background flow that wind turbines experience, namely atmospheric boundary layers, which in itself is an extremely complex collection of different flows that are highly dependent on the

Figure 1.1: Leonardo da Vinci, movement of water, 1507-9. Windsor, Royal Library, 12660v.

local conditions (Wagner et al. 2009). This ties well into our experimental facility, which has the ability to tailor the turbulent inflow properties. It is important to understand how these flows influence the boundary layer and thus the usable region of the flow for wind turbine applications. At the same time, it gives us insight into some of the fundamentals of the interactions between freestream turbulence and boundary layers. It then follows to examine the effect of turbulence on arguably one of the most important aspects of a wind turbine, namely the design of the blade cross section. Finally, we will look at the development of turbulent shear flow research in experimental settings and how such flow in the real world impact the performance and operation of wind turbines and wind farms.

1.2.1 Turbulence & Grid Turbulence Research

As mentioned before, the study of turbulence forms one of the most challenging topics in classical physics because of its chaotic nature. Qualitatively, turbulence exhibits flow structures of different sizes. These structures take on the form of eddies, or "whorls", in the flow (Richardson 1922), and these eddies interact with each other in a chaotic manner. This is in contrast to laminar flow, where no such structures are found and the flow field is smooth and predictable. An early observation of turbulent structures is a sketch by Leonardo da Vinci of a stream of water flowing out of a duct and down into a reservoir (figure 1.1), where eddies of different sizes can clearly be seen. In the famous experiment of Reynolds (1883), differences between laminar and turbulent flows were observed through examining the flow pattern of a stream of dye in water flowing in a glass pipe. The flow rate through the pipe was varied to produce, in the dye stream, what is now known

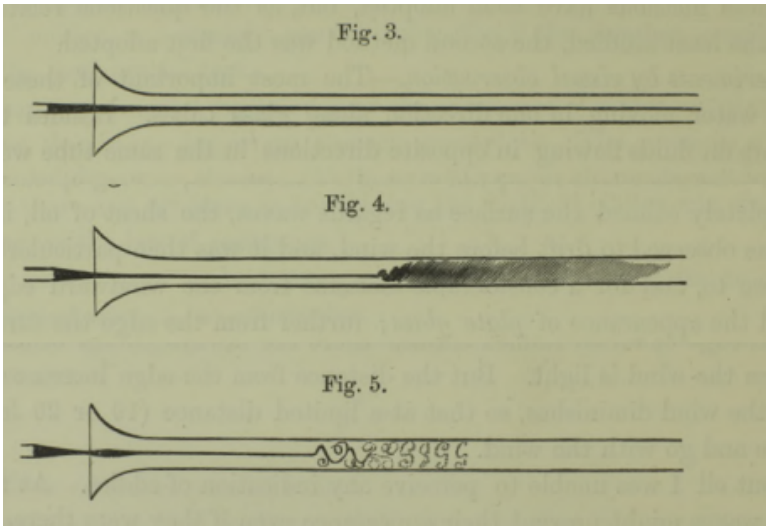

Figure 1.2: Sketches of dye streams showing (*Fig. 3*) fully laminar flow; (*Fig. 4*) laminar-turbulent transition; (*Fig. 5*) quasi-instantaneous snapshot of the turbulent structure illuminated by electrical sparks. Taken from Reynolds (1883).

as laminar-turbulent transition. Figure 1.2 shows the sketches made by Reynolds of his observations of the behaviour of the dye streams. Of particular interest is the last figure, where he used an electrical spark to illuminate the flow to provide quasi-instantaneous snapshot of the flow structures. One can again clearly observe eddies of different sizes forming after the transition point.

Richardson (1922) famously summarized the relationship between these eddies in the poetic verses:

Big whorls have little whorls
That feed on their velocity,
And little whorls have lesser whorls
And so on to viscosity.

All of the aforementioned examples only describe the structures of turbulent flows qualitatively. The verses by Richardson introduced the idea that these eddies (or whorls) break down into smaller ones until they reach a scale where further breakdown is no longer possible and they simply dissipate into heat due to the intrinsic viscous properties of the fluid. In the process of eddy breakdown, the turbulent kinetic energy in the flow is also transferred from the largest to the smallest eddies. This is referred to as the energy-cascade.

Before we go further into the energy cascade, we will introduce some important concepts. The first is Reynolds decomposition of velocity. The velocity in a turbulent flow can be considered as a superposition of a time-averaged component and a fluctuating component, namely $u_i = U_i + u_i'$. Here u_i is the velocity, U_i is the time-averaged mean of u_i, and u_i' is the fluctuating component. Note that Einstein's notation is used here, where the index i represents the three spatial axes x_1, x_2, and x_3. The turbulent kinetic energy mentioned in the previous paragraph is then defined as $k = \frac{1}{2}\langle u_i' u_i' \rangle$, where $\langle \cdot \rangle$ represents a time-averaged quantity. We will also introduce the concept of the dimensionless Reynolds number, which is defined as $Re = \mathcal{U}\mathcal{L}/\nu$, where $\mathcal{U}$ and $\mathcal{L}$ are the velocity and length scale respectively, and ν is the kinematic viscosity of the fluid. The Reynolds number represents the ratio between inertial and viscous forces in a fluid, and is an important parameter for characterizing how "turbulent" is the flow. Lastly, we define the turbulence intensity to be $\langle u_1'^2 \rangle^{1/2}/U_0$, where U_0 is the freestream velocity, and a length scale called the integral length scale, which is representative of the size of the largest eddies. It is defined as

$$L_{ij} = \int_0^{r_0} \frac{\langle u_i'(x_j) u_i'(x_j + r) \rangle}{\langle u_i'^2 \rangle} \mathrm{d}r, \tag{1.1}$$

where r_0 is the first zero crossing of the auto-correlation function $\langle u_i'(x_j) u_i'(x_j + r) \rangle$.

The groundwork of Kolmogorov (1941a) built upon the idea of this energy-cascade introduced by Richardson, and provided a mathematical model for this process. The model describes the amount of turbulent kinetic energy contained by eddies of different sizes. This can be better explained by looking at a spectrum of the velocity fluctuations. Figure 1.3 shows one such example, plotting the normalized energy spectra against $\kappa_1 \eta$, where κ_1 is the wavenumber, which is inversely proportional to the physical size of the eddies, and η is the Kolmogorov length scale, which is representative of the size of the smallest eddies. It is defined as

$$\eta = \left(\frac{\nu^3}{\epsilon} \right)^{1/4}, \tag{1.2}$$

where ϵ is the mean dissipation rate of turbulent kinetic energy, which is in turn defined as

$$\epsilon = \nu \left\langle \frac{\partial u_i'}{\partial x_j} \frac{\partial u_i'}{\partial x_j} \right\rangle. \tag{1.3}$$

The plateau region with low wavenumbers represents the energy containing range, where the largest scale structures exist. The region with high wavenumbers, near $\kappa_1 \eta = 1$, represents what is known as the dissipation range, where the smallest eddies dissipate their kinetic energy into heat due to viscosity. In between these two

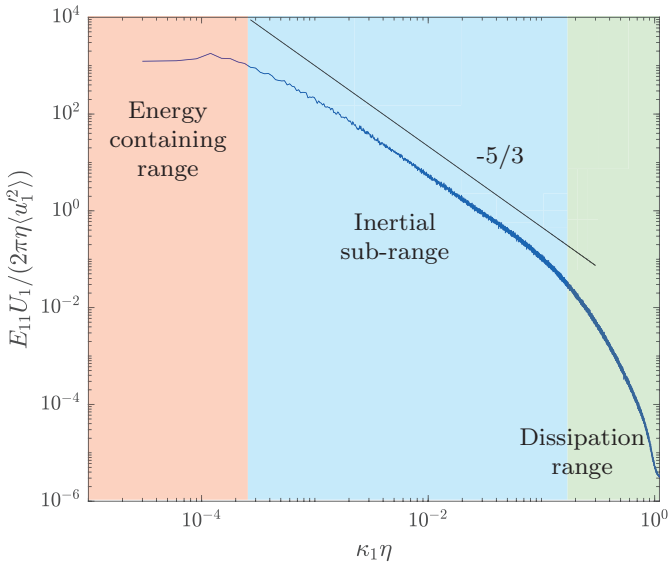

Figure 1.3: An example of the velocity fluctuation energy spectra, showing the energy-containing range, the inertial sub-range, and the dissipation range. The black solid line denotes a slope of -5/3.

regions there exists a third region called the inertial sub-range, where the turbulent kinetic energy is cascaded down from the larger eddies to the smaller ones. The slope of the spectra is predicted to be $-5/3$ for this region by dimensional analysis based on Kolmogorov's hypothesis (Kolmogorov 1941a), as indicated by the black line in the figure.

The predictions of Kolmogorov (1941a) require the flow to be "sufficiently turbulent" such that a separation of scales exists. To quantify how turbulent a flow is, we introduce another concept called the Taylor micro-scale, denoted λ. This quantity will be defined later, but for now it can be understood as an intermediate length scale between the largest scales and η, residing in the inertial sub-range. The corresponding Reynolds number based on λ is $Re_\lambda = \langle u_1'^2\rangle^{1/2}\lambda/\nu$. This quantity can be used as an indicator of how "turbulent" the flow is, with higher values denoting more turbulent flows. The predictions of Kolmogorov (1941a) assume that Re_λ is infinite. While this is not readily achievable in simulations or laboratory flows due to their respective limitations, but if Re_λ is sufficiently high, the predictions should be approached asymptotically. This motivates an area of turbulence research called homogeneous isotropic turbulence (HIT), which is the simplest form of turbulent flow. Homogeneous means that the turbulence statistics are invariant in space (e.g., no shear flow), while isotropic means that the velocity fluctuations $\langle u_i'^2\rangle^{1/2}$ are

equal in all directions (i.e. invariance of rotations of the coordinate system). It is also postulated that the initial conditions for generating turbulence are sufficiently removed from the turbulence itself in space and/or time such that they play no significant role on its subsequent development. In other words, the turbulence does not "remember" how it was made.

Grid turbulence has been popular with experimentalists trying to create close approximations of HIT. In its simplest form, these grids consist of bars placed somewhere in the test section of a experimental facility, typically at or near the inlet. The bars perturb the flow, creating wakes. The wakes then develop and mix with each other downstream of the grid. At a certain distance behind the grid, the mixing produces relatively homogeneous and isotropic turbulence in transverse planes, which then decays as the flow propagates farther downstream. Within the homogeneous region, there is no production of turbulent kinetic energy because there is no shear, which means that, in grid turbulence, the turbulent kinetic energy transport equation reduces to

$$U_1 \frac{\partial k}{\partial x_1} = -\nu \left\langle \frac{\partial u_i'}{\partial x_j} \frac{\partial u_i'}{\partial x_j} \right\rangle . \tag{1.4}$$

The flow in grid turbulence is assumed to be statistically stationary in the far wake, and Taylor's frozen flow hypothesis[1] is invoked to transform time-domain terms into spatial-domain terms. We shall refer to this class of grids, where the bars are static, as passive grids hereafter.

There are two major design parameters for passive grids, the grid mesh length, typically denoted as M, which is the separation between each bar measured from centre to centre, and the solidity σ, which is the ratio of solid blockage to the total cross sectional area of the grid. Studies have also indicated the shape of the bars plays a role in the produced turbulence (e.g., Lavoie et al. 2007), but this is not a focus here. The solidity can be calculated from the mesh length and the bar diameter, d, via

$$\sigma = 1 - \frac{(M-d)^2}{M^2}.$$

Figure 1.4 is a schematic of a typical passive grid element, showing M and d.

Passive grids have the advantage of simplicity and the ability to produce homogeneous turbulent flows with relatively low degrees of anisotropy, where anisotropy is defined as the ratio between the streamwise and the spanwise velocity fluctuations, namely u_1'/u_2' and u_1'/u_3'. However, it has the drawback of limited Reynolds number

[1] Taylor's frozen flow hypothesis states that a transform can be made between space and time, via $x \sim tU_0$.

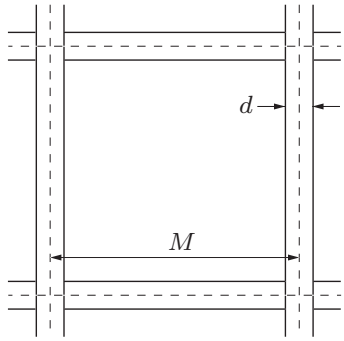

Figure 1.4: Schematic of a generic passive grid element, showing the mesh length M and the bar diameter d. The dotted lines denote the centreline of the bars.

Re_λ, where λ is defined as

$$\lambda = \left[5\nu\frac{q^2}{\epsilon}\right]^{1/2}, \tag{1.5}$$

and $q^2 = \langle u_i' u_i' \rangle$. Here, the turbulence is assumed to be homogeneous and isotropic. Under this assumption, eq. 1.3 becomes

$$\epsilon = 15\nu \left\langle \left(\frac{\partial u_1'}{\partial x_1}\right)^2 \right\rangle. \tag{1.6}$$

We will now look at some selected studies from the perspective of anisotropy and Re_λ achieved to see how well they have approximated high Reynolds number HIT. Comte-Bellot and Corrsin (1966) carried out hot-wire measurements in a wind tunnel for three different passive grids. A secondary contraction was used and each grid was made in two sizes, for upstream and downstream of the secondary contraction. The anisotropy u_1'/u_2' decreases with respect to tU_0/M within the experimental domain of $20 < tU_0/M < 400$. However, it does not reach unity, settling around 1.05 to 1.10 near the end of the measurement domain. Note that here tU_0/M is used to denote the normalized distance downstream of the grid instead of the more straightforward x_1/M because it allows direct comparison between results for data taken with and without the secondary contraction. Here t is the elapsed time, which is calculated from

$$t = \int \frac{\mathrm{d}x_1}{U_1(x_1)}.$$

When the secondary contraction is in place, the flow is much more isotropic for all test cases, with u_1'/u_2' between 0.95 and 1.05. The authors did not report the Re_λ

for their flow cases, and no energy spectra were shown to check for the existence of an inertial sub-range.

A subsequent study of a grid instrumented with jet injection nozzles by Gad-El-Hak and Corrsin (1974) produced an energy spectra that had limited inertial range ($Re_\lambda \sim 100$), and the validation of the $-5/3$ prediction is not conclusive. However, the u_1'/u_3' anisotropy was around 1.05, while the u_1'/u_2' anisotropy was around 1.15, which is comparable to passive grid values. This suggests that the initial conditions of turbulence generation have less effect on the turbulence properties as Re_λ increases, as Gad-El-Hak and Corrsin (1974) used a grid with jet injection capabilities as opposed to the simple passive grid used by Comte-Bellot and Corrsin (1966). Furthermore, no peculiar behaviour was found when the jet grid was operated at different injection directions (against the mean flow vs. with the mean flow) or injection rates, providing more evidence for the diminishing effects of initial conditions as Re_λ increases.

In a more recent effort, an extensive campaign by Lavoie et al. (2007) investigated the effect of initial conditions on turbulence characteristics. Four different bi-planar passive grids were used, with different bar shapes (round & square) and grid solidity. As with Comte-Bellot and Corrsin (1966) and Gad-El-Hak and Corrsin (1974), a secondary contraction was employed to improve the flow isotropy. The addition of the secondary contraction reduced u_1'/u_3' from around 1.2 to around 1.1. However, Re_λ for this particular study is in the low range, around 40 for all cases.

In an effort to increase Re_λ, Carter et al. (2016) used a random jet array to create zero-mean turbulent flows. Reaching a $Re_\lambda \sim 400$, they found good approximation in the inertial range with the $-5/3$ law. This was made at the cost of relatively high anisotropy values, with u_1'/u_2' ranging from 1.35 - 1.75. Although this study is not a grid turbulence experiment, it is included here to show that as Re_λ increases, we do get closer approximations to the $-5/3$ law predicted by Kolmogorov (1941a).

Overall, passive grids offer a promising start in the field of HIT research. Although they are limited in terms of the turbulence intensity, and thus the Re_λ that they can achieve, passive grids nonetheless offer turbulent flow with good isotropy, and have shown, at least qualitatively, that as Re_λ increases, the effect of initial conditions diminish and the inertial sub-range expands, increasing the size of the region where the spectra exhibits a slope of -5/3, consistent with the predictions of Kolmogorov (1941a). As an aside but adding strong evidence for the proposed energy cascade process, Cardesa et al. (2017) performed Direct Numerical Simulation (DNS) on box turbulence and observed the actual breakdown of turbulent eddies from larger sizes to smaller ones. The preferred mode of breakdown is one eddy breaking down into two eddies of similar size. This breakthrough allows us to proceed with more

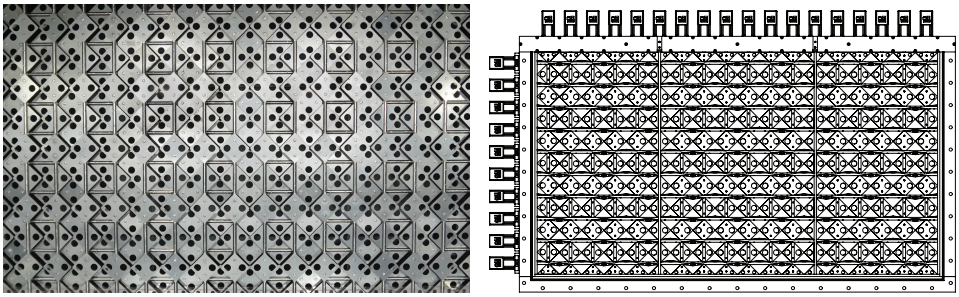

Figure 1.5: An image (left) and the schematic (right) of the active grid installed in the new water channel facility at NTNU Gløshaugen. This is viewed from the test section looking upstream, with the active grid at full blockage. These images are also available in *Article I*.

confidence as we search for better ways of increasing the turbulence intensities and Reynolds number produced in an experimental setting.

A major breakthrough in grid turbulence research was the advent of the active grid. First popularized by the seminal work of Makita (1991), active grids are, in short, bars with agitator wings on them, which are actuated by motors in a controlled manner. The actuation algorithm controls the rotational velocity, acceleration, duration, and direction of each motor. Figure 1.5 shows an image and a schematic of the active grid installed in the new water channel facility at NTNU Gløshaugen.

An active grid has the ability to create turbulent flows with very high Re_λ compared to passive grids, and more importantly, this can be achieved in a moderately sized experimental facility (the test section utilized by Makita (1991) only measures 0.7 m $\times$ 0.7 m $\times$ 6 m). Thus, the active grid offers unprecedented access to potential exploration of high Re_λ turbulence without the need to build very large facilities. Furthermore, the $Re_\lambda = 387$ achieved by Makita (1991) was an order of magnitude larger than all the previous work at that time except those of Kistler and Vrebalovich (1961). The main drawback of active grids is the higher values of anisotropy. Makita (1991) reported $u_1'/u_2' \approx 1.22$.

Figure 1.6 shows two example velocity fluctuation spectra to highlight the extended inertial sub-range created by the active grid. One can see that in figure 1.6(b), the active grid is able to produce an inertial sub-range with a slope of approximately $-5/3$ for over two decades of the wave number range, while the spectra from a passive grid (figure 1.6(a)) shows a shorter inertial sub-range. The corresponding turbulence intensities of the two cases shown in figure 1.6 are approximately 5.4% for the passive grid and 16.0% for the active grid. These spectra are generated from our own measurements conducted with constant temperature anemometry, the details of which will be addressed in Section 2.2.

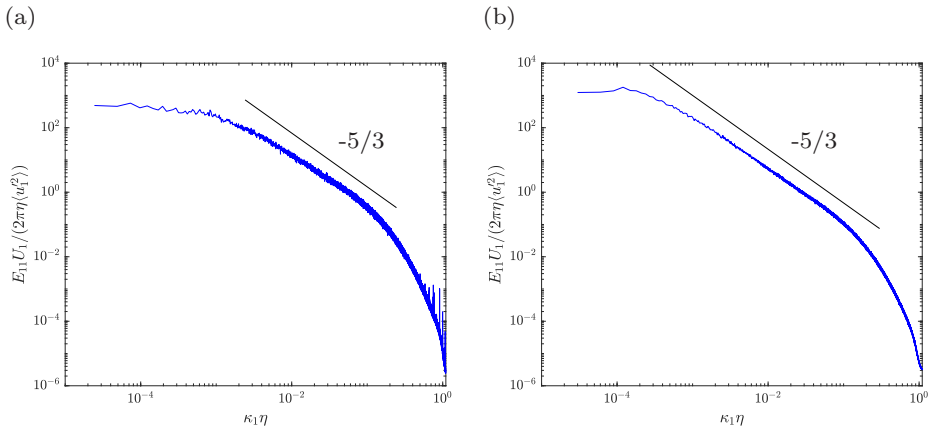

Figure 1.6: A comparison of the velocity fluctuation spectra between turbulent flows generated by (a) a passive grid, and (b) an active grid. The data are original constant temperature anemometry measurements.

Mydlarski and Warhaft (1996) used an active grid similar to that of Makita (1991) in a wind tunnel to investigate the dependence of turbulence statistics on Re_λ. Re_λ was varied between 99 and 473 by varying the freestream velocity. Both the u_1' and u_2' spectra show lengthening of the inertial sub-range with increasing Re_λ. However, even at the highest Re_λ reached, the slope is still below -5/3, at -1.58. Through relating the slope of the inertial sub-range to Re_λ, the authors suggested that a -5/3 scaling region (to within 0.01) will not occur until $Re_\lambda \approx 10^4$. Mydlarski and Warhaft (1996) then went on to investigate a proposed qualitative difference between 'weak' and 'strong' turbulence, defined as turbulence with $Re_\lambda < 100$ and $Re_\lambda > 200$, with the region in between being called a transitional region.

A large active grid was constructed by Larssen and Devenport (2011) in an effort to study the generation of large-scale turbulence in a systematic way. The grid measures 2.14 m × 2.14 m, and is installed in a large wind tunnel with a square cross section measuring 1.83 m on edge and 7.3 m long. The grid itself is installed in the contraction in an effort to decrease the anisotropy of the turbulence generated, much like the secondary contraction used by Comte-Bellot and Corrsin (1966). The grid consists of 10 × 10 rods each controlled independently via a stepper motor, with a mesh length M of 21.0 cm. It is operated in a double-random mode, where both the rotation speed and rotation period of each rod is randomized. This improves the homogeneity and isotropy of the flow. A parametric study is performed on how the different operating parameters affect the properties of the turbulence. These are the normalized distance from the grid (x_1/M), the grid Reynolds number (MU_0/ν), the Rossby number ($U_0/(M\Omega)$), the average number of rotations before direction

change ($T\Omega$), the normalized maximum deviation in cruise time (t/T), and the normalized maximum deviation in rotation rate (ω/Ω). Here Ω is the nominal rotation rate in Hz, T is the nominal rotation time in seconds, and t and ω are the maximum deviations in rotation time and rate respectively. The rotation acceleration α is examined on a limited basis, kept to 20 Hz/s for most of the test cases due to mechanical limitations. A total of 39 test cases were investigated, with turbulence intensities ranging from 1.9% to 12.0% and Re_λ reaching up to 1362, which was the highest level achieved in grid turbulence at the time. The placement of the active grid in the contraction, in essence having a secondary contraction after the grid, greatly improved the isotropy of the flow. In the cases tested, u_1'/u_2' and u_1'/u_3' were between 0.98 and 1.02, which was comparable to and even better than some earlier passive grid experiments. This study revealed that U_0, Ω, and α have the largest effect on the turbulence intensity. In particular, slower rotation rates (i.e. smaller Ω) generate higher turbulence intensities up to a certain point. After which the turbulence intensity plateaus with respect to smaller Ω. The effect of α works in a similar principle, as in a slower acceleration rate will prolong the time in which the wings spin relatively slowly, and thus it has a similar effect as slower rotation rates. The turbulence intensity shows a strong dependency on the grid Reynolds number, in contrast with passive grids, where the turbulence intensity is relatively constant over a range of U_0. Re_λ and the streamwise integral length scale L_{11} were found to be mostly dependent on Ω, U_0, T, ω, and possibly t. The length scales are inversely related to $T\Omega$, and positively related to ω/Ω, but only up to a certain point for the latter. It is important to note that except for Ω and U_0, the other parameters do not affect the turbulence intensity much, which means that the grid operating parameters can be used to decouple turbulence intensity from the length scales, thereby expanding the space that an active grid can explore.

Hearst and Lavoie (2015) performed an extensive parametric study on the effect of the operating parameters of an active grid on the generated turbulence properties. Their grid is a unique double-mesh design, where wings along an axis are mounted in the fore and aft meshes in an alternating pattern. This design decouples adjacent wings so that they can rotate independently, as opposed to the more traditional active grid design there wings mounted on one bar are locked to rotate together synchronously. There are 20 horizontal bars and 30 vertical bars in total, organized into two layers of 10×15 mesh. Figure 1.7 shows the dependency of turbulence intensity, Re_λ, isotropy, the Kolmogorov length scale η, the Taylor micro-scale λ, and the integral length scale L_{11} on the Rossby number and the grid Reynolds number. The results largely agree with Larssen and Devenport (2011), in that as Ω decreases and/or U_0 increases, the flow generated becomes more turbulent, as signified by the increase in turbulence intensity and Re_λ. Wing blockage was also found to be an important parameter, and that the blockage rather than the shape

of the wings appeared to be the dominate factor. There is still some degree of coupling between the turbulence intensity and the integral length scale, however, in figures 1.7(a) and 1.7(f), one can see regions of operating parameters where the integral length scale is relatively constant, while the turbulence intensity changes significantly, and vice versa. These regions appear to be along the lines of the lowest grid Reynolds number and the lowest Ω.

In addition to high Reynolds number grid turbulence research, active grids can also generate highly-tailored inflow conditions to, for instance, closely resemble the atmospheric boundary layer in which wind turbines operate. Knebel et al. (2011) generated highly intermittent turbulent wind fields through the use of an active grid in a wind tunnel, and Neunaber et al. (2021) studied the effects of continuous and intermittent turbulent inflows on the wake development behind a wind turbine. Active grids have been used in turbulent shear flow research for applications to atmospheric boundary layer studies, and this will be covered later in Section 1.2.4.

Overall, both the classical passive grids and the more advanced active grids have been used extensively in the field of experimental turbulence research to create close approximations to homogeneous, isotropic turbulence and customized inflows. These devices form the foundation for this project in generating the necessary flow conditions in order to study the effect of turbulence on topics related to wind energy and beyond, which will be covered in the next sections.

1.2.2 The effects of freestream turbulence on turbulent boundary layers

Ever since the concept of boundary layers was introduced by Prandtl (1904), research into their behaviour has been growing in popularity due to their importance, as boundary layers can be found in almost every facet of life wherever fluid flows can be found.

In short, boundary layers are caused by interactions between a viscous fluid and a solid surface, where the flow at the surface remains stationary with respect to it, and the mean velocity gradually increases as one moves away from the surface, eventually reaching the freestream velocity. Boundary layers can range in thickness from sub-millimeter in micro-fluidics to kilometers in atmospheric flows, and they can have significant influence on a wide range of problems ranging from heat exchangers to atmospheric and oceanic currents (Smits and Marusic 2013). Turbulent boundary layers (TBL) in particular are of special interest to researchers because, like freestream turbulent flow, they are also ubiquitous in nature. Analogous to homogeneous isotropic turbulence, the simplest form of a TBL is the canonical zero-pressure-gradient TBL. It is usually produced experimentally by having the boundary layer develop over a large flat plate. The transition from laminar to tur-

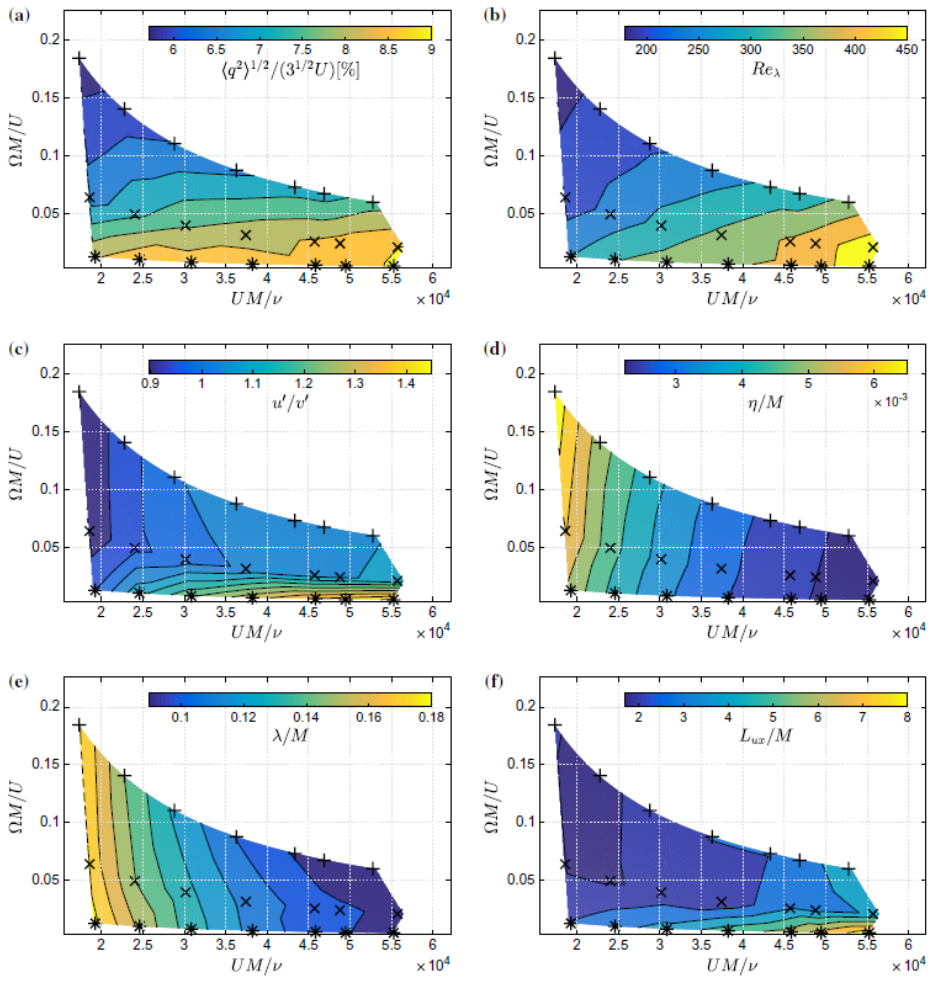

Figure 1.7: "Contours identifying the co-dependence of the produced turbulence on the Reynolds number and the Rossby number (plotted in inverse). Contours are drawn for solid square wings. *Asterisk* U1b to U7b, $\Omega \pm \omega = 0.625 \pm 0.375$ Hz; *multi symbol* U8b to U14b, $\Omega \pm \omega = 3 \pm 2$ Hz; *plus symbol* U15b to U21b, $\Omega \pm \omega = 8 \pm 7$ Hz." Taken with permission from Hearst and Lavoie (2015).

bulent can be either natural or artificially tripped.

Boundary layers in general can be characterized by their velocity profiles $u(x_2)$, which can be further decomposed into the mean $U(x_2)$ and the fluctuating $u'(x_2)$ components via Reynolds decomposition. From the mean velocity profile, three different boundary layer thicknesses of interest can then be defined: the boundary layer thickness δ, the displacement thickness δ^*, and the momentum thickness θ.

The boundary layer thickness δ is typically defined as the wall-normal position where $U(x_2)$ reaches 99% of the freestream velocity U_0, and it represents the physical boundary layer thickness. Other thresholds exist, such as 95% of U_0, in which case δ is typically denoted as δ_{95}. However, for the purpose of this project, we will assume the 99% threshold (i.e., $\delta = \delta_{99}$).

The displacement thickness δ^* is defined as

$$\delta^* = \int_0^\infty \left(1 - \frac{U(x_2)}{U_0}\right) \mathrm{d}x_2. \tag{1.7}$$

It represents a hypothetical boundary from the surface, where the flow within this bounded region has uniform velocity U_0 and has the same flow rate as the real complete boundary layer. In essence, the displacement thickness modifies the shape of the object such that an inviscid solution to the problem with the modified shape yields the same flow field.

In a similar manner, the momentum thickness θ is defined as

$$\theta = \int_0^\infty \left(\frac{U(x_2)}{U_0}\right)\left(1 - \frac{U(x_2)}{U_0}\right) \mathrm{d}x_2. \tag{1.8}$$

Analogous to δ^*, θ represents a hypothetical boundary where the bounded region has uniform velocity U_0 and has the same momentum flow rate as the real complete boundary layer. The displacement and momentum thicknesses can be combined to form the shape factor $H = \delta^*/\theta$. This can be used as an indicator of the fullness of a boundary layer mean velocity profile. Smaller values of H indicate a fuller profile, i.e. the velocity gradient near the wall is larger, and moving away from the wall, more of the boundary layer exhibits a flatter velocity profile close to U_0. The friction velocity $U_\tau = \sqrt{\tau_w/\rho}$ is a measure of the shear, or velocity gradient, at the wall, and is typically used as a normalization factor. Here τ_w is the shear stress at the wall. The normalized wall units for position and velocity are $x_2^+ = x_2 U_\tau/\nu$ and $U^+(x_2^+) = U(x_2)/U_\tau$.

In a TBL, the relationship between U^+ and x_2^+ forms what is commonly referred to as the law of the wall. Very close to the wall ($x_2^+ < 5$), $U^+ = x_2^+$ in what is

called the viscous sublayer. For $x_2^+ > 30$, we have the log-law region and the wake region, where

$$U^+ = \frac{1}{\kappa} \ln x_2^+ + C^+ + \frac{2\Pi}{\kappa} \mathcal{W}\left(\frac{x_2^+}{Re_\tau}\right), \tag{1.9}$$

where κ is the von Kármán constant, and C^+ is also a constant. The last term of equation 1.9 only becomes important as one approaches the end of the log-law region and enters the wake region, where the normalized velocity profile exhibits a bump, deviating away from the log-law. Here, Π is Coles' wake parameter (Coles 1956), and $\mathcal{W}$ is a wake function (Chauhan et al. 2009). The friction Reynolds number is defined as $Re_\tau = U_\tau \delta / \nu$. Other Reynolds numbers relevant to TBLs are $Re_x = U_0 x_1 / \nu$ and $Re_\theta = U_0 \theta / \nu$.

The combination of freestream turbulence (FST) and TBL is a natural development in the field of turbulence research considering that both of these phenomena are abundant in natural processes and technical applications. Hancock and Bradshaw (1983; 1989) were the first ones to investigate the influence of FST on TBLs. This was done through the use of two passive grids generating turbulent flow over a flat plate. A range of Re_θ between 2870 and 5760 was achieved by varying the streamwise position of the measurements. It was found that both the turbulence intensity and the integral length scale influence the structures of the boundary layer. However, the highest freestream turbulence intensity achieved was only 5.8%, and this was measured at $x_1/M = 15$, where the flow is typically still inhomogeneous (Ertunç et al. 2010, Isaza et al. 2014, Hearst and Lavoie 2014; 2015). Castro (1984) showed that skin friction increases with Reynolds number and freestream turbulence intensity. However, the measurements were also done close to the grid, with the largest freestream turbulence intensity measured at $x_1/M = 6$. This trend of increasing skin friction with respect to increasing FST was subsequently observed by Blair (1983a;b) and Esteban et al. (2017).

Thole and Bogard (1996) generated freestream turbulence with up to 20% intensity through the use of crossflow jets and found that the log-region of the velocity profile remains relatively unaffected. This shows that TBLs display a certain degree of robustness to how FST is generated.

Hutchins and Marusic (2007) introduced the use of spectrograms to identify the locations and the frequencies of velocity fluctuation peaks in the boundary layer. Two such peaks are found. One is near the wall and it is associated with the near-wall peak of the velocity variance. A second peak emerges in the outer layer when Re_τ increases, with a distinct peak existing for $Re_\tau >= 7300$. The presence of this second peak was subsequently observed by Sharp et al. (2009), Dogan et al. (2016), and Hearst et al. (2018). These three works are significant in that they incorporated

the use of active grids to create FST with high intensity (on the order of tens of percent) and relatively high homogeneity and isotropy. This is a substantial extension on the parameter range compared to the earlier works of Castro (1984) and Hancock and Bradshaw (1989). The results show that the secondary peak in the outer layer can be reproduced at a significantly lower Re_τ by increasing the FST level. This has the implication that high Re_τ boundary layers can be studied in small to moderately sized facilities with the use of an active grid (Dogan et al. 2017). Furthermore, the near wall peaks in the spectrogram are not noticeably affected by FST (Dogan et al. 2016). This was later confirmed by Hearst et al. (2018) in that only the large structures in the freestream turbulence penetrated the turbulent boundary layer and stimulated the growth of the outer velocity fluctuation peaks, while the inner peaks remained largely unaffected. Ganapathisubramani (2018) included this observation in his formulation of the law of the wall for turbulent boundary layers subjected to the influence of freestream turbulence. Hearst et al. (2018) were also able to reconstruct the spectra of the boundary layer from that of the freestream turbulence. These promising developments make the active grid approach for simulating high Re_τ boundary layers through stimulation via FST an attractive option.

So far, the studies mentioned have mostly focused on single-plane measurements of turbulent boundary layers. The spatial development of a canonical, naturally developing turbulent boundary layer without freestream turbulence has been investigated by Vincenti et al. (2013) and Marusic et al. (2015). The near-wall velocity fluctuation peak grows with downstream spatial development, while at sufficiently high Re_τ, the outer velocity fluctuation peak starts to emerge. These are consistent with the observed behaviours of single-plane measurements with increasing FST, further suggesting that increasing FST has similar effects as letting the TBL develop naturally. Numerical simulation studies on evolving canonical turbulent boundary layers have been performed by Ferrante and Elghobashi (2004), Wu and Moin (2009), Eitel-Amor et al. (2014), and Wu et al. (2017). In terms of investigating the spatial development of a turbulent boundary layer subjected to incoming FST, there has been very few works on the topic. Raushan et al. (2018) posed the inverse question on how would a spatially developing turbulent boundary layer influence grid-generated turbulence. However, their focus was primarily on the near-field flow behind passive grids. There has been several DNS studies into this topic (You and Zaki 2019, Wu et al. 2019, Kozul et al. 2020, You and Zaki 2020). Generally, the skin friction increases as FST increases (up to 15% in the work by You and Zaki (2019)), and the wake is suppressed in the presence of FST.

Currently, there exists a research gap on the spatial evolution of a TBL subjected to FST that is also spatially evolving. The aforementioned works either only examined the effect of FST at a single measurement plane, or they only examined the

spatial evolution of a TBL without FST. The limitations in the investigated parameter space were primarily due to the inflexibility of their experimental set-up. Furthermore, their Reynolds numbers and turbulence intensities are still relatively low. The few DNS studies that touch upon this gap are also limited to having relatively low Reynolds numbers ($Re_\theta \leq 3000$). Nonetheless, all of these works lay a firm foundation and provide good insights, and this project seeks to address this knowledge gap by experimentally investigating the spatial development of a turbulent boundary layer subjected to different incoming freestream turbulent flows that are also evolving.

1.2.3 The effects of freestream turbulence on airfoils

Ever since the pioneering works of Otto Lilienthal and the Wright brothers on airfoil designs for their respective gliders and aircraft, airfoils have slowly trickled into a wide range of applications in our daily lives. They can be found anywhere from the manoeuvring fins of a submarine up to the wings on the space shuttle, from the scorching environment inside a jet engine's turbine section, to the freezing conditions of wind turbine blades perched atop a summit. And indeed relevant to this project, wind turbine airfoils need to operate in a wide range of inflow conditions within the atmospheric boundary layer, caused by a combination of shear flow, terrain, obstacles, and weather systems. A survey conducted at the GROWIAN facility by Mücke et al. (2011) measured the average on-site freestream turbulence intensity to be between 5% to 10%, with occasional gusts exceeding 40%. While this is only a survey done at one specific location, it does give an idea about the wild variations in turbulence intensity that can be expected by a wind turbine blade.

Before going further, we will introduce some concepts related to airfoil aerodynamics. An airfoil is defined as the 2D cross section profile of a lifting body, typically a wing. The frontmost and the rearmost points on an airfoil are defined as the leading and the trailing edges, respectively. A chord line is a straight line that connects these two points, and the chord length, c, is the length of this line. The camber line is defined as the locus of midpoints between the upper and lower surfaces of an airfoil. As an airfoil moves through a fluid, forces are generated that act upon the airfoil. The force that acts perpendicular to the direction of the movement is defined as the lift, L, while the force acting parallel to the movement but in the opposite direction is defined as the drag, D. We acknowledge that L is used previously in this thesis to denote the integral length scale, however, we will also use L here for lift in accordance with the literature convention. The angle between the chord line and the freestream velocity, U_0, is defined as the angle of attack, α. The sectional lift, L', is defined as the lift per unit span, where span is the dimension of the wing in the direction perpendicular to the airfoil plane. We can also define

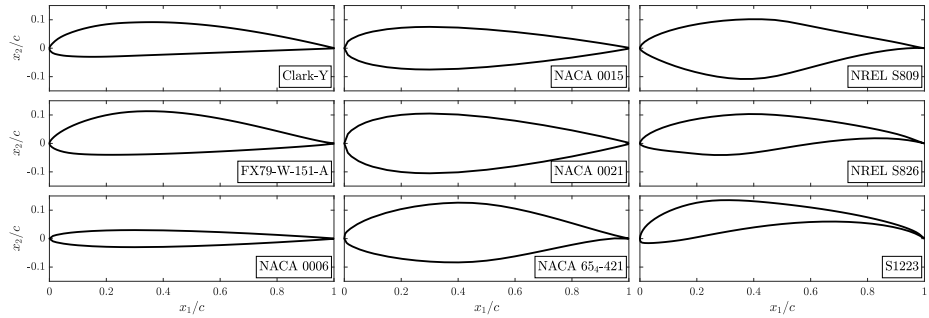

Figure 1.8: Selected airfoil profiles that are examined by the studies mentioned in this section. Note that DU93-W-210 is not included because its airfoil coordinates are unavailable, and NACA 0012 is not included because it closely resembles NACA 0015.

the sectional lift coefficient C_l as

$$C_l = \frac{L'}{\frac{1}{2}\rho_0 U_0^2 c}, \tag{1.10}$$

where ρ_0 is the freestream fluid density. Stall is defined as the phenomenon where the airfoil experiences significant flow separation, resulting in a loss in lift and a significant increase in drag. The stall angle is defined as the α in which maximum C_l is reached. Typical airfoils would also have a normal operating region before stall. Within this region, C_l scales linearly with α, so we will refer to this region as the linear region. The lift slope is defined as the rate of change of C_l with respect to α within the linear region. Lastly, the Reynolds number relevant to airfoils is the chord Reynolds number $Re_c = U_0 c/\nu$.

We will now examine selected past studies on the effects of FST on airfoil performance, with an emphasis on the stall characteristics and the lift slope. Figure 1.8 shows the airfoil profiles that will be mentioned in the following paragraphs. They include applications for general aviation (Clark-Y, NACA 00XX series), wind turbine blades (Wortmann FX79-W-151A, NACA 65_4-421, NREL S series), and low Reynolds number flight (Selig S1223). Note that the coordinates for another wind turbine airfoil, DU93-W-210, is unavailable, and therefore not included in this figure. NACA 0012 is also not included because it closely resembles NACA 0015, which is included in figure 1.8.

First we will focus on airfoils designed for general aviation purposes. Stack (1931) was one of the first to highlight the different behaviour of thin and thick airfoils when subjected to freestream turbulence. In their investigation, FST was generated by means of a coarse grid. It was found that an increase in FST increased the stall

angle and the maximum lift for NACA 0021 and Clark-Y airfoil profiles, while their lift slope in the linear region is relatively unchanged. Both airfoils are thick airfoils. However, a thinner airfoil, NACA 0006, did not have its lift properties significantly influenced by FST. The chord Reynolds numbers ranged from 5.2×10^4 to 3.4×10^6.

Early works by Owen and Klanfer (1953) and Gaster (1967) examined the transition process in the airfoil boundary layer, which is relevant for subsonic, low speed applications, where a significant portion of the airfoil boundary layer could remain laminar, and therefore susceptible to boundary layer separation leading to reductions in aerodynamic performance. This transition process can be influenced by Re_c. Other influential factors include the airfoil surface finish and FST, and there is a need for systematic investigations into the isolated effects of these factors (Mueller et al. 1983).

Hoffmann (1991) saw a marked increase in the maximum C_l and the stall angle for a NACA 0015 airfoil when it was subjected to increasing FST levels from 0.25% to 9%. The lift slope for this study, however, stayed relatively constant. The same trends were observed by Swalwell et al. (2001) for a NACA 0021 profile. For lower freestream turbulence intensity, Huang and Lee (1999) observed that even for FST levels less than 1%, there was an improvement in the aerodynamic performance of a NACA 0012 profile. Wang et al. (2014) extended the turbulence intensity to up to 6% for the same airfoil and also observed an increase in the maximum lift. Both studies did not see significant changes to the lift slope. It should be noted that the Re_c involved here are between 10^3 and 10^5, and neither study showed that the aerodynamic behaviour reached a Reynolds number independent state.

Moving to a more specialized application, both Butler et al. (2001) and Michálek et al. (2012) saw the transition point in the airfoil boundary layer of gas turbine blades move upstream with increasing turbulence. The effects are however diminished at higher Reynolds number on the order of 10^5. Ravi et al. (2012a) examined the influence of FST on a thin flat plate with elliptical leading edge, typically used for small low Reynolds number Unmanned Aerial Vehicle (UAV) applications, and found that the lift slope actually decreased with increasing FST.

Moving to wind turbine airfoils, Devinant et al. (2002), through the use of passive grids, found that for a NACA 65_4-421 airfoil, the maximum lift and the stall angle increases with FST, but the lift slope decreases. The highest turbulence intensity achieved was 15.4%, which is quite high for passive grid studies. However, this likely came with the cost of inhomogeneous freestream flow, with the measurements for that case taken at $x_1/M = 5$. For this study, Re_c ranged from 1×10^5 to 7×10^5. Kamada et al. (2011) reported similar behaviour as Devinant et al. (2002) for a DU93-W-210 wind turbine airfoil. A passive grid was also employed

to generate FST, where the model was placed at $x_1/M = 6.6$ for the most turbulent case. This is similar to the closest placement found in Devinant et al. (2002). In contrast, Maldonado et al. (2015) used an active grid to generate moderate FST of 6.14%, but at a streamwise location of $x_1/M = 39$, which is within the homogeneous flow region. Maldonado et al. (2015) found that for a NREL S809 airfoil, both the maximum lift and the lift slope increased with increasing FST, but the stall angle remained relatively constant. This is in contrast with the findings of Devinant et al. (2002) and Kamada et al. (2011), especially on the behaviour of the lift slope, despite all three studies examining wind turbine airfoils. Both Kamada et al. (2011) and Maldonado et al. (2015) had similar Re_c, at 3.5×10^5 and 2.08×10^5 respectively.

As mentioned in the previous sections, at locations very close to the grid, the flow exhibits strong inhomogeneity (Ertunç et al. 2010, Hearst and Lavoie 2014, Isaza et al. 2014). The flow inhomogeneity can potentially interact with flow features around an airfoil and cause unintended effects. It has been documented that 3D cell structures can develop on the airfoil surface near stall (Sarlak et al. 2018, Sarlak Chivaee and Sørensen 2018), and if any significant flow inhomogeneity exists, then they are likely to affect the behaviour of those stall structures. The different behaviour observed in Devinant et al. (2002), Kamada et al. (2011), and Maldonado et al. (2015), in particular for lift slopes, add some evidence to the potential adverse effect of flow inhomogeneity. This is further strengthened by the fact that all three studies had similar chord Reynolds numbers, therefore the effects of flow inhomogeneity is more isolated.

Looking at more investigations into wind turbine airfoils, Schneemann et al. (2010) saw no significant change in the lift slope for a Wortmann FX79-W-151A airfoil at $Re_c = 7 \times 10^5$, however the streamwise location of the measurements is unknown. In a cross-application study, Cao et al. (2011) examined a Selig S1223 airfoil at Re_c up to 10^5 for the purpose of potential use on a vertical axis wind turbine. This airfoil was originally developed for low Reynolds number UAV applications. Contrary to the aforementioned studies, it was found that increasing FST made no significant improvement on the lift properties of the airfoil, with the exception that it made the stall behaviour smoother. Li et al. (2016) investigated a self-developed wind turbine airfoil for Re_c up to 2×10^5, and found that the lift slope was not significantly affected by increasing FST. Like some of the previous studies, the model was placed close to the grid at $x_1/M = 7$ for the highest turbulence intensity case (13.9%). Sarlak et al. (2018) used three wires instead of a space filling grid to investigate the effect of FST on a NREL S826 airfoil at a relatively low Re_c of 4×10^4. As a result of the set up, the FST generated is not homogeneous, but nevertheless, turbulence intensities up to 2% gave significant improvement to the lift performance of the

airfoil.

Most of the aforementioned studies agree that increasing FST improves the lift performance, either through an increase in the maximum lift, an increase in the stall angle, or a combination of both. However, major disagreements arise when it comes to the lift slope behaviour. Some showed a decreasing trend (Devinant et al. 2002, Kamada et al. 2011, Ravi et al. 2012a), others reported an increasing trend (Maldonado et al. 2015), and lastly some reported no significant changes at all (Schneemann et al. 2010, Wang et al. 2014, Li et al. 2016). Several factors can contribute to this disagreement, which include the airfoil shape, Reynolds number, and freestream flow homogeneity. Because of this, a part of this project seeks to address these three factors in an effort to systematically investigate the influence of freestream turbulence on the aerodynamic behaviour of a wind turbine airfoil.

Furthermore, we also seek to combine the traditional time-averaged pressure distribution and lift calculations with spectral analysis of the airfoil surface pressure fluctuations. Blackburn and Melbourne (1996) investigated the frequency content of the lift coefficient for a cylinder, while Sicot et al. (2006b) performed the same for an airfoil. Watkins et al. (2010) and Ravi et al. (2012b) examined the frequency content of their pressure data. However, to date, there has been no effort in combining the spectral analysis of the pressure and lift data of an airfoil for the purpose of shedding more insight into their time-averaged pressure and lift behaviour. It is one of the objectives of this project to address this research gap, as well as provide a systematic investigation into the effect of freestream turbulence on the aerodynamic properties of a wind turbine airfoil, taking into account the three potential factors identified for lift slope behaviour discrepancies found in earlier studies, namely the airfoil shape, Reynolds number, and flow homogeneity.

1.2.4 Atmospheric Boundary Layers & Wind Turbines

As mentioned previously, one of the grand challenges identified by Veers et al. (2019) for future wind energy development is the "improved understanding of atmospheric and wind power plant flow physics". The last part of this project seeks to contribute to this challenge by studying ways to generate different turbulent shear flows in an experimental setting, and applying that to a model wind turbine to examine the wake structures (in particular the near-field) in an effort to understand the effects of turbulence and shear.

Atmospheric boundary layers (ABLs) present a difficult challenge for wind energy research. In essence, it is a group of highly variable turbulent shear flows that is influenced by many factors, including the local terrain, natural or man-made obstacles, local weather, etc. As modern wind turbines can have rotor diameters

on the order of 100 – 200 m, and considering that tower heights can also reach up to around 100 m, it follows that the total swept height of some of the largest wind turbines can be up to 200 m. As ABLs can have thicknesses ranging from hundreds of meters to kilometers (Bianchi et al. 2006), it is evident that modern large wind turbines cover a non-negligible portion of the ABLs, and thus, the flow over the rotor swept area cannot simply be modelled as uniform. Often, the shear flow profile for ABLs can be parameterized by

$$\frac{U(x_3)}{U_r} = \left(\frac{x_3}{x_{3,r}}\right)^{\alpha}, \tag{1.11}$$

where x_3 is the wall normal, or vertical, direction in keeping with wind energy research convention. We note that earlier, for boundary layers, we used x_2 to denote the wall normal direction. We use x_3 here to keep with the wind energy research convention. The subscript r denotes a reference position (usually the wind turbine hub height), and the exponent α modifies the shape of the profile (Wagner et al. 2011). For reference, $\alpha = 0$ denotes a uniform flow, and $\alpha \approx 0.143$ denotes a neutrally buoyant/stable ABL. Wagner et al. (2009; 2011) collected 2340 independent real-world ABL profile measurements and classified them into 173 different categories of shape. It was found that about 44% of their measured profiles cannot be accurately modelled by eq. 1.11. Even within the profiles where eq. 1.11 is valid, the exponent α can still vary from -0.20 to 0.36 (Dimitrov et al. 2015). Not only does the shear profile of ABLs vary widely, the turbulence intensity within the flow can have large variations as well. Recall, Mücke et al. (2011) surveyed the atmospheric flow between a height of 50 m to 150 m at the GROWIAN facility and found that the wind velocity has variations of 5% and 15% on average, with occasional gusts exceeding 40%. All this goes to show that real-world flows experienced by modern large wind turbines are highly complex, and it is insufficient to only investigate a limited number of turbulent shear flows in an experimental setting.

The extreme variations in the inflow experienced by wind turbines can have large effects on their power output as the power $P \propto U^3$. They can also negatively impact the maintenance frequency and the overall lifespan of a wind turbine. Typically grouped into wind farms, the collective power output of wind turbines can vary by as much as 50% in a time-span on the order of 2 minutes, with power changes up to 15 standard deviations away in extreme cases (Milan et al. 2013). Furthermore, within these wind farms, wind turbines are inevitably placed inside the wake region of other wind turbines. This can cause significant reduction in power from 20% to 46%, caused simply by wake flows, without the added complexity of highly varying ABL inflow (Adaramola and Krogstad 2011). With good planning of the wind farm layout, this power loss can be reduced to 10% to 20%, but it is still a non-negligible

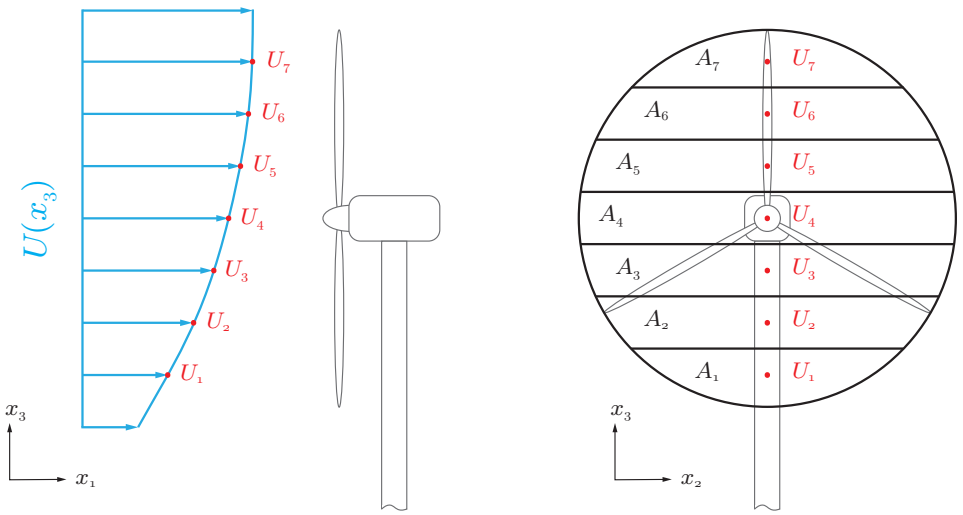

Figure 1.9: "Example schematic of a discretized incoming velocity field and swept area break-down for a wind turbine. The dots represent measurement positions". Reproduced and modified with permission from Hearst and Ganapathisubramani (2017).

loss (Barthelmie et al. 2010, Gaumond et al. 2012). As mentioned before, the inflow condition for modern large wind turbines should be considered as turbulent shear flow instead of uniform flow. This presents a challenge to finding a characteristic freestream velocity when designing a wind turbine. The logical choice of the hub height velocity U_{hub} is no longer adequate in light of shear flow. Wagner et al. (2009) introduced the concept of an equivalent velocity U_{eq} to replace U_{hub}, namely

$$U_{\text{eq}} = \left[\frac{1}{A} \sum_i U_i^3 A_i \right]^{1/3}, \tag{1.12}$$

where A is the rotor swept area, U is the mean incoming velocity, and the subscript i denotes the i^{th} segment of the discretized frontal area. Figure 1.9 shows a schematic of a discretized incoming velocity field. Note here that the U_i here represents the velocity of the i^{th} segment, and not the velocity in the i^{th} spatial direction.

Later, Choukulkar et al. (2016) expanded this formulation to include turbulence intensity and wind yaw angle, namely

$$U_{\text{eq}} = \left\{ \frac{1}{A} \sum_i U_i^3 \left[1 + 3 \left(\frac{u_i'}{U_i} \right)^2 \right] \left[1 - \frac{\Phi_i^2}{2} - \frac{\Phi_i'^2}{2} \right]^3 A_i \right\}^{1/3}, \tag{1.13}$$

where u_i' are the velocity fluctuations and Φ_i and Φ_i' denote the mean and the fluctuations of the incoming wind angle. It can be seen that any presence of velocity fluctuations would increase the magnitude of U_{eq}, while any non-zero inflow angle (with zero defined as being parallel to the hub centreline) will reduce the magnitude.

To generate turbulent shear flows in a laboratory setting, flow control or modification devices need to be used. The simplest devices are spires placed near the entrance of a test section. They augment the naturally developing boundary layers on the test section floor or walls by creating varying blockage in the plane perpendicular to the flow, and by having spires with different blockage profiles, different shear profiles can be created. Because the spires also create mixing wakes in the flow, they have the added benefit of also augmenting the turbulence intensity in the test section. Counihan (1969; 1973) generated both a neutrally buoyant ABL and a simulated urban profile with $\alpha = 0.28$ through these spires, and the turbulence intensity was around 7.5%. Other methods include adding a flow straightener to the shear generator to modify the turbulence intensity, and the shear profile to a lesser extent (Vanderwel and Tavoularis 2011). However, it is evident that these passive devices are very limited in the parameter space they can cover in terms of different shear profiles and turbulence intensities. For each combination of shear profile and turbulence intensity, a new device(s) needs to be manufactured. There is also coupling between the amount of blockage and the resulting turbulence intensity, making investigations into the isolated effects of shear and turbulence difficult, if not impossible, with these passive devices. Nevertheless, important insights into the effect of turbulent flow on wind turbines have been made. Medici and Alfredsson (2006) and Hattori et al. (2007) both found that an increased level of FST reduced the wake width due to the turbulent transport of high-momentum flow from the freestream into the wake. However, this width reduction was only observed for two or more rotor diameters downstream of the wind turbine. Rind and Castro (2012) found that in the far wake of an axisymmetric disc, FST actually leads to an increase in the body drag, resulting in larger wake momentum deficits. Another research gap that exists within the historical investigation into simulated ABLs is that most studies have focused on reproducing the neutrally buoyant profile with $\alpha = 0.143$ because this is a reasonably well-understood theoretical state. However, Wagner et al. (2009) did not include this profile within the top ten most commonly occurring natural ABLs, so continued investigation into this particular shear profile may not provide much practical purpose to wind turbine and wind farm designs. Overall, the passive flow modification devices have contributed greatly to the field of turbulence shear flow research, but they are limited in the expanse of the parameter space they can cover for future studies.

As with grid turbulence research, the advent of active grids since the seminal work

of Makita (1991) has opened the door to vast possibilities for turbulent shear flow research. Already mentioned briefly in Section 1.2.1, here, we will provide more details on past studies specifically on this research topic.

Shen and Warhaft (2000) were the first to incorporate an active grid in a shear flow study by inserting variable solidity screens downstream of the active grid. Cekli and van de Water (2010) were the first to attempt to create a shear flow with an active grid alone. This was accomplished by setting the initial position of the wings to different angles, and then having each set of wings flap about this angle. Schottler et al. (2017) set their active grid wings to two sets of static positions to create a classical and an inverted shear profile. Talavera and Shu (2017) created three different simulations of turbulent shear flows using a single active grid setup, with turbulence intensities ranging from 3% to 17.4%. However they did not explore the possibility of creating different shear velocity profiles in their study. Hearst and Ganapathisubramani (2017) were the first to decouple shear and turbulence intensity with an active grid. This was done by flapping one plane of bars about their centre position (defined as when the wings are parallel to the mean flow). Each bar was assigned a different flapping angle and by changing the angles, different time-averaged blockages were created, thus leading to different shear flow profiles. The other plane of bars was operated in the classic double-random spinning mode used to create flows with different turbulence intensities. The flapping algorithm was deliberately made asynchronous, meaning the wings are flapped sequentially in random order. This was done to prevent sharp peaks in the spectra associated with the flapping frequency, demonstrating the latest advancement of an active grid in creating tailored turbulent flows. Figure 1.10 shows the expanded parameter space for turbulent shear flows achieved by this set up.

The last part of this project seeks to build upon the work of Hearst and Ganapathisubramani (2017) by putting a lab-scaled model wind turbine in the generated turbulent shear flow and examine the resulting near-field wake structures. In the extensive review of available experimental and numerical investigations of wake flow of wind turbines by Vermeer et al. (2003), the authors stressed the need for a systematic investigation into the wake structures behind both single wind turbines and wind farms, with the near-field wake region highlighted as a particularly important and interesting area of research. It is the goal, therefore, of this project to address to a certain degree this knowledge gap.

1.3 Objectives

The main objective of this project is to experimentally investigate the effects of turbulent flow on the various problems inspired by wind energy. The project is divided into the following three research topics:

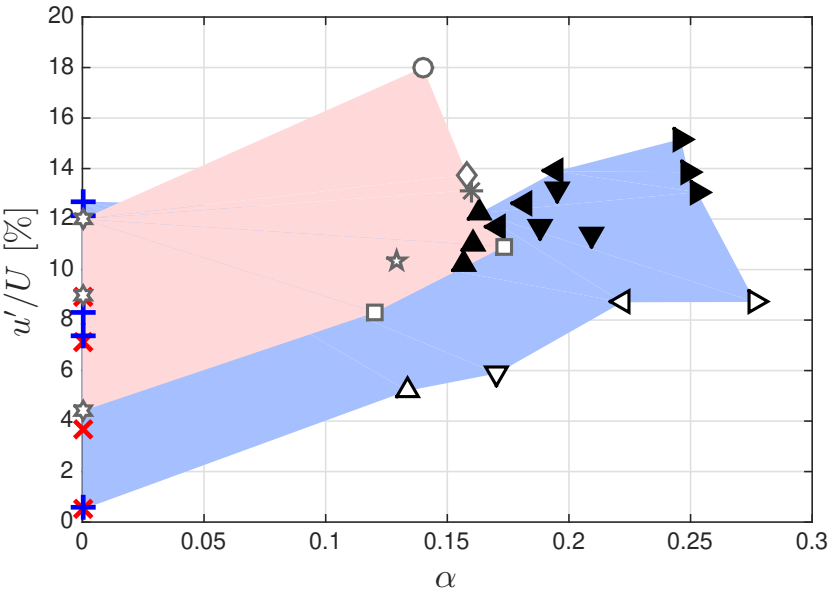

Figure 1.10: "Parameter space of wind tunnel turbulent shear flows. Measurements from Hearst and Ganapathisubramani (2017) are represented by the black triangles: (▷) shear mode 1, (▽) shear mode 2, (△) shear mode 3, and (◁) shear mode 4; the empty triangles represent the turbulence mode A measurements. Homogeneous turbulence ($\alpha = 0$) cases from the same grid are also included from (×) Hearst et al. (2016) and (+) Dogan et al. (2016). measurements from other wind turbine model studies in wind tunnels are presented as gray symbols: (□) Chamorro and Porté-Agel (2009), (◇) Cal et al. (2010), (☆) Bossuyt et al. (2017), (○) Sicot et al. (2006a), and (∗) Aubrun et al. (2013). The red shaded area represents the parameter space of wind tunnel experiments relying on the wall to produce the shear. The blue shaded region represents the parameter space occupied by the presented methodology." Taken with permission from Hearst and Ganapathisubramani (2017).

1. The influence of freestream turbulence on the spatial development of a turbulent boundary layer.

2. The influence of freestream turbulence on the aerodynamic performance of a wind turbine airfoil.

3. The influence of turbulent shear flow on the near field of a lab-scaled model wind turbine.

Each of these research topics relates to a certain aspect of wind turbine operation, and together they form a step-by-step approach to the overall goal of looking at wind turbines in the atmospheric boundary layer. The project starts with the examination of the spatial development of a turbulent boundary layer under the influence of freestream turbulence. While we recognize that this is not exactly representative of an atmospheric boundary layer since we are limited in the Reynolds number and the integral length scales that can be created in our experimental facility, this is still the first work of its kind to our best knowledge, and it yields new insights into how a turbulent boundary layer develops under freestream turbulent flows of different intensity. The results will be briefly summarized in Section 3 and will also be available in the attached article.

Next, we move on to how freestream turbulence influences the aerodynamic behaviour of a wind turbine airfoil. The force coefficients are calculated via surface pressure measurements, and particular emphasis is paid to the combination of time-averaged trends and the frequency content of the pressure and lift force fluctuations. The turbulence intensities investigated correspond well to the expected field values, although we could not match the integral length scale-to-chord length ratio. The novelty of the work lies in the large amount of flow cases investigated, as well as in looking at the influence of freestream turbulence on both the time-averaged values and the frequency content of the pressure and lift force. To the best of our knowledge, this is the most extensive work of its kind to date, and it contributes to the field of wind turbine airfoil design.

Lastly, we look at a lab-scaled model wind turbine as a whole inside different turbulent shear flows. All the different flow cases are generated by one experimental set up, which is unprecedented in the field of turbulent shear flow research. Furthermore, we were able to separate the effects of the shear profile from the turbulence intensity by generating flows with similar shear profiles but different turbulence intensities, and vice versa. This is another first in this particular field of research. The flexibility of the set up allowed us to gain insights into how the near-field of a model wind turbine behaves under different turbulent shear flows, and also allowed

us to quantify the relative importance of turbulence intensity and shear profiles to those behaviour.

The experimental work for the three research topics is carried out at the Norwegian University of Science and Technology (NTNU) and the University of Southampton. The water channel system used for the spatially developing boundary layer study is a brand new facility. Therefore, a supplementary objective of this project is the successful completion and commissioning of the new water channel and all of its associated sub-systems.

Overall, the three topics investigated for this project constitute a relatively complete picture of how a wind turbine would behave under a variety of operating conditions. From the fundamental background flow to the complexity of a whole model wind turbine, we hope this thesis is received as a valuable contribution to experimental investigations applied to the field of wind energy, and by extension, lays the ground work for more general future studies into the effect of freestream turbulence on other objects.

Chapter 2

Experimental Methods

This chapter documents the various experimental facilities and methods used for each of the three investigative topics in this project. Because each of the experiments used a different facility and different experimental methods, this chapter will be organized by topics in the following order, with each section describing the facility and the experimental methods used:

1. Spatial development of TBLs under the influence of FSTs.
2. Lift and pressure characteristics of a wind turbine airfoil in FSTs.
3. Near-field of a model wind turbine in turbulent shear flow.

2.1 TBL in FST

2.1.1 Water Channel Facility

The investigation into the spatial development of turbulent boundary layers subjected to freestream turbulence is conducted in the new recirculating water channel facility at the Norwegian University of Science and Technology (NTNU) Gløshaugen Campus. Figure 2.1 shows the schematic of the water channel.

As a significant part of the project is the construction and commissioning of this new facility, a detailed description of the new water channel is given here. The process involved planning the layout and location of the water channel within the laboratory space, coordinating with both internal and external contractors and technicians for the installation of all the major components, designing and constructing the various sub-components, such as the active grid (described in the next section), and the characterization of the flow in the test section.

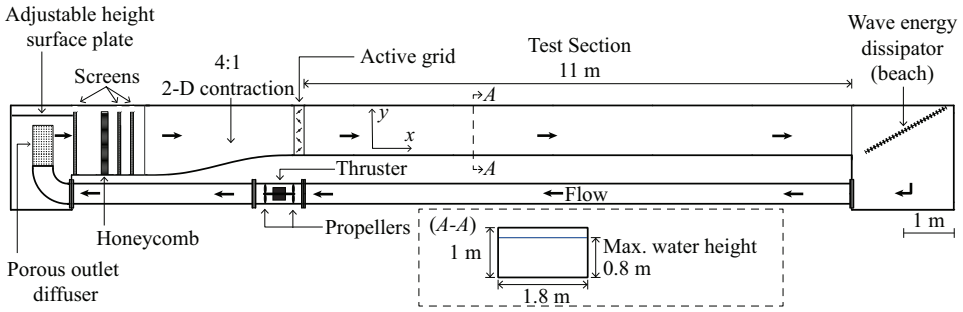

Figure 2.1: Schematics of the water channel facility at NTNU Gløshaugen Campus

The design of the water channel started in 2017 and primary construction was finished in 2019, with the channel entering its operational state in the latter half of that year. The water channel recirculates a maximum capacity of 65 tons of water through a series of return pipes and flow conditioners. The flow is driven by two Siemens 1AV2186B 3-phase squirrel-cage thrusters. The thrusters are off-the-shelf manoeuvring side-thrusters for small ships and yachts. Each thruster is connected to a composite 4-bladed counter-rotating Kaplan propeller set, with a diameter of 386 mm. Each complete thruster assembly outputs 28 kW of power, for a total of 56 kW power output. Two ABB ACS550 variable frequency drives (VFDs) are used to individually control the thrusters, with a maximum drive frequency of 50 Hz. Both the thrusters and the VFDs are supplied with 400 V power input.

Each thruster assembly is embedded within a return pipe made of 4 mm thick stainless steel, with an internal diameter of 400 mm. The return pipes run along the bottom of the water channel and are secured to the floor of the laboratory via pipe rings. The water enters the main facility from the return pipes into a polyethylene settling chamber, where two 90°-stainless steel elbows redirect the flow upwards. The elbows are followed by porous outlets to provide a diffused source of water. The diffusers are welded onto the vertical ends of the elbows and are also made of stainless steel. A circular steel plate is secured inside each diffuser to act as a plunger, for the purpose of preventing a jet of water coming out of the top of the diffuser under high-speed operations. A system of large acrylic plates supported by stainless steel frames is installed in the settling chamber around the diffusers. The height of the plates is adjustable so that they can be placed at the water surface for the purpose of attenuating the chaotic surface waves in the settling chamber, and to minimize the associated air entrainment.

The water then flows through an initial coarse stainless steel screen. The main purpose of the screen is to catch large debris in the flow to protect the honeycomb

structure downstream, but it also provides some preliminary flow conditioning and pressure equalization to the flow. The honeycomb is a one-piece expanded stainless steel construction welded unto a supporting frame. It sits on top of plastic support blocks inserted into a built-in slot inside the settling chamber, and the internal face of the frame is flush with the inner wall of the chamber. The honeycomb provides most of the flow conditioning by straightening the streamlines. Two additional stainless screens of progressively finer mesh are placed downstream of the honeycomb to provide the final flow conditioning before the contraction.

The contraction is constructed out of fibreglass and provides a 3D, 4:1 contraction ratio. Both the settling chamber and the contraction are supported by stainless steel frames. Between the contraction and the test section is a gap measuring 200 mm in length. This gap is intended to house the permanent frame for inserting an active grid or other passive turbulence grids, the details of which will be covered in the next section. The test section is a straight rectangular open channel measuring 1 m $\times$ 1.8 m $\times$ 11 m. It is constructed out of 19 mm thick float glass supported by stainless steel frames. The frame itself is painted with a matt black anti-rust coating. The clear, untempered glass wall and floor provide optical access for laser diagnostics and other visual measurement techniques.

The flow exits the test section into a rectangular stainless steel and glass end tank, which is connected to the other end of the return pipes, forming a complete circuit. Stainless steel meshes are placed at the entrance to the return pipes in the end tank to prevent large debris from entering the pipes and damaging the propellers. The end tank walls are reinforced with stainless steel frames, and a large polycarbonate plate measuring 20 mm in thickness is installed at the back wall to stop water flow should the glass panels on the back wall suffer structural failure.

The maximum designed water height is 0.8 m measured from the inside floor of the test section. There are overfill drains placed in the settling chamber and the end tank to prevent spillage from overfilling. Normal drainage is accomplished through two valves, one at the settling chamber and one at the end tank. Drainage is done through gravity alone, and there are no active drainage pumps, although small bilge pumps are needed in both the settling chamber and the end tank to remove any left over water that remains below the drain pipe inlet.

The water channel is filled with normal tap water from Trondheim municipality without prior filtering or treatment. The water is kept clean from debris and algae growth through a triple-filter system. This system consists of an electrical pump, a cyclone filter for larger debris, a particle filter for microscopic debris, and a UV filter for limiting algae and other organic matter growths. Each filter (except the UV filter) can be bypassed in case it is not needed or not operational. The filter

system is kept running at all times when the water channel is filled but not in use. This is to keep the water flowing to minimize algae growth. Currently, there is no active temperature control in the water channel, the water eventually reaches thermal equilibrium with the room, where it stays at a constant temperature with less than 0.5 °C daily variation in the test conditions ran for this study.

A Höntzsch ZS25 vane wheel flow meter is used to measure the freestream velocity in the test section. The sensor area has a diameter of 25 mm, and the measured velocity is averaged over this area. The measurement resolution is 0.01 m/s, and the velocity can either be directly read from the sensor display, or be measured through an analogue output to a DAQ system. We use a NI-9125 C series voltage input module. A T-type thermocouple is used to measure the water temperature, and it is connected to a NI-9120 C series temperature input module. A NI cDAQ-9178 CompactDAQ chassis is used to integrate both modules into a single unit that is then connected to a PC, where the data are acquired through MATLAB.

2.1.2 Water Channel Active Grid

Passive and active grids can be installed in the water channel. Figure 2.2 shows a 3D drawing of the active grid designed for the water channel. It contains all the structural, mechanical, and electrical components. As the active grid is also a new apparatus designed and commissioned to be an integral part of this project, a detailed description is given here as well.

The main structural frame consists of three large CNC-machined acrylic pieces that fill in the 200 mm gap. The frame pieces are secured to both the contraction and the test section via bolts and flanges, and water-tightness is accomplished through the use of O-ring strips on the faces of the flanges and silicone sealant on the inner surfaces. The bolt holes and slots for accessing the nuts are machined into the individual pieces as can be seen along the vertical and horizontal frames shown on the right side in figure 2.2. Each of the frame components is machined in-house in one piece. Acrylic glue was used to join the three pieces together during installation to improve the water-tightness at the corners where the pieces come together.

The inner faces of the frame measure 1820 mm $\times$ 1010 mm in cross sectional area, which makes it 10 mm larger on all three sides than the test section. This is done to accommodate removable skins designed for clean, passive grid, and active grid configurations. For the clean configuration, the skins are simple one-piece acrylic or marine-grade aluminum plates that sit flush with the inside of the test section after installation. For the passive grid configuration, the skins for each face are divided into two pieces, one on each side of a 100 mm deep slot milled into the inner face of the frames. This slot is made for insertion of a passive grid. For the

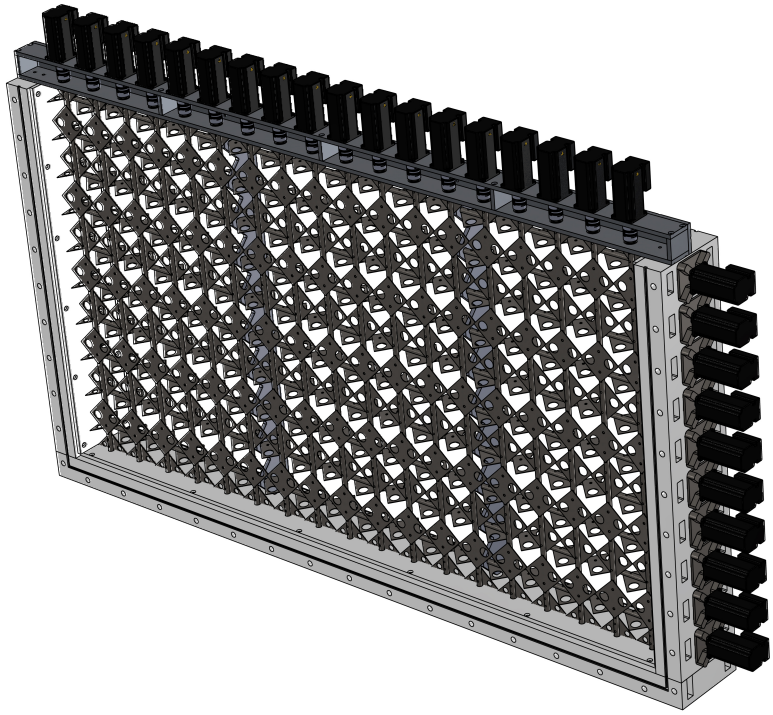

Figure 2.2: The active grid for the water channel facility at NTNU Gløshaugen Campus

active grid configuration, the skins are again one-piece, but this time with alignment holes machined into them for the horizontal and vertical bars. All skins are secured to the frame via countersunk bolts. Stainless steel threaded inserts are installed into the acrylic frame to prevent thread stripping from repeated usage.

We will now focus on the design and construction of the active grid. The grid contains 10 horizontal bars and 18 vertical bars for a total of 28 degrees of freedom. It is of the classic Makita-styled biplanar square mesh design (Makita 1991). The bars are round stainless steel sections that span the whole width and height of the permanent acrylic frame described earlier, making it a space-filling grid. The diameter of the bars is 12 mm, and they are spaced out evenly in a square pattern, with the mesh length $M = 100$ mm.

The wings are water-cut from 1 mm thick stainless steel sheets. Each wing is a square with sides measuring 70.7 mm, giving a diagonal length of 100 mm, which is M. Two 24 mm diameter holes are cut from each wing for the purpose of reducing the total load on each motor, and to ensure that the grid will never be in a 100%-blockage state. Triangular half wings are installed along the edges of the active grid to fill up the space without interfering with the skins. Each wing is secured to the bars via two bolts, and the wings are arranged in an alternating pattern on either side of the bar. To facilitate installation, the mounting holes on the bars are threaded, and slots of 100 mm in length and 1 mm deep are milled into the bars so that the wings have a flat surface to attach to and will sit flush with the bars when in the fully open position.

The total blockage ratio of this active grid ranges from 22.6% to 81.9%. To prevent the horizontal bars from sagging when mounted, four supporting points are built into the grid. Two are at the ends of the bars, and two are at the 1/3 and 2/3 width of the grid. The two sets of supports in the middle are mounted to two vertical acrylic struts with saw-tooth cutouts to accommodate for the spinning wings. Each support point consists of an inlaid plastic low friction bushing with the same internal diameter as the outer diameter of the bars.

A stainless steel flexible coupling and a custom-made adapter connect each bar to its driving motor. The flexible couplings can connect two circular bars with 12 mm diameter, while the custom adapters are made from the machined cutoffs of the bars, with one end made into a sleeve that slides into the drive shaft of the motor and is secured in place by a set screw. For the vertical bars, the motors are secured to an open aluminum box girder that attaches to the top of the two acrylic permanent side frames. A set of enclosed stainless steel bearings are inlaid to the bottom of the girder to align the motor-coupling-bar assembly.

The horizontal bars have the added complexity of making the interface watertight. To accomplish this, a set of custom designed watertight boxes is installed to the outer side wall of one of the vertical acrylic frames. Within these watertight boxes, custom-designed double lip seals from Trelleborg AB are placed in between stainless steel bearings and plastic bushings. The bearings and the bushings are of the same type used for the vertical bars and the horizontal bar supports respectively. The custom-made adapters go through these sets of support and seal, and the motors for the horizontal bars are mounted on the outside of the watertight boxes. Large drainage channels are designed into the boxes so that in the event of a leakage, the water would drain away from the electric motors.

The entire vertical bar assembly, which includes the bars, the wings, and the aluminum open box girder with motors attached, is designed to be removable as one unit. The horizontal bars need to be detached from the flexible couplings one by one during removal. The motors for the horizontal bars along with the watertight boxes are permanently mounted to the side frame.

To actuate the bars, 28 STM23S-3RE stepper motors from Moons Ltd. (or Applied Motion Products in other countries) are used. These motors are powered by two TDK-Lambda 48 V 52 A DC power supplies, which can supply the required maximum 2.5 A for each motor at 48 V. The motors are controlled through a PCI serial card installed on a PC. The signal cables are daisy-chained to each motor, and a unique ASCII name is also assigned to each. The control protocols are based on the Si^{TM} Command Language (SCL) developed by the manufacturer. Each motor comes equipped with its own encoder and motion controller, therefore no additional third party controllers are required. The commands are in the format of character strings. Through these commands, operational parameters such as rotational speed, acceleration, and directions can be set for each motor, allowing for complete independent control of all 28 bars.

2.1.3 Laser Doppler Velocimetry

Laser Doppler Velocimetry (LDV) is a non-intrusive laser-based diagnostics tool that can measure instantaneous velocities at a single point. The basic operating principle relies on the Doppler shift of scattered light coming off of tracer particles in the flow. Figure 2.3 shows a schematic representation of the basic working principle.

In this schematic, two laser beams, represented by the vectors e_1 and e_2, intersect at a point in space. When a particle (represented by the grey dot) passes through this intersection point with velocity u, it scatters light in all directions. In this case, we will consider the scattered light in the direction denoted by the vector e_s. Due

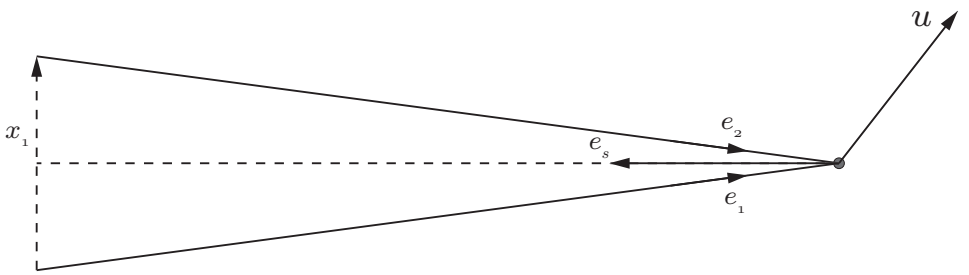

Figure 2.3: Schematic of the principle of LDV.

to the velocity difference between the particle and the two incident laser beams, the scattered light would have a Doppler shift in its frequency compared to the incident light frequency. Taking e_1 first and using Doppler-theory, the frequency shift between e_1 and e_s can be expressed as

$$f_{s,1} = f_1 \left[1 + \frac{u}{c} \cdot \left(e_s - e_1\right)\right], \tag{2.1}$$

where f_1 is the frequency of beam e_1 and c is the speed of light. Similarly, the same can be done for e_2 and e_s:

$$f_{s,2} = f_2 \left[1 + \frac{u}{c} \cdot \left(e_s - e_2\right)\right]. \tag{2.2}$$

The scattered light e_s would be composed of a superposition of the scattered light from e_1 and e_2, and because the moving particle induces two different Doppler frequency shifts due to the difference in the angles of e_1 and e_2 with respect to u, the resulting superposition would exhibit constructive and destructive interference patterns in the form of fringe lines. The frequency of these fringe lines is the difference between $f_{s,1}$ and $f_{s,2}$, and can be expressed as

$$\begin{aligned} f_D &= f_{s,2} - f_{s,1} \\ &= \frac{2\sin(\theta/2)}{\lambda_l} u_1, \end{aligned} \tag{2.3}$$

where θ is the angle between e_1 and e_2, λ_l is the wavelength of the laser beams, and u_1 is the velocity of the particle in the x_1 direction. Here we have also made the assumption that the two incident laser beams are from the same source and thus $f_1 = f_2$. Through simple re-arrangement of the terms, u_1 can be expressed as

$$u_1 = \frac{\lambda_l}{2\sin(\theta/2)} f_D. \tag{2.4}$$

This is the basic working principle of LDV, where all the quantities on the right hand side of eq. 2.4 are known *a priori* or can be measured, and thus the velocity component u_1 can be calculated directly. However, the direction of u_1 could be ambiguous as a particle travelling in the opposite direction will also induce a fringe frequency f_D. To resolve this, typically a Bragg cell is used to induce a frequency shift to one of the incident beams, so that eq. 2.4 now becomes

$$u_1 = \frac{\lambda_l}{2\sin(\theta/2)}(f_D - f_0), \tag{2.5}$$

where f_0 is the frequency shift induced by the Bragg cell.

The main advantage of LDV compared to other point measurement methods (such as hot-wires or Pitot-static tubes) is that it requires no calibration and that there is no sensor drift to account for. Multiple pairs of incident laser beams with different λ_l could be combined to measure multiple velocity components directly. To detect the scattered light, one can use the forward scatter method, where the light receiver is placed opposite of the light emitter, or the back scatter method, where the receiver and the emitter are placed on the same side. Forward scattering offers higher signal intensity, but its main drawback is the added complexity of aligning the receiver with the emitter. With advances in light detector technology, back scattering is becoming increasingly popular for LDV due to the ability to integrate the laser emitter and receiver into one unit, thus eliminating the need for sensor alignment.

However, LDV is not without its disadvantages. One of the main drawbacks is the intrinsic lack of a constant sampling rate. A detection can only be made when a particle crosses the intersection point, or the measurement volume. Thus, the instantaneous sampling rate is highly dependent on the particle density and the local flow velocity. This poses a problem for spectral analysis of the time series signal because it would require equi-distant time sampling. To resolve this, several methods have been developed to resample LDV time series (Boyer and Searby 1986, Adrian and Yao 1986, Ouahabi et al. 1998, Benedict et al. 2000). In the present work, a sample-and-hold technique is used where the resampled values take on the value of the previous real sample, until the next real sample arrives. This is employed in the works by Boyer and Searby (1986) and Adrian and Yao (1986).

This section is only intended as a high level overview of the working principle of LDV. For details on the physical set up for this experiment, please refer to *Article I*.

2.2 Wind Turbine Airfoil in FST

2.2.1 Wind Tunnel Facility

The testing facility used for this set of experiments is the large closed-loop wind tunnel at the Norwegian University of Science and Technology Strømningsteknisk laboratory. The wind tunnel itself is powered by a 220 kW fan located downstream of the test section. It is controlled through a variable frequency drive (VFD). The test section has a rectangular cross-sectional profile, with the area measuring 1.80 m $\times$ 2.71 m at the test section inlet. It has a length of 11.15 m, and the roof panels have adjustable height so that it can compensate for the growing boundary layers on the surfaces, creating a near zero-pressure gradient core flow in the test section. The maximum freestream velocity in the test section is around 23 m/s, although the test velocity is kept well below this to avoid mechanical vibration issues with the experimental rig. The test section is instrumented with a Pitot-static tube connected to a pressure transducer for freestream velocity measurements, as well as a K-type thermocouple situated on the inner surface of a side wall of the test section, near the middle in terms of the streamwise position, to measure the freestream temperature. A mercury barometer is used to measure the ambient atmospheric pressure.

Freestream turbulence is generated through the use of four different passive grids in seven different combinations. The grids are either constructed from steel or wooden beams. The finest grid is a metal mesh stretched over a steel frame, while the next finest grid is a monoplanar metal grid cut from one sheet. The two wooden grids are of bi-planar designs and are secured together through metal screws. For details on the physical properties of each of the grid as well as their combinations and the resultant inflow properties, please refer to *Article II*.

2.2.2 Hot-Wire Anemometry

The freestream turbulence statistics for each of the seven test cases are measured using constant-temperature anemometry (CTA), or more specifically, hot-wire anemometry. The working principle of CTA involves passing an electric current through a very thin metal wire, in this case tungsten, and heating it up to a temperature above the ambient temperature of the working fluid. As flow passes over the wire, heat is convected away. Typically, a Wheatstone bridge is used, in conjunction with other electrical components, to maintain the wire at a constant temperature (and therefore constant electrical resistance). The sensing wire forms one of the legs of the Wheatstone bridge. By measuring the voltage across the Wheatstone bridge needed to maintain the constant temperature, one can obtain a relationship between the voltage and the speed of the flow.

For this experiment, a StreamLine Pro CTA system is employed to perform the

hot-wire measurements. The accompanying proprietary software StreamWare Pro is used to set up the system, and the actual calibration and measurements are conducted via MATLAB scripts. The probe used is a Dantec 55P11 single-wire probe with a tungsten sensing element measuring 1.25 mm in length and 5 μm in diameter. The probe is mounted to a 55H21 straight probe support measuring 235 mm in length. The end of the support has an output BNC cable measuring approximately 0.8 m. A 4 m long BNC cable connects the probe support to the StreamLine Pro anemometer. The total length of the electric cables measured from the sensing element to the anemometer is therefore 5 m. A shorting probe is used to measure the resistance of the cables and the support, and this was recorded during the initial set up. The same value is used for all measurements. The total resistance of the probe system is measured daily, and the ambient temperature at the time of measurement is recorded to be used as the reference temperature for temperature correction, which will be explained in more detail later. The overheat ratio of the wire is set to 1.8. A square wave test is performed on the probe after the initial set up to check the frequency response of the system, which is estimated to be about 30 kHz. A 30 kHz low-pass filter is set for the whole system, with the sampling frequency set at 75 kHz, which is 1.25 times the required Nyquist frequency for the low-pass filter setting. The Kolmogorov frequency of the resulting turbulent flow is estimated to be around 10 kHz for the most turbulent case, therefore the frequency response of the whole system is sufficient to fully resolve the frequency content of the flow. Data acquisition is done through a $\pm$10 V NI-9125 C series BNC differential voltage module mounted in a NI cDAQ-9178 CompactDAQ chassis. The gain and offset for the output voltage signal from the hot-wire are 8 and 1.1 V respectively. This combination is found iteratively so that the amplified voltage signal spans the $\pm$10 V range of the DAQ module as much as possible.

Hot-wire calibration is performed *in-situ* with a Pitot-static tube providing the reference velocity measurements. A total of 12 calibration points are used, spanning approximately 1 m/s up to 1.5 times the test freestream velocity. The lower threshold for the calibration velocity is determined by the slowest stable operating speed of the wind tunnel. A Dantec Resistance Temperature Detector (RTD) is used to record the ambient air temperature simultaneously as the hot-wire signal. For each day of the experiment, calibrations were performed at the start and the end of the day to account for temperature and sensor drift. The temperature correction method of Hultmark and Smits (2010) is used in the post processing of the hot-wire raw voltage data. Figure 2.4 shows an example calibration curve from the experiment. We can see that in this method, U_1/ν is calibrated against the quantity $E^2/(k\Delta T)$, where U_1 is the freestream velocity measured by the Pitot-static tube, ν is the kinematic viscosity of the air, E is the analogue voltage output from the hot-wire probe without gain and offset, k is the thermal conductivity of air,

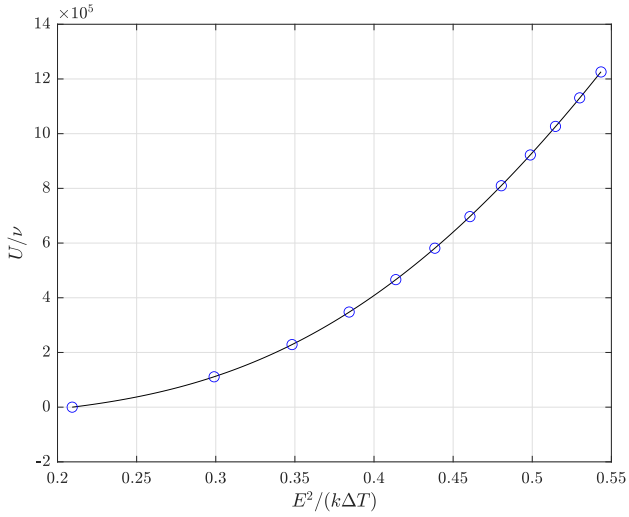

Figure 2.4: An example calibration curve using the temperature correction method of Hultmark and Smits (2010).

and ΔT is the temperature difference between the wire and the ambient air. Here $k = 418.4(5.75\times10^{-5}(1+0.00317T-0.0000021T^2))$ according to Kannuluik and Carman (1951). The overall uncertainty in the hot-wire measurements is estimated to be approximately 1% from the methods described by Benedict and Gould (1996).

2.2.3 Pressure Transducer Array

The airfoil pressure distributions are measured with a MPS4264 miniature pressure scanner from Scanivalve Corp. It has a range of 4" H_2O, or about 995 Pa, with an accuracy of $\pm$0.20% of the full range, or about 2 Pa. This pressure scanner uses 64 individual piezoelectric pressure sensors mounted on two separate printed circuit boards (PCBs) of 32 sensors each. Each board further groups the sensors into eight "sticks" of four sensors each for ease of replacement. The two PCB boards are mounted in the centre of a machined cavity, where the core of the housing is used as a reference pressure reservoir for all 64 sensors. Other circuit boards within the casing include the power and signal board, the processor board, the A/D converter board, and a valve position sensor board, which senses the position of the pneumatic valves within the pressure scanner for different operating modes. Overall, all the electro-mechanical components are included in a casing measuring approximately 90 mm $\times$ 30 mm $\times$ 36 mm, forming one complete unit with ports for power, input/output signals, 64 pressure ports, a reference pressure port, and a calibration

pressure port. The scanner itself is heated internally to minimize the thermal drift due to temperature changes. Power is provided by a five-port MPSPDM4500 DC supply at 24 V, which itself is powered by a standard 220 VAC wall socket. A dedicated power cable runs between the power supply and the pressure scanner. The signal is provided by a standard Ethernet cable connected to the scanner via an adapter cable. The other end of the Ethernet cable plugs directly into the PC. The entire pressure scanner, along with the power and signal adapter cables, are mounted inside the airfoil model. A slot as well as a channel for the electric cables are milled out of the model. The pressure ports are connected to the airfoil pressure tabs via flexible plastic tubing, and the reference pressure to the scanner is taken as the static pressure of the wind tunnel, obtained via a splice from the freestream Pitot-static tube. The two electric cables and the reference pressure tube pass through the channel in the airfoil model and come out from the bottom of the wind tunnel test section floor.

Data acquisition of the pressure scanner is accomplished through a web interface environment. Within this environment, one can set the data acquisition rate, acquisition time (or number of samples), data unit, and etc. For our purposes, the sampling rate is set at 800 Hz for 60 s for simultaneous sampling of all 64 sensors. The scanner can go up to 2500 Hz for sampling rate, however that would limit the number of simultaneously sampled ports to 16. Furthermore, the frequency response of the entire system is estimated to be 140 Hz from the spectra of the pressure fluctuation time series. Therefore, the sampling rate used here is more than sufficient to resolve the full observable frequency content of the pressure signal. The raw data file is saved in a binary format, and a self-developed MATLAB script is used to import the data for analysis.

2.3 Model Wind Turbine in Turbulent Shear Flow

Descriptions of the experimental facility and the active grid used in this experiment can be found in *Article III*. As the active grid employed here has the exact same control protocol as the active grid used in *Article I*, details of it will not be repeated here and the reader is instead directed to read Section 2.1.1 for an idea of the design and operation of this active grid. A detailed description of the model wind turbine used can also be found in *Article III*. We will only address particle image velocimetry (PIV) in this section.

2.3.1 Particle Image Velocimetry

Particle image velocimetry (PIV) is a non-intrusive optical flow measurement technique that can capture instantaneous 2D or 3D flow fields. For the purpose of this section, we will focus only on 2D planar PIV as this is the primary measurement

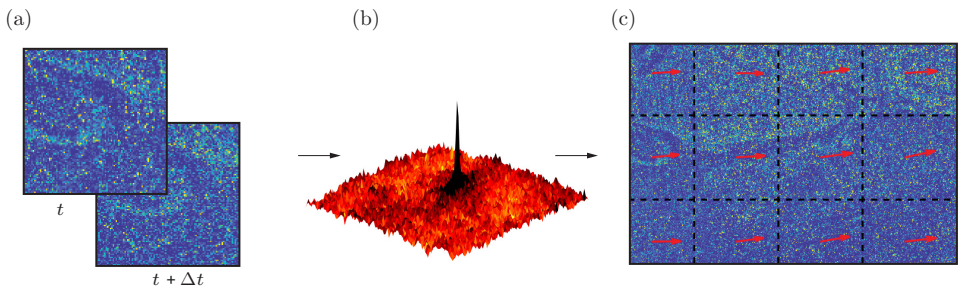

Figure 2.5: A high-level description for calculating velocity vector fields from raw PIV images. (a) Representative interrogation windows for two successive frames that form an image set. (b) Cross correlation between the two frames, the peak signifies the displacement of the particle clusters in the second frame, from the centre of the interrogation window. (c) Representative velocity vector field for each interrogation window, calculated from the displacement of the peak in the cross correlation. The data shown here are self-acquired and the schematic is original.

method used for this experiment. In this section, only a high level overview of the technique will be given, for more details, the interested reader is directed to the book by Raffel et al. (1998). 2D planar PIV works on the principle of correlating particle clusters or other flow-tracking features between two quick successive images, taken with a time difference Δt. The algorithm tracks the physical displacement of these clusters or features through 2D cross-correlation, and in combination with the known Δt, the velocity field can be calculated. Figure 2.5 shows a representation of the procedure described for 2D planar PIV. Please note that the interrogation windows shown in figure 2.5 do not represent the true size of the interrogation windows used, which typically is on the order of tens of pixels in terms of length across the window. The example shown here is of arbitrary size to show more clearly flow features traced by the particle clusters. To transform the results from the image space to physical space, a calibration is performed by taking a snapshot of a target with known markers with pre-determined physical positions (such as a ruler or a specifically made calibration target), and then the appropriate mapping can be performed to map the pixels onto physical space.

The particles mentioned here are seeding particles injected into the flow. They are typically on the order of μm or tens of μm in diameter, depending on the working fluid, field of view (FOV), application, and other factors. Those used for water or other liquid facilities can be made out of plastic, glass, or other insoluble material, while those for air applications are typically vapourized oil or other smoke fluid droplets. As this experiment is conducted in a wind tunnel facility, vapourized

smoke fluid is used to create the seeding particles for the flow. Illumination is typically provided by a laser sheet synchronized to the camera. The sheet should be as thin as possible to minimize cross-plane noise from the particles not in the interrogation plane, while at the same time bright enough to sufficiently illuminate enough particles in the plane.

For our particular experiment, two laser sheets and two cameras are used to create an extended field of view. The details of the physical set up as well as the processing procedure can be found in *Article III*. Here, however, we will go into more details on the stitching method used to combine the velocity vector fields taken by the two cameras.

Figure 2.6 shows a high-level overview of the stitching process of two example instantaneous velocity fields. The overlapping region between the two fields measures about 71 mm in length in the streamwise direction, or about 14% of the individual fields of view. The two fields are first aligned according to the calibrated physical coordinates. Fine adjustments are made visually to account for any inaccuracies in the calibration. The same fine adjustment values are used for all of the images. Next, weighting functions are applied to the u_1 field within the overlapping region. The weighting function used here is a blend of the error and the linear functions. For field A, the weighting function W_1 goes from 1 at the start of the overlapping region to 0 at the end. The weighting function for field B is simply $W_2 = 1 - W_1$. Overall, the final velocity within the overlapping region is calculated as $u_1 = u_{1,A}W_1 + u_{1,B}W_2$.

The weighting function itself, as mentioned, is a blend of the error function and the linear function. Figure 2.7 shows the steps taken to arrive at the final weighting function used for the stitching. The linear function works well for blending the two u_1 fields together in the middle portion of the overlapping region. However, due to the discontinuity in its slope at the ends, footprint of the weighting function can be detected in the stitched fields. The error function is introduced to mitigate this problem by providing a smooth transition in the weighting function slopes near the border of the overlapping region.

The error function is defined as

$$erf(x) = \frac{2}{\sqrt{\pi}} \int_0^x e^{-t^2} \mathrm{d}t. \tag{2.6}$$

For our purposes, we have evaluated the error function on the domain $[-\pi,\ \pi]$, and have made the following linear transform:

$$W_{erf} = \frac{1 - erf(x)}{2}, \tag{2.7}$$

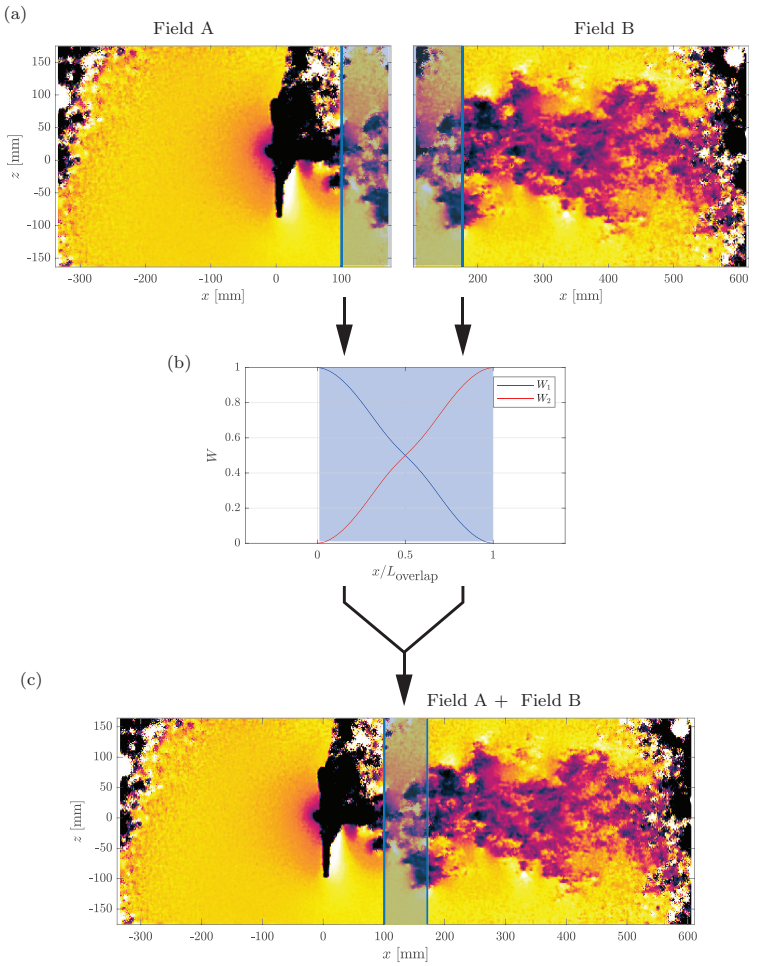

Figure 2.6: Schematic of the stitching procedure: (a) The two separate instantaneous u_1 fields, the overlapping regions are marked by the two blue rectangles. The model wind turbine is the black region just upstream of the overlapping region in Field A; (b) the weighting function for the u_1 fields in the overlapping regions of A and B, the x-axis is normalized by the length of the overlap; (c) combined u_1 field.

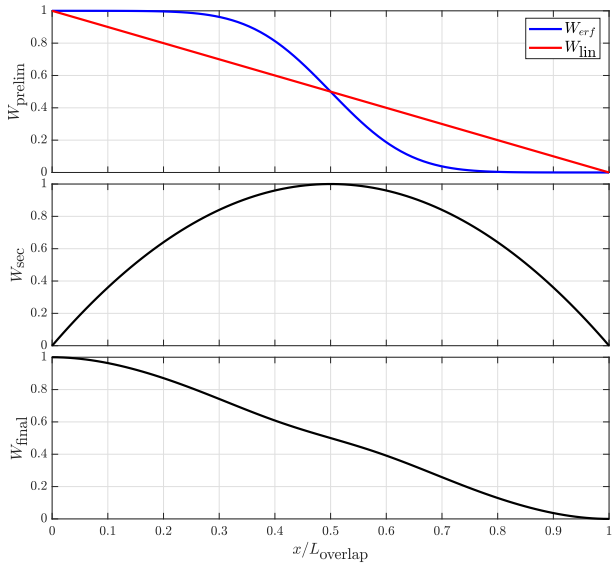

Figure 2.7: Procedure for arriving at the final weighting function W_{final}, showing the initial linear and error weighting functions as well as the secondary weighting function.

so that W_{erf} would go from 1 to 0 within the evaluated domain. The domain itself is also normalized afterwards to span [0, 1].

The linear weighting function W_{lin} is simply

$$W_{\text{lin}} = -x + 1 \quad x \in [0,\ 1]. \tag{2.8}$$

To combine the two preliminary weighting functions, we employ a secondary weighting function, defined as

$$W_{\text{sec}} = -4x(x-1) \quad x \in [0,\ 1]. \tag{2.9}$$

This function has the property that the values at the ends are 0, while at the midpoint of the domain, it is unity.

The final weighting function is calculated as

$$W_{\text{final}} = W_{erf}(1 - W_{\text{sec}}) + W_{\text{lin}} W_{\text{sec}}. \tag{2.10}$$

This weighting function combines the smooth slope change of the error function near the edge of the overlapping region with the good stitching performance of the

linear function within the region itself. The final stitched fields show no discernible discontinuities in the instantaneous velocity fields, the time-averaged velocity fields, and the higher order turbulence statistics fields.

Lastly, the final stitched fields are cropped to remove the regions with low signal-to-noise ratio near the extreme ends of the field of view, and masking is put on the model turbine region and its shadow. However, these are not applied during the actual vector field computation or the stitching procedure, and are only added to the plots in the end to make them more clear and readable. Thus, they do not affect the numerical computation of the velocity vector field, and therefore figure 2.6 does not include the cropping or the masks in the stitched field.

Chapter 3

Summaries of the research articles and future work

This thesis so far has described a project for experimentally investigating the effects of turbulent flows on topics related to the operation of a wind turbine. The background flow of a turbulent boundary layer is first investigated, followed by an examination into how the aerodynamic forces on a wind turbine airfoil cross section are affected by FST. It culminates in the investigation of a complete model wind turbine in turbulent shear flows. Chapter 1 reviewed the historical research and advances in the field of grid turbulence research, turbulent boundary layers, airfoils under the influence of FST, and wind turbines and turbulent shear flows. It also identified some research gaps that this project will seek to address, culminating in a list of objectives for this project. In Chapter 2, we described the experimental facilities and the methods that will be employed to carry out the intended research. Each of the three topics is investigated in a different facility with different methods used.

In this chapter, the results of the investigations into these three topics will be summarized, with particular attention paid to how they address the research gaps identified in Chapter 1. *Article I* focuses on how a spatially developing turbulent boundary layer is influenced by freestream turbulence, which in itself is also spatially developing. *Article II* examines the effects of freestream turbulence on the aerodynamic performance of a wind turbine airfoil. Lastly, *Article III* looks into the near-field of a model wind turbine in different turbulent shear flows, with specific attention paid to the induction zone and the near-wake. Together, these three research articles investigate how turbulence affects the operation of a wind turbine from the background flow perspective all the way up to the complete turbine level.

3.1 Article Summaries

Article I

Spatial development of a turbulent boundary layer subjected to freestream turbulence

Yannick Jooss, Leon Li, Tania Bracchi and R. Jason Hearst

J. Fluid Mechanics, Volume 911, A4, 25 January 2021

Article I investigated the streamwise spatial development of a turbulent boundary layer under the influence of freestream turbulence, which in itself is also spatially evolving. The experiments were performed in the new water channel facility at NTNU, and an active grid was used to generate four different turbulent inflow conditions, with turbulence intensities ranging from 3.2% to 12.5% measured at $x_1/M = 35$, where M is the grid mesh length. Laser Doppler Velocimetry was used to characterize both the freestream turbulence statistics and the boundary layer velocity profiles at three different streamwise locations, $x_1/M = 35$, 55, and 95.

As the freestream turbulence decays in the streamwise direction, its influence on the characteristics of a turbulent boundary layer wanes. This can be seen in three major areas. The first is the suppression of the wake region. It has been shown in literature that under high freestream turbulence, the mean velocity profile of the boundary layer does not exhibit a distinct wake region after the log-layer. It is shown in this study that the wake region returns when the freestream turbulence intensity drops below a certain level. Secondly, the near-wall peak in the velocity fluctuation profile shows behaviour that are dependent on the freestream turbulence intensity. Under high intensity inflows, the near-wall peak decreases as the boundary layer evolves downstream, suggesting a correlation to the decaying freestream turbulence. This is in contrast to low intensity cases where the peak grows, similar to how canonical turbulent boundary layers develop without the influence of freestream turbulence. Lastly, behaviour of the outer peak in the velocity fluctuation spectrograms suggests two mechanisms of formation. When the freestream turbulence intensity is high, the peak appears to be driven directly by the FST. On the other hand, when the intensity is low, this peak reverts back to being generated by natural development of the turbulent boundary layer itself, again similar to what is observed for canonical turbulent boundary layers without external influence from the freestream. Overall, the FST does not permanently mature the TBL, as when the freestream turbulence intensity decays, the boundary layer "devolves" to a less mature state. This was not predicted by previous results which were largely only measured at single points.

This work addresses the existing gap in literature on the spatial development of

turbulence boundary layers under the influence of freestream turbulence. Previous works in literature looked into either the spatial development of canonical boundary layers without freestream turbulence, or the influence of freestream turbulence at one streamwise location. This work contributes to bridging the gap between the two. It has also identified that characterizing turbulent boundary layers requires the consideration of the relative spatial evolution between the freestream turbulence and the turbulent boundary layer itself.

Article II

The influence of freestream turbulence on the temporal pressure distribution and lift of an airfoil

Leon Li and R. Jason Hearst

J. Wind Engineering & Industrial Aerodynamics, Volume 209, February 2021

Article II investigated the influence of freestream turbulence on the pressure and lift characteristics of a reference wind turbine airfoil. The work was conducted in the large low-speed wind tunnel at NTNU, and seven different inflow conditions were created through the use of passive turbulence grids. The turbulence intensity ranged from 0.40% to 5.39%. The flow inhomogeneity at the measurement location is less than 0.9% for the most turbulent inflow case. This is similar to the values reported by Wang et al. (2014). Pressure distribution measurements around the airfoil were taken at multiple angles of attack via a pressure scanner embedded inside the test model. The primary objective of this study is to examine both the mean and the temporal behaviours of the pressure distributions and lift characteristics of this airfoil under the influence of freestream turbulence.

It is found that an increase in freestream turbulence intensity generally increases the lift coefficient across the angles of attack tested. The lift slope in the linear regime as well as the maximum lift generally increases with increasing FST, while the stall angle remains relatively constant. There is a peculiar behaviour when the turbulence intensity is between 1% and 2%, where the lift coefficient within the linear operating regime of the airfoil decreased. Further analysis into the frequency content of the pressure fluctuations reveals that for those cases, near the trailing edge of the airfoil, there is a peak near $fc/U_0 = 1$ in the pressure fluctuation spectra, where f is the frequency of the peak, c is the chord length of the airfoil, and U_0 is the mean freestream velocity. It is postulated that this peak is the signature of a flow instability excited by the incoming turbulence that leads to a reduction in the time-averaged lift, and that this excitation diminishes with higher turbulence intensities.

This research isolated the effects of freestream turbulence from other factors such as incoming flow inhomogeneity, Reynolds number dependence, and varying airfoil profiles. The literature has shown somewhat contradictory results on how freestream turbulence affects the aerodynamics of airfoils, in particular the behaviour of the lift slope in the linear operating regime. We postulate that some of these contradictions could be attributed to one or more of the three factors mentioned at the beginning of this paragraph, in particular, flow inhomogeneity. Furthermore, the research is novel in its combination of looking into both the mean and the spectral characteristics of the pressure and lift. Previous studies have either stopped just short of examining the frequency content of the pressure fluctuations on an airfoil under the influence of freestream turbulence, or they focused on simpler geometries such as a cylinder (Blackburn and Melbourne 1996).

Article III

The near-field of a lab-scale wind turbine in tailored turbulent shear flows
Leon Li, R. Jason Hearst, Manuel A. Ferreira and Bharathram Ganapathisubramani
Renewable Energy, Volume 149, April 2020

Article III investigated the near-field of a model wind turbine under different turbulent shear flows. The experiment was conducted in the open-loop wind tunnel at the University of Southampton, where an active grid was used to create seven incoming flows with different combinations of shear profiles and turbulence intensities. The flow field was captured by 2D planar PIV.

Building on the novel work of Hearst and Ganapathisubramani (2017), where for the first time, different turbulent shear flows could be created by a single set up, this work opens up the possibility for significant advancement in our experimental abilities to explore the flow field around wind turbines under simulated atmospheric boundary layer flows. Through this work, it is shown that the mean velocity profile in the near wake could be considered as a superposition of wake profile caused by a uniform inflow and the incoming shear profile. This results in a higher velocity shear gradient in the wake toward the high-speed side of the shear flow, leading to an increase in turbulence production, and thus larger velocity fluctuations on that side. This could have adverse effects on downstream turbines as it leads to unequal loading across the rotor sweep area due to turbulent fluctuations. The power fluctuations measured on the turbine motor scales proportionally with the incoming turbulence intensity, regardless of shear profiles. Furthermore, the percentage difference between the two formulations of U_{eq} by Wagner et al. (2009) and Choukulkar et al. (2016) (eqs. 1.12 and 1.13 respectively, the latter takes velocity fluctuations into account) in the near wake is more affected by the freestream

turbulence intensity rather than the shear profile. As U_{eq} in the near wake can be considered as an indicator of the kinetic energy available for the downstream turbines, the results suggest that turbulence intensity plays a bigger role in the power behaviour of a wind turbine than shear profile.

3.2 Future Work

Several possibilities exist to extend the present work of this thesis. This section will examine them from the perspective of each of the research articles.

The active grid used to generate the different freestream turbulent flows could easily be adapted via the methods described in Hearst and Ganapathisubramani (2017) to create turbulent shear flows. While insights are gained into examining the spatial evolution of a naturally developing turbulent boundary layer under the influence of freestream turbulence, it may be more relevant to wind energy research to examine the spatial development of different turbulent shear flows, as they are more akin to the vast variety of expected inflow conditions for real wind turbines. This is particularly relevant because ideally the spatial development of the turbulent flow would be minimal. In this way, the investigation of say, the wake of a turbine, would be subject to the same turbulent conditions at every point in the wake's evolution. Using standard grid turbulence, this isn't the case because the background turbulence would be decaying. A well-designed shear flow could potentially result in an extended streamwise domain where both the mean shear velocity profiles and the turbulence intensity can remain relatively constant.

For the airfoil under the influence of FST experiment, again an active grid could be used instead of passive grids to generate flows with a greater range of turbulence intensity. In fact one such device has already been installed and made operational for the same wind tunnel since the publication of the article. In addition, PIV could be employed to capture the flow field around the airfoil, especially near the trailing edge, to capture the flow phenomena that cause the fluctuations seen in the pressure and lift force spectra when the freestream turbulence intensity is between 1% and 2%. Another suggestion is to examine the properties of several different airfoil profiles. While the airfoil used is a reference wind turbine airfoil that has been studied extensively in literature, it is nonetheless a specifically designed airfoil for a practical application. It would be interesting to test generic airfoils such as the NACA 00XX symmetric airfoils to categorize the separate effect of airfoil profiles on its aerodynamic behaviour under the same inflow conditions. Finally, the experimental set up could be adapted to acquire dynamic aerodynamic performance data as opposed to the steady-state conditions in *Article II*.

The investigation into the near-field of a model wind turbine could be extended to

examine the mid- to far-wake behind the turbine. This could provide a more complete picture of how the wake evolves spatially under different turbulent shear flow conditions, thus quantifying the flow field conditions at more realistic streamwise locations for any downstream turbines.

Lastly, while this thesis focuses on topics related to wind turbines, all of the experimental set ups in the three research articles could be extended to include more topics. Simple canonical objects such as cylinders or spheres could be placed in the facilities to examine how different freestream turbulent flows affect their aerodynamic behaviour. The possibilities are broad and as far as it is practically feasible, future research topics are only limited by our imagination.

3.3 Concluding remarks

The effect of turbulent incoming flow has been investigated on topics inspired by wind energy research. These topics cover the background flow experienced by a wind turbine, the airfoil profile of a wind turbine blade, and lastly, the near-field of a model wind turbine. Each topic constitutes a separate experimental investigation using a variety of measurement methods, and the effect of turbulence on each is best summarized by directly addressing the topics listed in Chapter 1:

1. *The influence of freestream turbulence on the spatial development of a turbulent boundary layer.*

   It was shown that while freestream turbulence can induce features seen only in high Reynolds number turbulent boundary layers, it does not permanently mature the boundary layer. As the freestream turbulence decays, the boundary layer devolves into a less mature state that is more akin to naturally developing boundary layers of low to moderate Reynolds numbers. Freestream turbulence was found to have marked effects on the development of turbulent boundary layers with regard to the wake region, and the inner and outer velocity fluctuation peaks.

2. *The influence of freestream turbulence on the aerodynamic performance of a wind turbine airfoil.*

   Moving from the background flow to the component level of a wind turbine, elevated freestream turbulence level is found to improve the lift and stall characteristics of a wind turbine airfoil. There is evidence that the inflow homogeneity plays an important role on the aerodynamic behaviour, and this could be the source of some of the discrepancies regarding the behaviour of lift slopes seen in literature. Low intensity turbulence is found to cause a flow

instability near the trailing edge, which has the overall effect of reducing the lift in the linear operating regime of the airfoil.

3. *The influence of turbulent shear flow on the near field of a lab-scaled model wind turbine.*

   Lastly, moving to the system level, a model wind turbine is placed in different turbulent shear flows to investigate their influence on the near-field behaviour. Higher levels of turbulence production and velocity fluctuations are found on the high-velocity side of the wake due to the increased mean velocity gradient found there. This can lead to uneven and fluctuating aerodynamic loads on the downstream turbines. The power fluctuations are found to be proportional to the turbulence intensity, regardless of the shear profile. The kinetic energy available in the near-wake is also influenced more by the inflow turbulence level than the shear profile.

The primary aim of this thesis is to systematically investigate how turbulent flows influence topics related to wind turbines from three stages with increasing complexity. This work provides a complete picture of how wind turbines behave in turbulent flows at least at lab-scale, and that the work presented here contributes to the growing body of wind energy research, and by extension, provides inspirations for future investigations into the effect of turbulence on other objects and flow phenomena.

Bibliography

Adaramola, M. S. and Krogstad, P. Å. (2011), 'Experimental investigation of wake effects on wind turbine performance', *Renew. Energ.* **36**, 2078–2086.

Adrian, R. and Yao, C. (1986), 'Power spectra of fluid velocities measured by laser doppler velocimetry', *Exp. Fluids* **5**(1), 17–28.

Aubrun, S., Loyer, S., Hancock, P. and Hayden, P. (2013), 'Wind turbine wake properties: Comparison between a non-rotating simplified wind turbine model and a rotating model', *J. Wind Eng. Ind. Aerod.* **120**, 1–8.

Barthelmie, R. J., Pryor, S. C., Frandsen, S. T., Hansen, K. S., Schepers, J. G., Rados, K., Schlez, W., Neubert, A., Jensen, L. E. and Neckelmann, S. (2010), 'Quantifying the impact of wind turbine wakes on power output at offshore wind farms', *J. Atmos. Ocean. Tech.* **27**.

Benedict, L. and Gould, R. (1996), 'Towards better uncertainty estimates for turbulence statistics', *Exp. Fluids* **22**(2), 129–136.

Benedict, L., Nobach, H. and Tropea, C. (2000), 'Estimation of turbulent velocity spectra from laser doppler data', *Meas. Sci. Technol.* **11**(8), 1089.

Bianchi, F. D., de Battista, H. and Mantz, R. J. (2006), *Wind Turbine Control Systems: Principles, Modelling, and Gain Scheduling Design*, Springer.

Blackburn, H. M. and Melbourne, W. H. (1996), 'The effect of free-stream turbulence on sectional lift forces on a circular cylinder', *J. Fluid Mech.* **306**, 267–292.

Blair, M. (1983a), 'Influence of free-stream turbulence on turbulent boundary layer heat transfer and mean profile development, part i—experimental data', *Trans. ASME: J. Heat Transfer* **105**(1), 33–40.

Blair, M. (1983b), 'Influence of free-stream turbulence on turbulent boundary layer heat transfer and mean profile development, part ii—analysis of results', *Trans. ASME: J. Heat Transfer* **105**(1), 41–47.

Bossuyt, J., Howland, M. F., Meneveau, C. and Meyers, J. (2017), 'Measurement of unsteady loading and power output variability in a micro wind farm model in a wind tunnel', *Exp. Fluids* **58**(1), 1–17.

Boyer, L. and Searby, G. (1986), 'Random sampling: Distortion and reconstruction of velocity spectra from fast fourier-transform analysis of the analog signal of a laser doppler processor', *J. Appl. Phys.* **60**(8), 2699–2707.

Butler, R. J., Byerley, A. R., VanTreuren, K. and Baughn, J. W. (2001), 'The effect of turbulence intensity and length scale on low-pressure turbine blade aerodynamics', *Int. J. Heat Fluid Fl.* **22**(2), 123–133.

Cal, R. B., Lebrón, J., Castillo, L., Kang, H. S. and Meneveau, C. (2010), 'Experimental study of the horizontally averaged flow structure in a model wind-turbine array boundary layer', *J. Renew. Sustain. Ener.* **2**(1), 013106.

Cao, N., Ting, D. S.-K. and Carriveau, R. (2011), 'The Performance of a High-Lift Airfoil in Turbulent Wind', *Wind Engineering* **35**(2), 179–196.

Cardesa, J. I., Vela-Martín, A. and Jiménez, J. (2017), 'The turbulent cascade in five dimensions', *Science* **357**, 782–784.

Carter, D., Petersen, A., Amili, O. and Coletti, F. (2016), 'Generating and controlling homogenous air turbulence using random jet arrays', *Exp. Fluids* **57**.

Castro, I. (1984), 'Effects of free stream turbulence on low reynolds number boundary layers', *Trans. ASME: J. Fluids Engng* **106**(3), 298–306.

Cekli, H. E. and van de Water, W. (2010), 'Tailoring turbulence with an active grid', *Exp. Fluids* **49**, 409–416.

Chamorro, L. P. and Porté-Agel, F. (2009), 'A Wind-Tunnel Investigation of Wind-Turbine Wakes: Boundary-Layer Turbulence Effects', *Bound. Layer Meteor.* **132**, 129–149.

Chauhan, K. A., Monkewitz, P. A. and Nagib, H. M. (2009), 'Criteria for assessing experiments in zero pressure gradient boundary layers', *Fluid Dyn. Res.* **41**(2), 021404.

Choukulkar, A., Pichugina, Y., Clark, C., Calhoun, R., Banta, R., Brewer, A. and Hardesty, M. (2016), 'A new formulation for rotor equivalent wind speed for wind resource assessment and wind power forecasting', *Wind Energy* **19**(8), 1439–1452.

Coles, D. (1956), 'The law of the wake in the turbulent boundary layer', *J. Fluid Mech.* **1**(2), 191–226.

Comte-Bellot, G. and Corrsin, S. (1966), 'The use of a contraction to improve the isotropy of grid-generated turbulence', *J. Fluid Mech.* **25**, 657–682.

Counihan, J. (1969), 'An improved method of simulating an atmopsheric boundary layer in a wind tunnel', *Atmos. Environ.* **3**, 197–214.

Counihan, J. (1973), 'Simulation of an adiabatic urban boundary layer in a wind tunnel', *Atmos. Environ.* **7**, 673–689.

Devinant, P., Laverne, T. and Hureau, J. (2002), 'Experimental study of wind-turbine airfoil aerodynamics in high turbulence', *J. Wind Eng. Ind. Aerod.* **90**(6), 689–707.

Dimitrov, N., Natarajan, A. and Kelly, M. (2015), 'Model of wind shear conditional on turbulence and its impact on wind turbine loads', *Wind Energy* **18**(11), 1917–1931.

Dogan, E., Hanson, R. and Ganapathisubramani, B. (2016), 'Interactions of large-scale free-stream turbulence with turbulent boundary layers', *J. Fluid Mech.* **802**, 79–107.

Dogan, E., Hearst, R. J. and Ganapathisubramani, B. (2017), 'Modelling high Reynolds number wall-turbulence interactions in laboratory experiments using large-scale free-stream turbulence', *Philos. Trans. A. Math. Phys. Eng. Sci.* .

Eitel-Amor, G., Örlü, R. and Schlatter, P. (2014), 'Simulation and validation of a spatially evolving turbulent boundary layer up to $Re_\theta = 8300$', *Int. J. Heat Fluid Fl.* **47**, 57–69.

Ertunç, O., Özyilmaz, N., Lienhart, H., Durst, F. and Beronov, K. (2010), 'Homogeneity of turbulence generated by static-grid structures', *J. Fluid Mech.* **654**, 473–500.

Esteban, L. B., Dogan, E., Rodríguez-López, E. and Ganapathisubramani, B. (2017), 'Skin-friction measurements in a turbulent boundary layer under the influence of free-stream turbulence', *Exp. Fluids* **58**(9), 1–7.

Ferrante, A. and Elghobashi, S. (2004), 'On the physical mechanisms of drag reduction in a spatially developing turbulent boundary layer laden with microbubbles', *J. Fluid Mech.* **503**, 345–355.

Gad-El-Hak, M. and Corrsin, S. (1974), 'measurements of the nearly isotropic turbulence behind a uniform jet grid', *J. Fluid Mech.* **62**, 115–143.

Ganapathisubramani, B. (2018), 'Law of the wall for small-scale streamwise turbulence intensity in high-reynolds-number turbulent boundary layers', *Phy. Rev. Fluids* **3**(10), 104607.

Gaster, M. (1967), *The structure and behaviour of laminar separation bubbles*, NPL.

Gaumond, M., Réthoré, P.-E., Bechmann, A., Ott, S., Larsen, G. C., Peña, A. and Hansen, K. S. (2012), Benchmarking of wind turbine wake models in large offshore wind farms, *in* 'Proceedings of the Science of Making Torque from Wind 2012'.

Hancock, P. and Bradshaw, P. (1989), 'Turbulence structure of a boundary layer beneath a turbulent free stream', *J. Fluid Mech.* **205**, 45–76.

Hancock, P. E. and Bradshaw, P. (1983), 'The effect of free-stream turbulence on turbulent boundary layers', *Trans. ASME: J. Fluids Eng.* **105**(3), 284–289.

Hattori, Y., Yamamoto, M., Eguchi, Y., Kondo, K., Suto, H. and Tanaka, N. (2007), 'A wind tunnel experiment on wake structure of a wind turbine', *KAJIM Technical Research Institute, Kajim* .

Hearst, R. J., Dogan, E. and Ganapathisubramani, B. (2018), 'Robust features of a turbulent boundary layer subjected to high-intensity free-stream turbulence', *J. Fluid Mech.* **851**, 416–435.

Hearst, R. J. and Ganapathisubramani, B. (2017), 'Tailoring incoming shear and turbulence profiles for lab-scale wind turbines', *Wind Energy* **20**(12), 2021–2035.

Hearst, R. J., Gomit, G. and Ganapathisubramani, B. (2016), 'Effect of turbulence on the wake of a wall-mounted cube', *J. Fluid Mech.* **804**, 513–530.

Hearst, R. J. and Lavoie, P. (2014), 'Decay of turbulence generated by a square-fractal-element grid', *J. Fluid Mech.* **741**, 567–584.

Hearst, R. J. and Lavoie, P. (2015), 'The effect of active grid initial conditions on high Reynolds number turbulence', *Exp. Fluids* **56**, 1–20.

Hoffmann, J. A. (1991), 'Effects of Freestream Turbulence on the Performance Characteristisc of an Airfoil', *AIAA J.* **29**(9), 1353–1354.

Huang, R. F. and Lee, H. W. (1999), 'Effects of Freestream Turbulence on Wing-Surface Flow and Aerodynamic Performance', *J. Aircraft* **36**(6), 965–972.

Hultmark, M. and Smits, A. J. (2010), 'Temperature corrections for constant temperature and constant current hot-wire anemometers', *Meas. Sci. Technol.* **21**(10), 105404.

Hutchins, N. and Marusic, I. (2007), 'Evidence of very long meandering features in the logarithmic region of turbulent boundary layers', *J. Fluid Mech.* **579**, 1–28.

Isaza, J., Salazar, R. and Warhaft, Z. (2014), 'On grid-generated turbulence in the near- and far field regions', *J. Fluid Mech.* **753**, 402–426.

Kamada, Y., Maeda, T., Murata, J., Toki, T. and Tobuchi, A. (2011), 'Effects of Turbulence Intensity on Dynamic Characterstics of Wind Turbine Airfoil', *Journal of Fluid Science and Technology* **6**(3), 333–341.

Kannuluik, W. and Carman, E. (1951), 'The temperature dependence of the thermal conductivity of air', *Aust. J. Chem.* **4**(3), 305–314.

Kistler, A. and Vrebalovich, T. (1961), 'Turbulence measurements at the 8 by 10-foot cooperative wind tunnel', *Jet Prop. Lab. Res. Summary* pp. 36–4.

Knebel, P., Kittel, A. and Peinke, J. (2011), 'Atmospheric wind field conditions generated by active grids', *Exp. Fluids* **51**, 471–481.

Kolmogorov, A. N. (1941a), 'The local structure of turbulence in incompressible viscous fluid for very large Reynolds numbers', *Proc. USSR Acad. Sci.* **30**, 301–305.

Kozul, M., Hearst, R. J., Monty, J. P., Ganapathisubramani, B. and Chung, D. (2020), 'Response of the temporal turbulent boundary layer to decaying free-stream turbulence', *J. Fluid Mech.* **896**.

Larssen, J. V. and Devenport, W. J. (2011), 'On the generation of large-scale homogenous turbulence', *Exp. Fluids* **50**, 1207–1223.

Lavoie, P., Djenidi, L. and Antonia, R. A. (2007), 'Effects of initial conditions in decaying turbulence generated by passive grids', *J. Fluid Mech.* **585**, 395–420.

Li, Q. A., Kamada, Y., Maeda, T., Murata, J. and Yusuke, N. (2016), 'Effect of turbulence on power performance of a Horizontal Axis Wind Turbine in yawed and no-yawed flow conditions', *Energy* **109**, 703–711.

Makita, H. (1991), 'Realization of a large-scale turbulence field in a small wind tunnel', *Fluid Dyn. Res.* **8**, 53–64.

Maldonado, V., Castillo, L., Thormann, A. and Meneveau, C. (2015), 'The role of free stream turbulence with large integral scale on the aerodynamic performance of an experimental low Reynolds number S809 wind turbine blade', *J. Wind Eng. Ind. Aerod.* **142**, 246–257.

Marusic, I., Chauhan, K., Kulandaivelu, V. and Hutchins, N. (2015), 'Evolution of zero-pressure-gradient boundary layers from different tripping conditions', *J. Fluid Mech.* **783**, 379–411.

Medici, D. and Alfredsson, P. H. (2006), 'Measurements on a wind turbine wake: 3D effects and bluff body vortex shedding', *Wind Energy* **9**, 219–236.

Michálek, J., Monaldi, M. and Arts, T. (2012), 'Aerodynamic Performance of a Very High Lift Low Pressure Turbine Airfoil (T106C) at Low Reynolds and High Mach Number With Effect of Free Stream Turbulence Intensity', *J. Turbomach.* **134**.

Milan, P., Wächter, M. and Peinke, J. (2013), 'Turbulent Character of Wind Energy', *Phys. Rev. Lett.* **110**(138701).

Mücke, T., Kleinhans, D. and Peinke, J. (2011), 'Atmospheric turbulence and its influence on the alternating loads on wind turbines', *Wind Energy* **14**(2), 301–316.

Mueller, T. J., Pohlen, L. J., Conigliaro, P. E. and Jansen, B. J. (1983), 'The influence of free-stream disturbances on low Reynolds number airfoil experiments', *Exp. Fluids* **1**(1), 3–14.

Mydlarski, L. and Warhaft, Z. (1996), 'On the onset of high-Reynolds-number grid-generated wind turnnel turbulence', *J. Fluid Mech.* .

Neunaber, I., Hölling, M., Whale, J. and Peinke, J. (2021), 'Comparison of the turbulence in the wakes of an actuator disc and a model wind turbine by higher order statistics: A wind tunnel study', *Renew. Energ.* **179**, 1650–1662.

Ouahabi, A., Depollier, C., Simon, L. and Koume, D. (1998), 'Spectrum estimation from randomly sampled velocity data [ldv]', *IEEE T. Instrum. Meas.* **47**(4), 1005–1012.

Owen, P. R. and Klanfer, L. (1953), On the Laminar Boundary Layer Separation from the Leading Edge of a Thin Aerofoil, Technical report, Aeronautical Research Council, London (United Kingdom).

Porté-Agel, F., Bastankhah, M. and Shamsoddin, S. (2020), 'Wind-turbine and wind-farm flows: a review', *Boundary-Layer Meteorology* **174**(1), 1–59.

Prandtl, L. (1904), 'Über flüssigkeitsbewegung bei sehr kleiner reibung (on the fluid motion at very low friction)', *Verhandl. III, Internat. Math.-Kong., Heidelberg, Teubner, Leipzig, 1904* pp. 484–491.

Raffel, M., Willert, C. E., Kompenhans, J. et al. (1998), *Particle image velocimetry: a practical guide*, Vol. 2, Springer.

Raushan, P. K., Singh, S. K. and Debnath, K. (2018), 'Grid generated turbulence under the rigid boundary influence', *J. Wind Eng. Ind. Aerod.* **182**, 252–261.

Ravi, S., Watkins, S., Watmuff, J., Massey, K., Petersen, P. and Marino, M. (2012a), 'Influence of large-scale freestream turbulence on the performance of a thin airfoil', *AIAA J.* **50**(11).

Ravi, S., Watkins, S., Watmuff, J., Massey, K., Petersen, P., Marino, M. and Ravi, A. (2012b), 'The flow over a thin airfoil subjected to elevated levels of freestream turbulence at low Reynolds numbers', *Exp. Fluids* **53**, 637–653.

Reynolds, O. (1883), 'XXIX. An experimental investigation of the circumstances which determine whether the motion of water shall be direct or sinuous, and of the law of resistance in parallel channels', *Philosophical Transactions of the Royal society of London* (174), 935–982.

Richardson, L. F. (1922), *Weather prediction by numerical process*, Cambridge university press.

Rind, E. and Castro, I. P. (2012), 'On the effects of free-stream turbulence on axisymmetric disc wakes', *Exp. Fluids* **53**, 301–318.

Sarlak Chivaee, H. and Sørensen, J. N. (2018), Characterisation of Mushroom Structures on Airfoils: CFD and Wind Tunnel Investigation, *in* '21st Australasian Fluid Mechanics Conference'.

Sarlak, H., Frère, A., Mikkelsen, R. and Sørensen, J. N. (2018), 'Experimental Investigation of Static Stall Hysteresis and 3-Dimensional Flow Structures for an NREL S826 Wing Section of Finite Span', *Energies* **11**(6).

Schneemann, J., Knebel, P., Milan, P. and Peinke, J. (2010), Lift Measurements in Unsteady Flow Conditions, *in* 'DEWEK 2010'.

Schottler, J., Hölling, A., Peinke, J. and Hölling, M. (2017), 'Brief communication: On the influence of vertical wind shear on the combined power output of two model wind turbines in yaw', *Wind Ener. Sci.* **2**, 439–442.

Sharp, N. S., Neuscamman, S. and Warhaft, Z. (2009), 'Effects of large-scale free stream turbulence on a turbulent boundary layer', *Phy. Fluids* **21**(9), 095105.

Shen, X. and Warhaft, Z. (2000), 'The anisotropy of the small scale strucutre in high Reynolds ($R_\lambda \sim 1000$) turbulent shear flow', *Phys. Fluids* **12**.

Sicot, C., Aubrun, S., Loyer, S. and Devinant, P. (2006b), 'Unsteady characteristics of the static stall of an airfoil subjected to freestream turbulence level up to 16%', *Exp. Fluids* **41**(4), 641–648.

Sicot, C., Devinant, P., Laverne, T., Loyer, S. and Hureau, J. (2006a), 'Experimental study of the effect of turbulence on horizontal axis wind turbine aerodynamics', *Wind Energy* **9**(4), 361–370.

Smits, A. J. and Marusic, I. (2013), 'Wall-bounded turbulence', *Phys. Today* **66**(9), 25–30.

Stack, J. (1931), Test in the variable density wind tunnel to investigate the effects of scale and turbulence on airfoil characteristics, Technical Report 364, NACA.

Swalwell, K. E., Sheridan, J. and Melbourne, W. H. (2001), The Effect of Turbulence Intensity on Stall of the NACA 0021 Aerofoil, *in* '14^{th} Australasian Fluids Mechanics Conference'.

Talavera, M. and Shu, F. (2017), 'Experimental study of turbulence intensity influence on wind turbine performance and wake recovery in a low-speed wind tunnel', *Renew. Energ.* .

Thole, K. and Bogard, D. (1996), 'High freestream turbulence effects on turbulent boundary layers', *Trans. ASME: J. Fluids Engng* **118**(2), 276–284.

van Kuik, G., Peinke, J., Nijssen, R., Lekou, D., Mann, J., Sørensen, J. N., Ferreira, C., van Wingerden, J.-W., Schlipf, D., Gebraad, P. et al. (2016), 'Long-term research challenges in wind energy–a research agenda by the european academy of wind energy', *Wind Energy Sci.* **1**(1), 1–39.

Vanderwel, C. and Tavoularis, S. (2011), 'Coherent structures in uniformly sheared turbulent flow', *J. Fluid Mech.* **689**, 434–464.

Veers, P., Dykes, K., Lantz, E., Barth, S., Bottasso, C. L., Carlson, O., Clifton, A., Green, J., Green, P., Holttinen, H. et al. (2019), 'Grand challenges in the science of wind energy', *Science* **366**(6464).

Vermeer, L. J., Sørensen, J. N. and Crespo, A. (2003), 'Wind turbine wake aerodynamics', *Prog. Aerosp. Sci.* **39**, 467–510.

Vincenti, P., Klewicki, J., Morrill-Winter, C., White, C. and Wosnik, M. (2013), 'Streamwise velocity statistics in turbulent boundary layers that spatially develop to high reynolds number', *Exp. Fluids* **54**(12), 1–13.

Wagner, R., Antoniou, I., Pedersen, S. M., Courtney, M. S. and Jørgensen, H. E. (2009), 'The influence of the wind speed profile on wind turbine performance measurements', *Wind Energy* **12**, 348–362.

Wagner, R., Courtney, M., Gottschall, J. and Lindelöw-Marsden, P. (2011), 'Accounting for the speed shear in wind turbine power performance measurement', *Wind Energy* **14**, 993–1004.

Wang, S., Zhou, Y., Alam, M. M. and Yang, H. (2014), 'Turbulence intensity and Reynolds number effects on an airfoil at low Reynolds number', *Phys. Fluids* **26**(115107).

Watkins, S., Ravi, S. and Loxton, B. (2010), 'The effect of turbulence on the aerodynamics of low reynolds number wings', *Eng. Lett.* **18**(3).

Wu, X. and Moin, P. (2009), 'Direct numerical simulation of turbulence in a nominally zero-pressure-gradient flat-plate boundary layer', *J. Fluid Mech.* **630**, 5–41.

Wu, X., Moin, P., Wallace, J. M., Skarda, J., Lozano-Durán, A. and Hickey, J.-P. (2017), 'Transitional–turbulent spots and turbulent–turbulent spots in boundary layers', *Proceedings of the National Academy of Sciences* **114**(27), E5292–E5299.

Wu, X., Wallace, J. M. and Hickey, J.-P. (2019), 'Boundary layer turbulence and freestream turbulence interface, turbulent spot and freestream turbulence interface, laminar boundary layer and freestream turbulence interface', *Phy. Fluids* **31**(4), 045104.

You, J. and Zaki, T. A. (2019), 'Conditional statistics and flow structures in turbulent boundary layers buffeted by free-stream disturbances', *J. Fluid Mech.* **866**, 526–566.

You, J. and Zaki, T. A. (2020), 'Turbulent heat-transfer enhancement in boundary layers exposed to free-stream turbulence', *Flow Turbul. Combust.* **104**(2), 381–402.

Publications in full text

Spatial development of a turbulent boundary layer subjected to freestream turbulence

J. Fluid Mech. (2021), *vol*. 911, A4.
Published by Cambridge University Press

doi:10.1017/jfm.2020.967

Spatial development of a turbulent boundary layer subjected to freestream turbulence

Yannick Jooss[1], **Leon Li**[1], **Tania Bracchi**[1] **and R. Jason Hearst**[1],†

[1]Department of Energy and Process Engineering, Norwegian University of Science and Technology, Trondheim NO-7491, Norway

(Received 5 June 2020; revised 18 September 2020; accepted 28 October 2020)

The spatial development of a turbulent boundary layer (TBL) subjected to freestream turbulence (FST) is investigated experimentally in a water channel for friction Reynolds numbers up to $Re_\tau = 5060$. Four different FST intensities are generated with an active grid, ranging from a low-turbulence reference case to $u'_\infty/U_\infty = 12.5\,\%$. Wall-normal velocity scans are performed with laser doppler velocimetry at three positions downstream of the grid. There are two combating influences as the flow develops: the TBL grows while the FST decays. Whilst previous studies have shown the wake region of the TBL is suppressed by FST, the present measurements demonstrate that the wake recovers sufficiently far downstream. For low levels of FST, the near-wall variance peak grows as one moves downstream, whereas high FST results in an initially high variance peak that decays with streamwise position. These results are mirrored in the evolution of the spectrograms, where low FST results in the emergence of an outer spectral peak as the flow evolves, while high FST sees an initially high outer spectral peak decay in space. This finding is significant as it suggests the FST does not permanently mature the TBL ahead of its natural evolution. Finally, it is explicitly demonstrated that it is not sufficient to characterize the TBL solely by conventional parameters such as Re_τ, but that the level of FST and the evolution of the two flows must also be considered.

Key words: homogeneous turbulence, turbulent boundary layers

1. Introduction

Turbulent boundary layers (TBL) exist in a wide range of natural processes and technical applications. Understanding their nature and evolution has been a subject of great interest since the concept was first introduced (Prandtl 1905). The study of TBLs is also important for developing knowledge on diverse problems ranging from how heat is distributed in the atmosphere to the determination of drag forces on aeroplanes and ships (Smits & Marusic 2013). In many of these flows, the freestream above the boundary layer is also turbulent. The characteristics of the so-called freestream turbulence (FST) can vary significantly; two parameters of leading-order significance are the turbulence intensity u'_∞/U_∞, where U_∞ is the freestream velocity and u'_∞ is the root-mean-square of the

† Email address for correspondence: jason.hearst@ntnu.no

velocity fluctuations in the freestream, and the size of the largest scales in the flow, both of which vary depending on the turbulence's origin and state of evolution. Over the past three decades the effect of FST on a canonical zero-pressure-gradient turbulent boundary layer has been studied extensively, e.g. Hancock & Bradshaw (1983, 1989), Castro (1984), Thole & Bogard (1996), Sharp, Neuscamman & Warhaft (2009), Dogan, Hanson & Ganapathisubramani (2016), Dogan, Hearst & Ganapathisubramani (2017), Hearst, Dogan & Ganapathisubramani (2018), Dogan *et al.* (2019) and You & Zaki (2019).

Pioneering work in subjecting a turbulent boundary layer to FST was performed by Hancock & Bradshaw (1983, 1989). Freestream turbulence was generated with two different passive grids in a wind tunnel, and the flow was measured over a flat plate. The freestream turbulence intensity and length scales were also varied by measuring at different downstream positions from the grids. This resulted in a range of $2870 \leqslant Re_\theta \leqslant 5760$, where $Re_\theta = U_\infty \theta/\nu$ is based on the momentum thickness θ. They covered a range of freestream turbulence length scales $L_{u,\infty}$, representing the characteristic length scale of the energy containing eddies, between 0.67 and 2.23 times the boundary layer thickness δ. They found both u'_∞/U_∞ and $L_{u,\infty}$ were significant influencing parameters on the structure of the boundary layer. They combined these concepts in an empirical parameter, $\beta = (u'_\infty/U_\infty)/(L_{u,\infty}/\delta + 2)$, which appeared to correlate well with the wall shear stress and boundary layer wake region in their flows. However, their experiment was not without limitations – for example, the relatively low turbulence intensities, up to a maximum of 5.8 %, and, more importantly, measurement positions as close as 15 mesh lengths (M) downstream of their grids where the flow is typically still inhomogeneous (Ertunç *et al.* 2010; Isaza, Salazar & Warhaft 2014). The measurement position relative to the grid bars could bias the results in this region, and more recent measurements offer words of caution and update these results (Hearst *et al.* 2018; Kozul *et al.* 2020). Several other fluids problems, including flow over aerofoils, for example, have shown sensitivity to being in the inhomogeneous region behind a grid, resulting in strongly contrasting results (Devinant, Laverne & Hureau 2002; Wang *et al.* 2014; Maldonado *et al.* 2015). Castro (1984) looked at the effect of freestream turbulence on turbulent boundary layers at relatively low Reynolds numbers, $500 \leqslant Re_\theta \leqslant 2500$. Two passive grids were used to create the FST with turbulence intensities up to 7 %. It was shown that the skin friction was influenced by both the Reynolds number and the freestream turbulence intensity. Once again measurements were, in part, taken relatively close to the grid, starting from $x/M = 6$.

Similarly, Blair (1983*b*) showed that the skin friction increases with FST in a turbulent boundary layer for $1000 \leqslant Re_\theta \leqslant 7000$. In the second part of his work (Blair 1983*a*), the influence of FST on the shape of the turbulent boundary layer profile was analysed. While the logarithmic region was relatively unaffected by the freestream turbulence, the presence of the wake was found to be strongly dependent on the level of FST. The outer region intermittency was progressively suppressed with increasing turbulence intensity, effectively making the wake region of the boundary layer profile imperceptible for $u'_\infty/U_\infty \gtrsim 5.3\,\%$.

A different way to introduce FST was examined by Thole & Bogard (1996). Crossflow jets were used to generate turbulence intensities up to 20 % in the freestream. The conclusions remained the same with the wake being suppressed while the logarithmic region was maintained. This demonstrated that it is not pivotal how the FST is generated.

In a study of canonical turbulent boundary layers without FST, Hutchins & Marusic (2007) introduced the use of spectrograms in boundary layer research. Pre-multiplied spectra at different wall-normal positions throughout the boundary layer are plotted in a contour map illustrating the energy distribution between different wavelengths in the

boundary layer from the wall up to the freestream. They covered a range of friction Reynolds numbers $1010 \leqslant Re_\tau \leqslant 7300$, with $Re_\tau = U_\tau \delta/\nu$ based on the friction velocity U_τ. Two peaks were found in the spectrograms: one coinciding with the location of the variance peak close to the wall, which was present through the full range of Re_τ examined, and an outer peak emerging with increasing Re_τ, distinctly visible at $Re_\tau = 7300$. Sharp *et al.* (2009) were the first to use an active grid to study the influence of FST on turbulent boundary layers. The active grid was modeled after the original design of Makita (1991). With the active grid, FST intensities up to 10.5 % were produced. This corresponded to a turbulence Reynolds number of $Re_\lambda = 550$, with $Re_\lambda = u'_\infty \lambda_\infty/\nu$ based on the Taylor microscale λ_∞. The examined boundary layers ($550 \leqslant Re_\theta \leqslant 2840$) showed a decrease of the wake strength with increasing FST, consistent with Blair (1983*a*). Analysing the pre-multiplied energy spectra showed the emergence of an outer spectral peak similar to the findings of Hutchins & Marusic (2007) at considerably lower Re_τ. This result was confirmed by Dogan *et al.* (2016) who also showed that the magnitude of the outer spectral peak scales with FST. In that work, turbulence intensities up to 13 % were generated with an active grid, and it was shown that the streamwise velocity fluctuations at the near-wall peak in the boundary layer correlate with freestream turbulence intensity. These observations in combination with the presented energy spectra demonstrate that the FST penetrates the boundary layer down to the wall. Despite the permeance of the FST, Dogan *et al.* (2017) used the same setup to demonstrate that the near-wall region is statistically similar to a canonical high-Re_τ turbulent boundary layer without FST.

Using the same setup, Esteban *et al.* (2017) confirmed the increase of skin friction with growing FST (Blair 1983*a*; Castro 1984). Oil-film interferometry was used to obtain the wall shear stress. It was also found that the relation between Reynolds number and skin friction is similar to canonical turbulent boundary layers without FST. Furthermore, it was demonstrated that oil-film interferometry and the multi-point composite fitting technique of Rodríguez-López, Bruce & Buxton (2015) were in good agreement in their estimates of U_τ for these TBL flows with FST above them.

In a subsequent study by Hearst *et al.* (2018), it was shown that for $8.2\,\% \leqslant u'_\infty/U_\infty \leqslant 12.3\,\%$, corresponding to $455 \leqslant Re_\lambda \leqslant 615$ and up to 65 % changes in the integral scale for a fixed u'_∞/U_∞, there was no influence of the length scale on the features of the boundary layer. It was proposed that this result differed from the older Hancock & Bradshaw (1989) result because of the increase in turbulence intensity, a different way of measuring the integral scale and measurements performed at positions more suitably distant from the grid. Through spectral analysis it was found that only the large scales penetrate the boundary layer, resulting in the outer spectral peak which would otherwise not be present in these flows, while the inner spectral peak remained unaffected. This result was included in the formulation of the law of the wall for such flows by Ganapathisubramani (2018). Finally, Hearst *et al.* (2018) developed a model that reproduced the spectrogram of the boundary layer based on the pre-multiplied energy spectrum of the freestream.

The majority of the aforementioned studies focussed on statistics and spectra at singular points in the TBL and did not investigate the streamwise development of the boundary layer. Earlier studies were in fact almost exclusively single plane measurements, and if the streamwise position was varied, this typically involved moving closer to the grid to obtain higher turbulence intensities. The spatial evolution of a canonical turbulent boundary layer without FST was studied experimentally by Vincenti *et al.* (2013) and Marusic *et al.* (2015). They showed that the magnitude of the near wall variance peak increases as the boundary layer evolves spatially. Furthermore, it was demonstrated that the emergence of an outer spectral peak with increasing Re_τ can also be observed in a spatially evolving turbulent boundary layer. There has also been some effort to simulate spatially developing

canonical turbulent boundary layers (Ferrante & Elghobashi 2004; Wu & Moin 2009; Eitel-Amor, Örlü & Schlatter 2014; Wu *et al.* 2017).

None of the aforementioned works investigated how a turbulent boundary layer evolves when subjected to FST which itself is also evolving. Raushan, Singh & Debnath (2018) examined a flow of this type, posing the inverse question: how does the spatial development of a boundary layer influence grid generated freestream turbulence. They used three different passive grids in an open water channel to create different levels of freestream turbulence. The focus in their analysis was on the development of inhomogeneous turbulence in the near-field region of the grids. You & Zaki (2019) compared a turbulent boundary layer subjected to FST (inflow $u'_\infty/U_\infty = 10\,\%$) to a canonical TBL in a direct numerical simulation (DNS). At $1900 \leqslant Re_\theta \leqslant 3000$, an increase of the skin-friction of up to 15 % was observed in the presence of FST, as well as the suppression of the wake region, confirming previous experimental results. This study also affirmed an increase in magnitude of the near-wall streamwise variance peak with the logarithmic region remaining robust. At their highest $Re_\theta = 3000$, they also observed the emergence of an outer peak in the pre-multiplied energy spectrogram. Wu, Wallace & Hickey (2019) examined the interfaces between freestream turbulence and laminar and turbulent boundary layers, as well as turbulent spots in a DNS, for $80 \leq Re_\theta \leq 3000$. Recently, Kozul *et al.* (2020) explored the evolution of a temporal turbulent boundary layer subjected to decaying FST. In their DNS study, they analysed the relative timescales of boundary layers and freestream turbulence to determine if and how much the boundary layer is affected. These were insightful works, but the achievable Reynolds numbers in DNS studies are still relatively low compared to what can be realized in a laboratory. So far the development of a turbulent boundary layer subjected to freestream turbulence has only been studied for low Reynolds numbers (Re_τ, Re_θ) and in single cases without comparison to other FST parameters. This study addresses this gap by examining the development of a turbulent boundary layer for $Re_\tau > 5000$ and $Re_\theta > 9000$ at three states of evolution for four levels of freestream turbulence. The influence of the evolving freestream turbulence on the mean velocity and variance profiles is examined, as well as the spectral distribution of energy in the developing boundary layer.

2. Experimental methods and procedure

The measurements were conducted in the water channel at the Norwegian University of Science and Technology. A schematic of the facility is provided in figure 1. The test section measures 11 m × 1.8 m × 1 m (length × width × height) with a maximum water depth of 0.8 m. It is a recirculating, free surface, water channel with a 4 : 1 contraction followed by an active grid upstream of the test section. A 10 mm thick acrylic plate measuring 1.8 m × 1.045 m was placed at the start of the test section, immediately downstream of the active grid, on the water surface to dampen surface waves directly caused by the water flowing through the bars of the active grid; the remaining ∼10 m of the water channel has a free surface. More details on the facility can be found in appendix A.

The active grid used in this study to generate the freestream turbulence is based on the design of Makita (1991). It is a biplanar grid with 28 rods – 10 horizontal and 18 vertical (figure 2). The rods are equipped with square-shaped wings that measure 100 mm on the diagonal and include two holes to reduce the motor loading, as well as to prevent 100 % blockage from occurring. Each rod can be controlled independently with a stepper motor. The mesh length of the grid, i.e. the spacing between each rod, is $M = 100$ mm. More information on the active grid design is provided in appendix B.

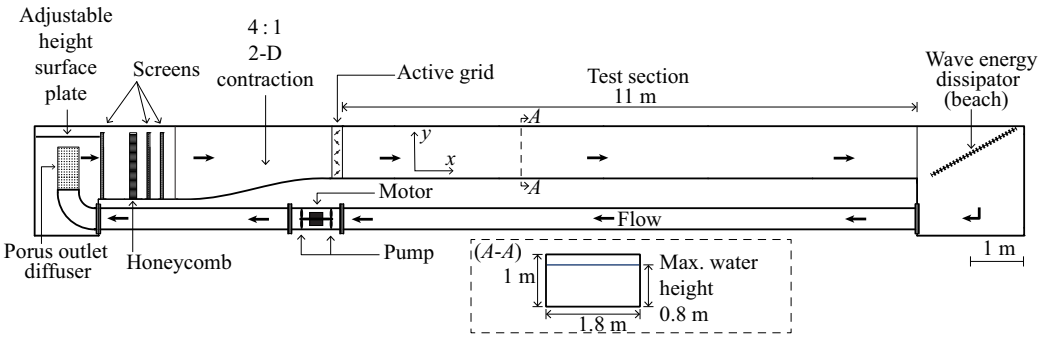

FIGURE 1. Schematic of the water channel facility in Strømningslaben at the Norwegian University of Science and Technology.

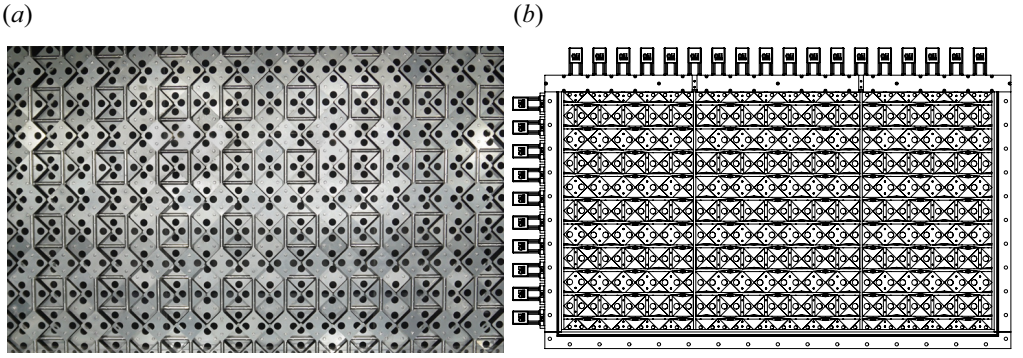

FIGURE 2. Biplanar active grid featuring square wings with holes. Viewed from the test section at full blockage and full schematic of the active grid.

The boundary layer was tripped by the bars of the active grid and then allowed to develop along the glass floor of the water channel. Wall-normal boundary layer scans were performed in the centre of the channel at three streamwise positions, $x/M = 35$, 55, and 95. The downstream positions relative to the grid were chosen to be greater than $30M$ to be in keeping with grid turbulence norms for homogeneity and isotropy of the freestream at all measurement positions (Ertunç *et al.* 2010; Isaza *et al.* 2014; Hearst & Lavoie 2015). Velocity measurements were performed with single-component laser doppler velocimetry (LDV). The laser has a wavelength of 514.5 μm. A 60 mm FiberFlow probe from Dantec Dynamics was used in backscatter mode in combination with a beam expander and a lens with a focal length of 500 mm. This results in an elliptical measuring volume with dimensions $\mathrm{d}x \times \mathrm{d}y \times \mathrm{d}z = 119\ \mu\mathrm{m} \times 119\ \mu\mathrm{m} \times 1590\ \mu\mathrm{m}$, which corresponds to 1.6–1.8 wall units y^+ in the wall-normal direction (depending on the case) and a fringe spacing of 3.33 μm. Wall unit normalization of the wall-normal position is $y^+ = yU_\tau/\nu$. The wall was found by manually positioning the measurement volume near the wall and then traversing downward in 0.1 mm steps until the data rate suddenly increased, indicating reflections by the glass floor. This gives an accuracy of ∼0.05 mm. The probe was then traversed upward from this position to the water surface applying a logarithmic spacing with a total of 24 measurement points for each scan. A method to correct for the true wall-normal position from the mean velocity profile, introduced by Rodríguez-López *et al.* (2015), was applied *a posteriori*.

The sampling rate of LDV is non-constant and varies with mean velocity – thus, in this study effectively with wall-normal distance. The mean sampling rate varied between 7 Hz directly at the wall and 155 Hz in the freestream. To guarantee convergence throughout the scans, every position was sampled for 10 min. This is between 630 and 1440 boundary layer turn-overs for a single measurement, depending on the test case. This might be low compared to some hot-wire studies, but it is still a substantial amount of data and sampling time with a single scan, pushing the realistic limits for what could be accomplished as a continuous run. Moreover, a 20 min convergence study in the freestream for the most turbulent case showed only a 0.4 % change in the variance compared to 10 min samples, which is smaller than the other measurement uncertainties. Time-series acquired with LDV also have a non-uniform time step distribution. To perform spectral analysis it is therefore required to resample the data. This is done with sample and hold reconstruction as proposed by Boyer & Searby (1986) and Adrian & Yao (1986). This method returns a uniformly spaced data series, which can then be used to compute spectra using a fast Fourier transform in the same manner as hot-wire data. The spectra are filtered with a bandwidth moving filter of 25 % to facilitate the identification of the underlying trends (Baars, Hutchins & Marusic 2016).

The friction velocity, U_τ, was estimated from the measured velocity profiles using the method introduced by Rodríguez-López *et al.* (2015), which was demonstrated to be effective in these flows by comparison to oil-film interferometry (Esteban *et al.* 2017). This method is essentially a multi-variable optimization applied to the composite boundary layer profile,

$$U^+ = \frac{1}{\kappa}\ln(y^+) + C^+ + \frac{2\Pi}{\kappa}\mathcal{W}\left(\frac{y^+}{Re_\tau}\right), \tag{2.1}$$

where κ is the von Kármán constant, Π is Coles' wake parameter (Coles 1956) and $\mathcal{W}$ is the wake function defined as per Chauhan, Monkewitz & Nagib (2009). Due to a limited number of points acquired in the log-region, a simple comparison of κ to $\kappa = 0.39 \pm 0.02$ as found by Marusic *et al.* (2013) across several facilities was made and found to be in good agreement; this is illustrated explicitly in the subsequent figures. The von Kármán constant is not a specific focus of the present investigation, but the interested reader can find more details on κ in the work by Hearst *et al.* (2018), who measured several points within the log-region for a TBL subjected to FST.

3. Freestream conditions

Four different inflow conditions were investigated in this work. They are presented in table 1 with their freestream statistics at the three measurement positions. The mean velocity in the freestream was kept constant at $U_\infty = 0.345 \pm 0.015$ m s^{-1} for all test cases. A slight increase in velocity was recorded for the downstream positions. This is expected due to the head loss and growing boundary layer in an open channel flow. Overall the differences in mean velocity are considered negligible here. The parameter of interest that was deliberately varied between cases is the turbulence intensity in the freestream u'_∞/U_∞. The reference case (REF) was created by orienting all the wings of the active grid in line with the flow, resulting in $2.5\,\% \leq u'_\infty/U_\infty \leq 3.2\,\%$ at the three measurement positions. It is worth noting that the background turbulence in water channel flows is typically on the order of 2 or 3 %, and thus this particular case quickly sees the flow return to the background state of the water channel. For comparison, the canonical turbulent boundary layer results presented by Laskari *et al.* (2018) were measured in a water channel with ∼3 % turbulence intensity in the freestream; thus our REF case is

Case	$\Omega \pm \omega$ (Hz)	x/M	U_∞ $(\mathrm{m\,s^{-1}})$	u'_∞/U_∞ (%)	$Re_{\lambda,\infty}$	$L_{u,\infty}$ (m)	u'_∞/v'_∞	Symbol
REF	—	35	0.33	3.2	59	0.20	1.1	●
		55	0.34	2.9	52	0.24	1.2	●
		95	0.35	2.5	45	0.32	1.2	●
A	1 ± 0.5 (2D)	35	0.34	5.5	176	0.30	1.2	■
		55	0.34	4.7	142	0.37	1.2	■
		95	0.35	3.8	103	0.50	1.2	■
B	1 ± 0.5	35	0.34	7.4	303	0.39	1.2	▲
		55	0.34	6.0	219	0.49	1.2	▲
		95	0.35	5.0	176	0.64	1.2	▲
C	0.1 ± 0.05	35	0.35	12.5	725	0.50	1.2	▶
		55	0.35	9.6	495	0.69	1.1	▶
		95	0.36	7.7	392	0.94	1.2	▶

TABLE 1. Freestream parameters of the examined cases at the different streamwise positions. Note that the colours fade with increasing downstream distance from the grid. These symbols are used in all figures and tables.

equivalent to their canonical case. For case A, the wings on the vertical rods remained static, while the horizontal rods were actuated. For the last two cases, B and C, all rods were actuated. The actuation mode for the cases A–C was always fully random. This means rotational velocity, acceleration and period were varied randomly over a set range (Hearst & Lavoie 2015). The parameter that was varied between cases was the mean rotational velocity Ω, i.e. $\Omega_A, = \Omega_B = 1$ Hz and $\Omega_C = 0.1$ Hz. All three cases were varied with a top-hat distribution $\Omega \pm \omega$ with the limits $\omega = 0.5\Omega$. The exact distributions used for each case are listed in table 1. The period and acceleration were always varied in the same range of 0.5–10 s and 10–100 $\mathrm{s^{-2}}$, respectively. The parameters were chosen based on the findings of previous active grid studies (Kang, Chester & Meneveau 2003; Larssen & Devenport 2011; Hearst & Lavoie 2015; Hearst *et al.* 2018) and slightly adapted to reflect the requirements of this study. The result is a wide range of turbulence intensities at the first measurement position $x/M = 35$, from 3.2 % for REF up to 12.5 % for case C. The turbulence intensity at the first position will be referred to as the initial turbulence intensity, $u'_0/U_0 = (u'_\infty/U_\infty)_{x/M=35}$.

The decay of the turbulence in the freestream was measured with a finer streamwise discretization. Measurements were taken at 15 positions between $x/M = 15$ and $x/M = 107$ at $y = 500$ mm. This wall-normal position was chosen as it was always outside the boundary layer while also being far away from the free surface. As the turbulence decays with increasing distance from the grid, the spread of turbulence intensity between the cases becomes smaller from $\Delta u'_\infty/U_\infty = 9.3$ % at $x/M = 35$ down to $\Delta u'_\infty/U_\infty = 5.2$ % at the last measurement position, $x/M = 95$. The decay of the turbulence with increasing distance from the grid can be described by a power law (Comte-Bellot & Corrsin 1966; Mohamed & Larue 1990; Lavoie, Djenidi & Antonia 2007; Isaza *et al.* 2014),

$$\frac{u'^2_\infty}{U^2_\infty} = A\left(\frac{x}{M} - \frac{x_0}{M}\right)^{-n}, \tag{3.1}$$

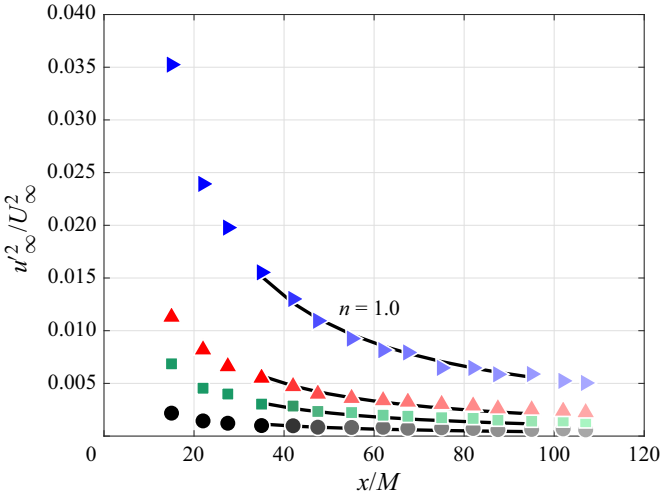

FIGURE 3. Decay of turbulence for case REF ●; A ■, green; B ▲, red; C ►, blue with fading colours indicating increasing streamwise distance from the grid.

where x_0 is a virtual origin, and A and n are the decay coefficient and exponent, respectively. Figure 3 shows the best fits to (3.1), resulting in $n \approx 1$ for all cases. Here, all three variables, A, x_0 and n were allowed to vary.

The Taylor microscale in the freestream λ_∞ was calculated as

$$\lambda^2_\infty = \frac{u'^2}{\langle(\partial u/\partial x)^2\rangle}, \tag{3.2}$$

assuming local isotropy and Taylor's frozen flow hypothesis to calculate $(\partial u/\partial x)^2$ from the time series data acquired at a singular streamwise position. A sixth-order central differencing scheme was used to determine the gradients as suggested by Hearst *et al.* (2012). This leads to turbulence Reynolds numbers Re_λ between 45 and 725. A decrease of Re_λ can be observed both for decreasing u'_0/U_0 and with streamwise evolution of the flow, as expected.

The integral length scale $L_{u,\infty}$ was calculated as proposed by Hancock & Bradshaw (1989) assuming isotropic turbulence,

$$U_\infty \frac{\mathrm{d}u'^2_\infty}{\mathrm{d}x} = \frac{-(u'^2_\infty)^{3/2}}{L_{u,\infty}}, \tag{3.3}$$

where x is the downstream distance from the grid, and the gradient $\mathrm{d}u'^2_\infty/\mathrm{d}x$ is calculated in physical space by taking the analytical derivative of (3.1). An increase in $L_{u,\infty}$ exists as the distance from the grid grows (table 1), which is expected. The integral scale was also computed by other means, e.g. integrating the auto-correlation to the first zero-crossing, but this approach was found to be less robust. Kozul *et al.* (2020, figure 7) demonstrated that while the finite value of the integral scale in flows like the present one is dependent on the method chosen for estimating it, the trends with evolution time (distance) and turbulence intensity are preserved.

The global anisotropy is also reported in table 1 as u'_∞/v'_∞. A separate two-component measurement campaign was performed to obtain these estimates. In general, the anisotropy

is between 1.1 and 1.2 and thus similar to what is typically reported in grid turbulence (Lavoie *et al.* 2007) and lower than the anistropy in some other studies of a similar nature (Sharp *et al.* 2009; Dogan *et al.* 2019). In most cases, the anistropy grows slightly with downstream distance, which is a result of the slight flow acceleration. Nonetheless, the positional variation in anistropy is always within $\pm 5\,\%$, which is approximately the uncertainty of this quantity. The isotropy itself was not a controlled parameter, and generally increasing the turbulence intensity with active grids comes with a loss of istropy (Hearst & Lavoie 2015). One should thus consider the present results in light of the anisotropy of the flow, which may also have an influence but was not rigorously controlled.

4. Evolution of the mean and variance profiles

Freestream turbulence has previously been shown to influence turbulent boundary layers all the way down to the wall (Castro 1984; Dogan *et al.* 2016; Hearst *et al.* 2018). While the majority of earlier studies focused on the influence of FST at a single point, in the present study we demonstrate that the evolution of the FST also plays a significant role. We begin with the mean statistics. In figure 4 the velocity and variance profiles for the four inflow conditions are displayed together for every measurement position, showing the differences between the cases at distinct downstream positions. It can be observed that the velocity profiles all collapse in the viscous sublayer, the buffer layer and the logarithmic region. In the viscous sublayer they follow the relation $U^+ = y^+$, with U^+ being a function of the streamwise velocity and the friction velocity $U^+ = U/U_\tau$. In the logarithmic region, all profiles agree with the law of the wall. This corresponds to the first three terms in (2.1); the plotted logarithmic region reference line has $\kappa = 0.39$ and $C^+ = 4.35$. The only significant deviation between cases and locations is in the region between the logarithmic layer and the freestream. In a canonical TBL this is the wake region, where large-scale mixing leads to a velocity defect (Coles 1956). When subjected to high enough freestream turbulence intensity, the wake region is known to be suppressed (Blair 1983*a*; Thole & Bogard 1996; Dogan *et al.* 2016). The freestream, being turbulent itself, leads to a suppression of the intermittent region that typically separates a canonical TBL from an approximately laminar freestream and replaces it with the inherent uniform intermittency of the FST, resulting in a suppressed wake in the boundary layer velocity profile (Dogan *et al.* 2016). The same can be observed here as presented in figure 4. Case REF with the lowest turbulence intensity of $u_0'/U_0 = 3.2\,\%$ shows traces of a wake region at $x/M = 35$ which grows with the development of the boundary layer; the wake is visible at $x/M = 55$ and 95. This evolution becomes even more apparent when looking at the velocity profiles of a single case at the three streamwise positions plotted together as presented in figure 5; we note that figure 5 does not contain different information from figure 4, but that plotting it in this way is also informative for comparison. DNS data of a fully developed canonical TBL without FST (Sillero, Jiménez & Moser 2013) at a Re_τ comparable to REF is included in figure 5 for reference. The mean velocity profile of REF and the DNS are in good agreement at our last measurement station. The variance profiles are roughly in good agreement, but the background turbulence in the freestream elevates the fluctuations in outer regions of the boundary layer for the experiment. At $x/M = 95$, the intermediate cases, A and B, also exhibit a wake region in the velocity profile (figures 4*c*, 5*b*) with turbulence intensities of $3.8\,\%$ and $5.0\,\%$, respectively, but this is still weaker than the REF case and the DNS. For case B, this trend starts to become visible at $x/M = 55$ and $u_\infty'/U_\infty = 4.7\,\%$. This is remarkably consistent with the limit of $u_\infty'/U_\infty = 5.3\,\%$ found by Blair (1983*a*). The present results demonstrate for the first time that even if the wake region is initially suppressed by the FST, it redevelops as the

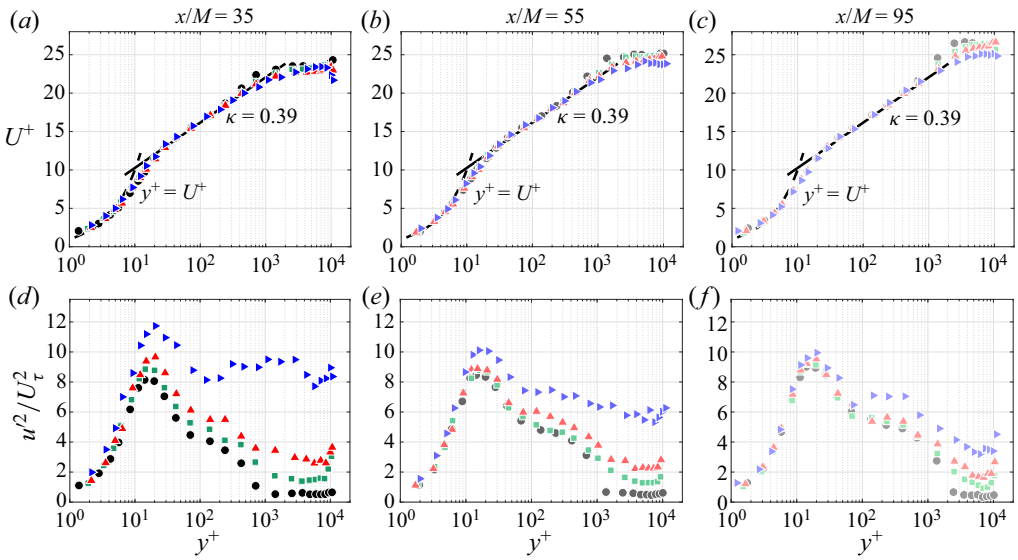

FIGURE 4. Mean velocity and variance profiles for cases REF ●; A ■, green; B ▲, red; C ▸, blue.

FST decays below a certain threshold. This is also supported by looking at Coles' wake parameter Π (Coles 1956). He predicted it to be 0.55 for a canonical turbulent boundary layer with no FST. Marusic *et al.* (2010) confirmed a similar value in their analysis using the model of Perry, Marusic & Jones (1998). Dogan *et al.* (2016) found $\Pi = 0.55$ in their no-FST case as well and showed that for FST with $7.4\,\% \leqslant u'_\infty/U_\infty \leqslant 12.7\,\%$ at $x/M = 43$, Coles' wake parameter drops to between -0.52 and -0.26. At $x/M = 35$, the present study shows values between -0.57 and -0.08 (table 2). For all cases, Π grows with the development of the TBL. The reference case reaches $\Pi = 0.37$, which approaches Coles' prediction. Both cases A and B eventually reach positive values for the wake parameter as the wake starts to become visible as one moves downstream. Case C does not show a visible recovery of the wake, as illustrated in figure 5(*c*). A visible difference remains compared to the canonical DNS of Sillero *et al.* (2013). The wake parameter for case C grows but remains negative and within the range of values for FST found by Dogan *et al.* (2016) throughout the three positions. u'_∞/U_∞ does not drop below 7.7 % within the studied distance from the grid for case C, suggesting it does not drop below the required threshold for wake recovery.

In the present study, we define the boundary layer thickness δ as the point where the velocity reaches 99 % of the freestream velocity, $\delta = \delta_{99}$. For all cases an increase of the boundary layer thickness is observed with the streamwise evolution of the TBL as documented in table 2. δ at $x/M = 35$ also scales with u'_∞/U_∞, likely due to enhanced mixing. It is also worth highlighting that $L_{u,\infty}$ grows with u'_∞/U_∞ at $x/M = 35$. From the first measurement station, the boundary layers with elevated FST (i.e. cases A, B and C) all grow more rapidly than the REF case.

Freestream turbulence is found to increase the friction velocity U_τ at a given point, in agreement with earlier works (Hancock & Bradshaw 1989; Blair 1983*a*; Castro 1984; Stefes & Fernholz 2004; Dogan *et al.* 2016; Esteban *et al.* 2017). This stems from the FST penetrating the boundary layer, increasing mixing and thus the momentum flux towards the wall. This increases the steepness of the velocity profile close to the wall (Dogan *et al.* 2016) and as a result also the skin friction (Stefes & Fernholz 2004).

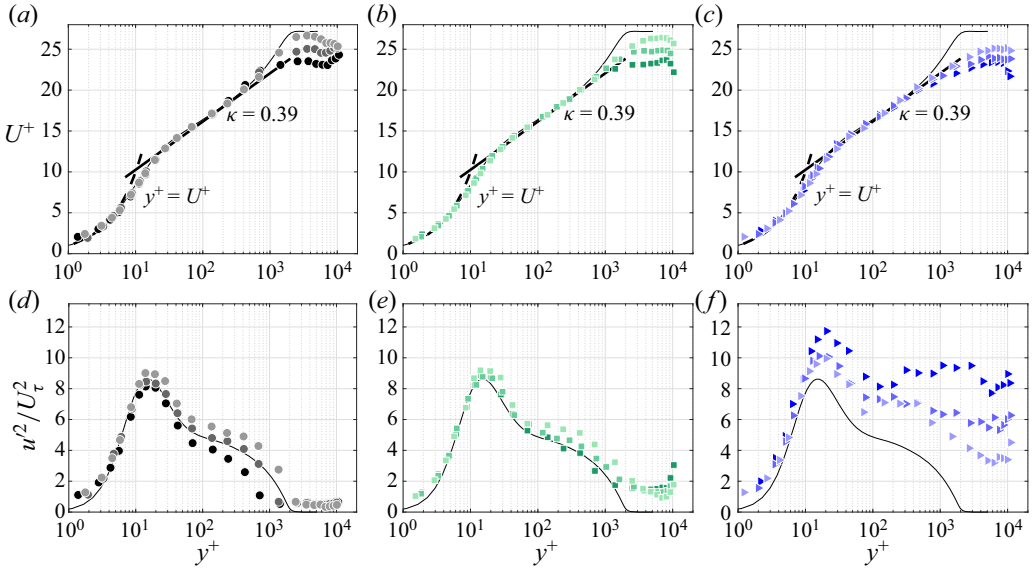

FIGURE 5. Development of mean velocity and variance profiles for cases REF ●; A ■, green and C ▶, blue with fading colours indicating increasing streamwise distance from the grid. DNS data of a fully developed canonical TBL at $Re_\tau \approx 1990$ by Sillero *et al.* (2013) plotted as a reference solid black line.

Case	u'_∞/U_∞ (%)	x/M	δ (mm)	δ^* (mm)	θ (mm)	H	U_τ (mm s^{-1})	Re_τ	Re_θ	Π	β	Symbol
	3.2	35	85	12	9	1.31	14.0	1210	3080	−0.08	0.73	●
REF	2.9	55	95	17	12	1.34	13.5	1310	4280	0.04	0.64	●
	2.5	95	138	25	19	1.34	13.1	1870	6860	0.37	0.58	●
	5.5	35	142	16	13	1.24	14.4	1990	4170	−0.19	1.34	■
A	4.7	55	170	20	16	1.26	13.8	2490	5860	0.04	1.13	■
	3.8	95	265	31	24	1.28	13.3	3700	8990	0.17	0.97	■
	7.4	35	152	15	12	1.23	14.8	2150	3840	−0.35	1.63	▲
B	6.0	55	220	21	17	1.23	14.0	3260	6230	−0.18	1.41	▲
	5.0	95	308	31	25	1.26	13.4	4340	9050	0.01	1.23	▲
	12.5	35	246	22	18	1.18	14.9	3610	6340	−0.57	3.09	▶
C	9.6	55	298	23	19	1.21	14.6	4590	7000	−0.35	2.22	▶
	7.7	95	343	29	24	1.22	14.2	5060	8820	−0.26	1.62	▶

TABLE 2. Boundary layer parameters of the test cases at the different streamwise positions.

A decrease in U_τ is observed as the boundary layer develops for each case. This agrees with the behaviour known for spatially evolving canonical turbulent boundary layers without FST (Anderson 2010; Vincenti *et al.* 2013; Marusic *et al.* 2015). Values for the friction Reynolds number Re_τ range from 1210 to 5060 and increase both with freestream turbulence intensity and streamwise development. The same is true for Re_θ, with values between 3080 and 9050. The empirical parameter β defined by Hancock & Bradshaw

(1989) is included in table 2. It follows the same trends as u'_∞/U_∞, showing that the influence of the FST is dominant in this flow. Greater discussion of this parameter can be found in appendix C.

The variance profiles at the first measurement positions in figure 4(*d*) resemble results from Dogan *et al.* (2016), Hearst *et al.* (2018) and You & Zaki (2019). They showed that the magnitude of the near-wall peak in the variance profiles correlates with the freestream turbulence intensity. The same can be observed in this study. The higher u'_∞/U_∞, the stronger the near-wall variance peak. FST penetrates the boundary layer and amplifies the fluctuations close to the wall. Moving downstream we can see that the magnitude of the near-wall peaks approach each other until they approximately collapse at $x/M = 95$ (figure 4*f*). Note that the four flows all still have distinct u'_∞/U_∞, $L_{u,\infty}$ and δ at $x/M = 95$. Thus, the present results demonstrate that if the boundary layer is allowed to evolve for a sufficient time, the correlation between the FST magnitude and the near-wall variance peak magnitude diminishes. This differs from earlier measurements performed at a single downstream position that could not observe this phenomenon. Taking a closer look at the development of the near-wall peak for the cases REF, A and C in figure 5, it becomes apparent that the approach to a common near-wall variance peak magnitude is due to different underlying trends in the four cases. For REF, the near-wall variance peak steadily increases with downstream position. This is in agreement with the results from Marusic *et al.* (2015) for spatially evolving canonical TBLs without FST. This trend is diminished but still present for case A; case B is similar to case A and is not plotted to reduce clutter. For case C, with the highest initial turbulence intensity, the trend reverses: instead of an increase, the near-wall variance peak decreases significantly with the development of the boundary layer. It can be concluded that the spatial development of the near-wall variance peak is strongly dependent on the initial level of turbulence intensity but approaches a common value downstream independently of the initial freestream state, at least for a given Re_τ. Hutchins & Marusic (2007) predicted this to be between 8.4 and 9.2 for the Re_τ examined here. The present measurements find a similar value of $u'^2/U_\tau^2 \approx 9.5$. This is slightly higher than what was found by Hutchins & Marusic (2007), which could be a result of the remaining freestream turbulence still present at the last measurement position, or differences in the noise floors of the measurement techniques used.

The displacement thickness $\delta^* = \int_0^\infty (1 - U(y)/U_\infty)\,\mathrm{d}y$ and momentum thickness $\theta = \int_0^\infty U(y)/U_\infty(1 - U(y)/U_\infty)\,\mathrm{d}y$ grow with streamwise evolution for all cases. The ratio between the two is the shape factor $H = \delta^*/\theta$, which is an indicator of the fullness of the boundary layer profile. Small deviations for the dimensional quantities δ^* and θ can be explained by differences in the mean velocity and uncertainty in the measurements. The trend is still captured accurately. Consequently, in the nondimensional H, the small deviations vanish. This study shows that freestream turbulence reduces the shape factor as the boundary layer profile becomes fuller – i.e. the velocity rises more steeply close to the wall, while farther away from the wall the velocity profile becomes flatter. This is in good agreement with previous studies (Hancock & Bradshaw 1983; Castro 1984; Stefes & Fernholz 2004; Dogan *et al.* 2016; Hearst *et al.* 2018). As presented in figure 6 and table 2, the higher the initial turbulence intensity, the lower the shape factor. For a canonical turbulent boundary layer, Monkewitz, Chauhan & Nagib (2008) found that the shape factor decreases with increasing Re_θ. This is confirmed for each downstream position in this study as depicted in figure 6; the data from Dogan *et al.* (2016) have also been plotted showing the same trend.

The aforementioned trend pertains to a single position. However, the question of how the evolution of H is impacted by the FST is still open. The data of Hancock & Bradshaw (1983) suggest a decrease of the shape factor as one moves downstream; this data is also

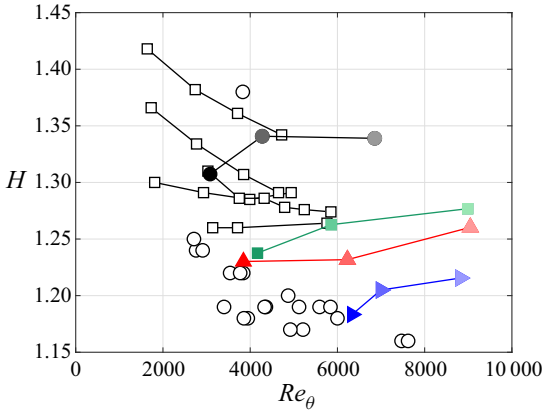

FIGURE 6. Development of the shape factor H for cases REF ●; A ■, green; B ▲, red; C ▸, blue with fading colours indicating increasing streamwise distance from the grid. The data of Hancock & Bradshaw (1983) □ and Dogan *et al.* (2016) ○ are also included for reference. Lines connecting points indicate that they were acquired from the same set-up but at different streamwise positions. All Dogan *et al.* (2016) measurements were conducted at the same location but with different freestream conditions.

included in figure 6. It has to be kept in mind that their measurements were for relatively low turbulence intensities, and some of them were very close to the grid. We show that when the turbulence intensity in the freestream is increased further and the measurements are taken past $x/M = 30$, this trend reverses. The shape factor is reduced significantly at the first measurement position, and as the freestream turbulence decreases it recovers towards its natural value. This value can be obtained by looking at the shape factor of canonical zero pressure gradient turbulent boundary layers for a wide range of $Re_{\delta^*} = U_\infty \delta^*/\nu$ as presented by Chauhan *et al.* (2009). For Re_{δ^*} between 4000 and 10 000, as found in the present study, a shape factor between 1.35 and 1.41 would be expected without the presence of freestream turbulence (Chauhan *et al.* 2009). While the shape factors of Hancock & Bradshaw (1983) drop away from the canonical values with increasing distance from the grid (Chauhan *et al.* 2009), the data presented herein trend toward the predicted values. The boundary layer appears to forget it started with different conditions as the influence of these conditions diminishes farther downstream.

The continuous streamwise development of the boundary layer results in an increase of Re_τ for all cases. At the same time Re_τ scales with the level of freestream turbulence which decays with streamwise evolution of the flow. It is therefore interesting to compare boundary layers with similar Re_τ but different paths to get there. This is done in figure 7 with the reference case at $x/M = 95$ with $u'_\infty/U_\infty = 2.5\,\%$ and $Re_\tau = 1870$ and case A at $x/M = 35$ with $u'_\infty/U_\infty = 5.5\,\%$ and $Re_\tau = 1990$ (figure 7*a*,*c*), as well as with case A at $x/M = 95$ with $u'_\infty/U_\infty = 3.8\,\%$ and $Re_\tau = 3700$ and case C at $x/M = 35$ with $u'_\infty/U_\infty = 12.5\,\%$ and $Re_\tau = 3610$ (figure 7*b*,*d*). For the first comparison (figure 7*a*,*c*) with a moderate difference in freestream turbulence intensity, the deviations in the variance profiles are small. Nevertheless, a distinction in the outer region is visible in the velocity profile. Whereas for case A at $x/M = 35$ the wake is still suppressed, for the most part, the reference case at $x/M = 95$ displays a pronounced wake region. This is particularly interesting given these two cases have essentially the same freestream integral scale, $L_{u,\infty} \approx 310$ mm and $2.1 \leq L_{u,\infty}/\delta \leq 2.3$, suggesting that this parameter is not what is driving the difference in the outer region. When comparing cases with a bigger difference

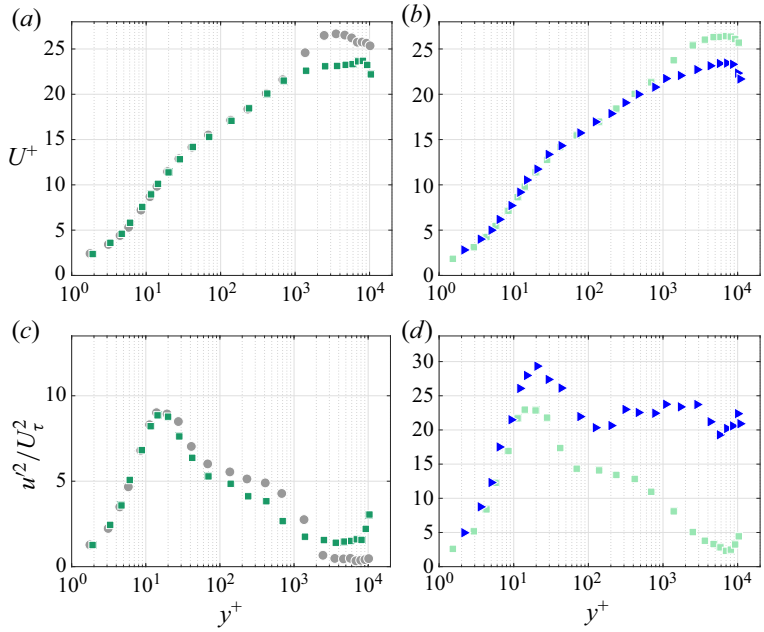

FIGURE 7. Comparison of TBL profiles with similar Re_τ: (*a*,*c*) case REF at $x/M = 95$ •, grey and case A at $x/M = 35$ ■, green; (*b*,*d*) case A at $x/M = 95$ ■, light green and case C at $x/M = 35$ ▸, blue.

in freestream turbulence (figure 7*b*,*d*), the differences become even more distinct. Once again the velocity profiles are collapsed in the viscous sublayer, the buffer layer and the logarithmic region. Farther away from the wall the profiles diverge. For case C the wake region is fully suppressed at this point, whereas case A at $x/M = 95$ shows the reemergence of a wake. In the variance profiles the considerable difference in u'_∞/U_∞ is visible. Moving closer to the wall it becomes evident that the turbulence intensity in the freestream also influences the boundary layer close to the wall. The near-wall variance peak is significantly more pronounced for the case with the higher freestream turbulence intensity. These particular cases have the same $L_{u,\infty}$ and $1.9 \leq L_{u,\infty}/\delta \leq 2.0$, again suggesting the above differences are not a result of a difference in the size of the large scales in the freestream. The same general trends were also observed at $Re_\tau \approx 4500$. One can thus conclude that Re_τ alone is not sufficient to describe the profile of a turbulent boundary layer subjected to FST, but rather u'_∞/U_∞ and the evolution distance must also be considered at a minimum.

5. Evolution of the spectral distribution of energy

Further insight into the processes governing the evolution of a TBL subjected to FST can be gained by looking at the spectral distribution of energy at different streamwise positions. For this, the pre-multiplied spectra, $\phi^+ = k_x\phi_u/U_\tau^2$, at every wall-normal position are plotted together in a contour map illustrating regions and wavelengths, $\zeta^+ = 2\pi U_\tau/k_x\nu$, with high and low energy. This is based on the streamwise energy spectra ϕ_u in normalized wavenumber space k_x. Computing spectra from the LDV measurements is not as straightforward as it is from hot-wires, which is the more common measurement technique in TBLs. As stated in § 2, we have used the sample

and hold technique to compute the spectra and applied a bandwidth moving filter. The spectra are also computed over less boundary layer turn-overs than is typical in hot-wire measurements, despite the long sample times used herein. As such, we provide the present spectra as qualitative relative comparisons in which we have confidence, rather than exact quantitative comparisons to the hot-wire-acquired spectra in the literature.

Hutchins & Marusic (2007) showed that in a canonical turbulent boundary layer there is a fixed peak close to the wall at $y^+ \approx 15$ and $\zeta^+ \approx 1000$. They further showed that for high $Re_\tau = 7300$, an outer spectral peak emerges. The evolution of the spectrograms in a spatially developing TBL for different initial freestream turbulence intensities is presented in figure 8. The first observation is that in agreement with Dogan *et al.* (2016), Hearst *et al.* (2018) and Ganapathisubramani (2018), the location of the near-wall spectral peak is independent of the level of freestream turbulence and coincides with the location found by Hutchins & Marusic (2007). It seems that the small scales close to the wall are not affected by the freestream turbulence. This is displayed explicitly in figure 9, where the larger scales deviate visibly for the higher FST cases above $u'_\infty/U_\infty \approx 6\,\%$, in agreement with Hearst *et al.* (2018).

Looking at the first measurement position, $x/M = 35$, in figure 8 confirms the findings of Sharp *et al.* (2009), Dogan *et al.* (2016) and Hearst *et al.* (2018) that when subjected to strong enough FST an outer spectral peak forms at considerably lower Reynolds numbers than in canonical TBLs – here at $Re_\tau = 3610$ for case C. For the lowest Re_τ of 1210, corresponding to the reference case at $x/M = 35$, no outer peak exists, and the spectrogram resembles the shape found by Hutchins & Marusic (2007) for $Re_\tau = 1010$. Cases B and C at $x/M = 35$ demonstrate a timid emergence of an outer spectral peak. The novel element of the present study is the streamwise development of these features. For cases REF, A and B, with initial turbulence intensities between 3.2 % and 7.4 %, the outer spectral peak grows in magnitude and moves away from the wall as the boundary layer develops. Of these three cases, case B with the highest initial turbulence intensity u'_0/U_0, shows the strongest outer spectral peak. This agrees with the trend for increasing Re_τ detected by Hutchins & Marusic (2007) in a canonical TBL.

Up until the present study there has been no reason not to expect a growth of the outer spectral peak with increasing Re_τ for higher freestream turbulence intensities as well. Instead, case C with the highest initial turbulence intensity of $u'_0/U_0 = 12.5\,\%$, presents different behaviour. The outer spectral peak is pronounced at $x/M = 35$. In contrast to the expected continuous growth of the outer spectral peak in canonical TBLs, here it gradually decreases as the boundary layer develops and the freestream turbulence decays. Thus, if one did not know the measured values of Re_τ, the spectrogram from earlier in the spatial evolution of case C gives the impression it is at a higher Re_τ than those from farther downstream. In contrast to the lower FST cases, the decay of the freestream turbulence more significantly influences the spectrogram than the growth of the TBL. This fading of the outer spectral peak is visible throughout the three measurement positions for case C. This behavior becomes more evident when looking at the net change $\Delta^+ = (\phi^+ - \phi_0^+)/\phi^+_{0,max}$ in spectrograms, where ϕ_0^+ is the spectrogram at $x/M = 35$. This is displayed in figure 10 for the reference case compared to case C with the highest freestream turbulence intensity. The reference case (figure 10*a*,*b*) shows the slow emergence of an outer peak with a positive net change Δ^+ for $\zeta^+ \approx 10^4$ most distinctly in the outer regions of the boundary layer at $y^+ \approx 10^3$. The opposite is observed for case C in figure 10(*c*,*d*), with a negative net change where the outer spectral peak was initially most pronounced at $10^3 \lesssim y^+ \lesssim 10^4$ and $10^4 \lesssim \zeta^+ \lesssim 10^5$. The location of the outer spectral peak in outer scaling, i.e. y/δ and ζ/δ, does not coincide with the location for canonical TBLs identified by Hutchins & Marusic (2007). This is to be expected for a TBL subjected to FST (Dogan

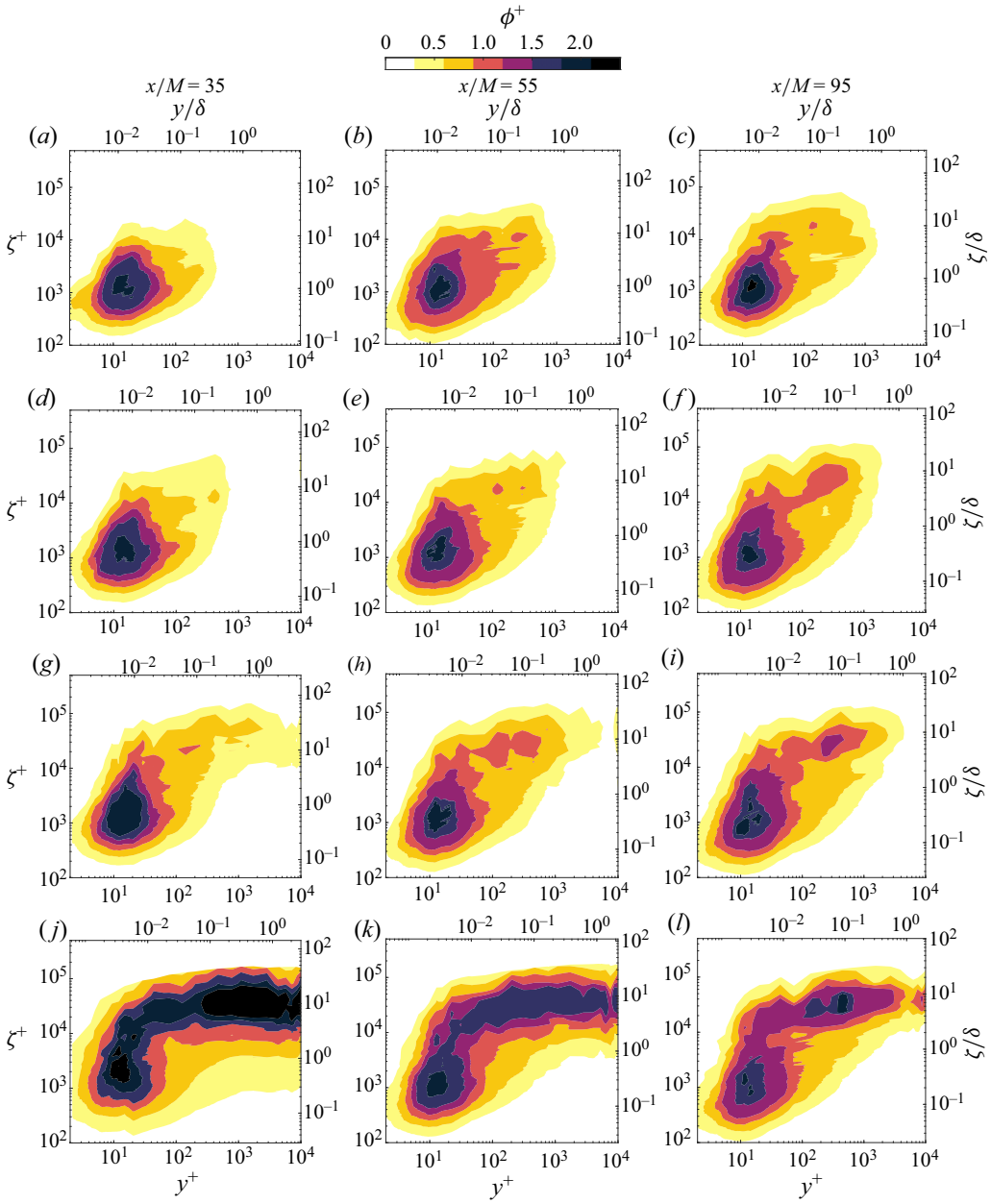

FIGURE 8. Spectrograms for cases REF (*a–c*), A (*d–f*), B (*g–i*) and C (*j–l*) at the three streamwise positions with increasing level of freestream turbulence from top to bottom.

et al. 2016; Hearst *et al.* 2018). The reason for this is that the peak is superimposed onto the outer boundary layer by the freestream turbulence. In fact, the peak is situated much higher for the FST cases and moves only once the boundary layer starts to redistribute the energy. This is documented in great detail for numerous cases in Hearst *et al.* (2018). As the outer peak evolves in this study, it approaches $\zeta_x/\delta \approx 10$ and $y/\delta \approx 0.4$ as found by Hearst *et al.* (2018).

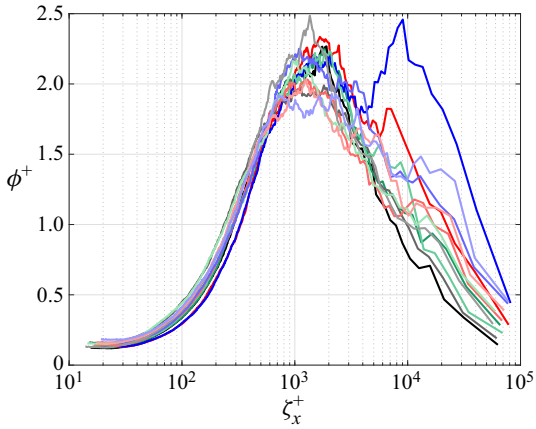

FIGURE 9. Normalized pre-multiplied velocity spectra at the near-wall spectral peak for cases REF solid black line, A solid green line, B solid red line, C solid blue with fading colours indicating increasing streamwise distance from the grid.

It is also interesting to compare case B at $x/M = 35$ (figure 8*g*) and case C at $x/M = 95$ (figure 8*l*), which have approximately the same freestream turbulence intensity $7.4\,\% \leq u'_\infty/U_\infty \leq 7.7\,\%$ and integral scale relative to the boundary layer thickness $2.6 \leq L_{u,\infty}/\delta \leq 2.7$. Their spectrograms look very different, demonstrating the importance of the evolution on the energy distribution within the boundary layer. Furthermore, when comparing cases with similar Re_τ, e.g. case A at $x/M = 95$ (figure 8*f*) and case C at $x/M = 35$ (figure 8*j*), the difference is even more apparent. Figure 8(*f*) shows a hint of an outer spectral peak, while figure 8(*j*) represents the most prominent occurrence of an outer peak of all the measurements. This underlines the fact that Re_τ must be considered alongside u'_∞/U_∞ and the evolution distance when studying TBLs subjected to FST.

6. Global trends

The way this experiment was constituted, there were two main factors modulating the boundary layer contrarily to each other. On the one hand, the TBL was evolving spatially, growing and becoming more developed. On the other hand, the FST, which artificially matured the state of evolution of the boundary layer, decayed with increasing distance x from its origin, the active grid. The streamwise evolution of a boundary layer may be expressed through $Re_x = U_\infty x/\nu$. Figure 11 summarizes how the natural growth of the boundary layer and the decay of the freestream turbulence interact, and which prevails under what conditions. The implications for different characteristics of a TBL are examined as the boundary layers evolve spatially.

The boundary layer at a single position thickens with increasing freestream turbulence intensity. As the flow evolves, the turbulence in the freestream decays and the integral scale grows. At the same time the boundary layer develops. Overall this leads to a growth of the boundary layer thickness for all levels of freestream turbulence. Figure 11(*b*) shows a relatively uniform stacking of the boundary layer thickness with u'_∞/U_∞ for low Re_x. As the flow develops, the higher FST intensity cases A, B and C have similar values of δ, while δ for REF is demonstrably smaller. The influence of u'_∞/U_∞ on δ decreases as the flow evolves, but a distinct difference remains between low and moderate to high FST intensity.

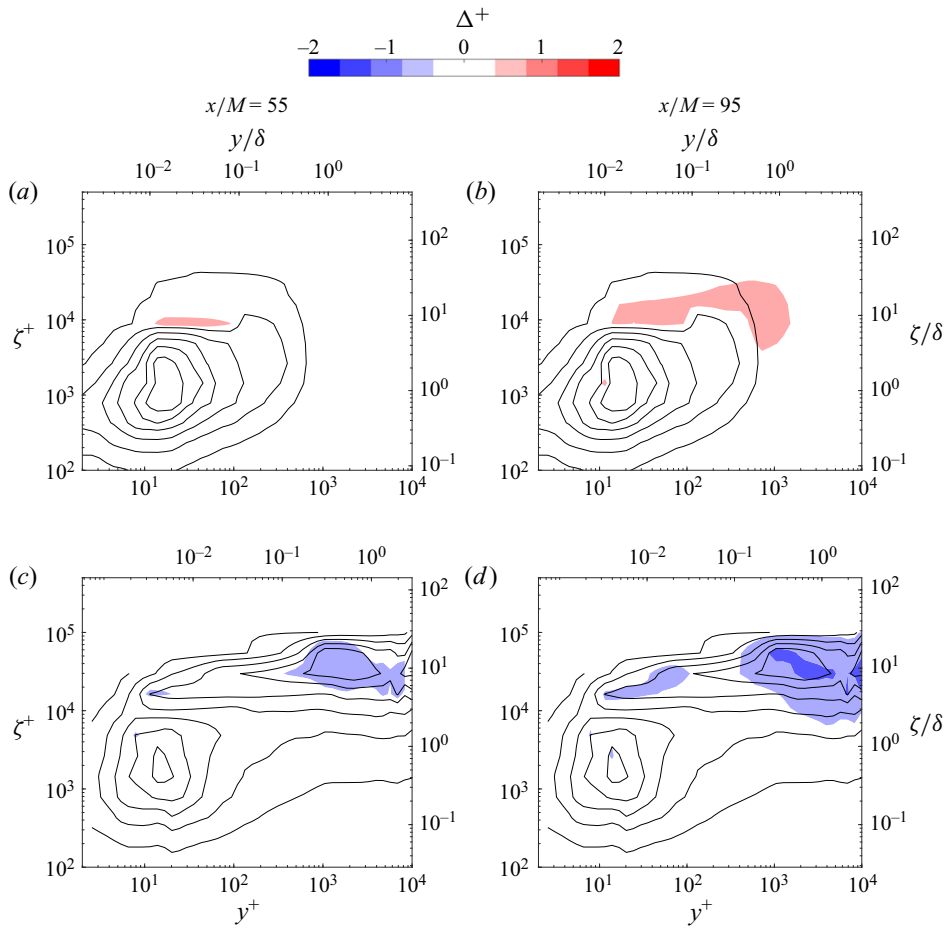

FIGURE 10. Net change $\Delta^+ = (\phi^+ - \phi_0^+)/\phi_{0,max}^+$ in spectrograms at $x/M = 55$ and $x/M = 95$ for cases REF (*a*,*b*) and C (*c*,*d*) with respect to initial spectrogram at $x/M = 35$. The contour lines of the initial spectrogram are imprinted as a reference.

For a sufficiently developed canonical turbulent boundary layer, the shape factor H decreases with increasing Re_x (Vincenti *et al.* 2013; Marusic *et al.* 2015). This decrease can also be achieved by introducing FST in the flow. The result is, contrarily to a canonical TBL, H grows with increasing Re_x as the boundary layer develops beneath decaying FST. Presumably there is a turning point when H will start decreasing again. Throughout the examined range, the shape factor remains distinguished by u'_∞/U_∞ (figure 11*c*). The influence of the initial difference in freestream turbulence is transported through the examined range of Re_x. Similar behaviour can be observed for the wake region of the TBL. This is quantified through Coles' wake parameter Π, which is known to trend towards a fixed value for canonical conditions with high Reynolds numbers and sufficient development length (Marusic *et al.* 2010). Freestream turbulence suppresses the intermittency in the wake region, thus leading to the suppression of the typical flow profile seen in the wake region and a significantly depleted wake parameter (Dogan *et al.* 2016). The stronger the freestream turbulence intensity, the lower Π becomes. The wake is predominantly influenced by the FST, and as it decays, the wake

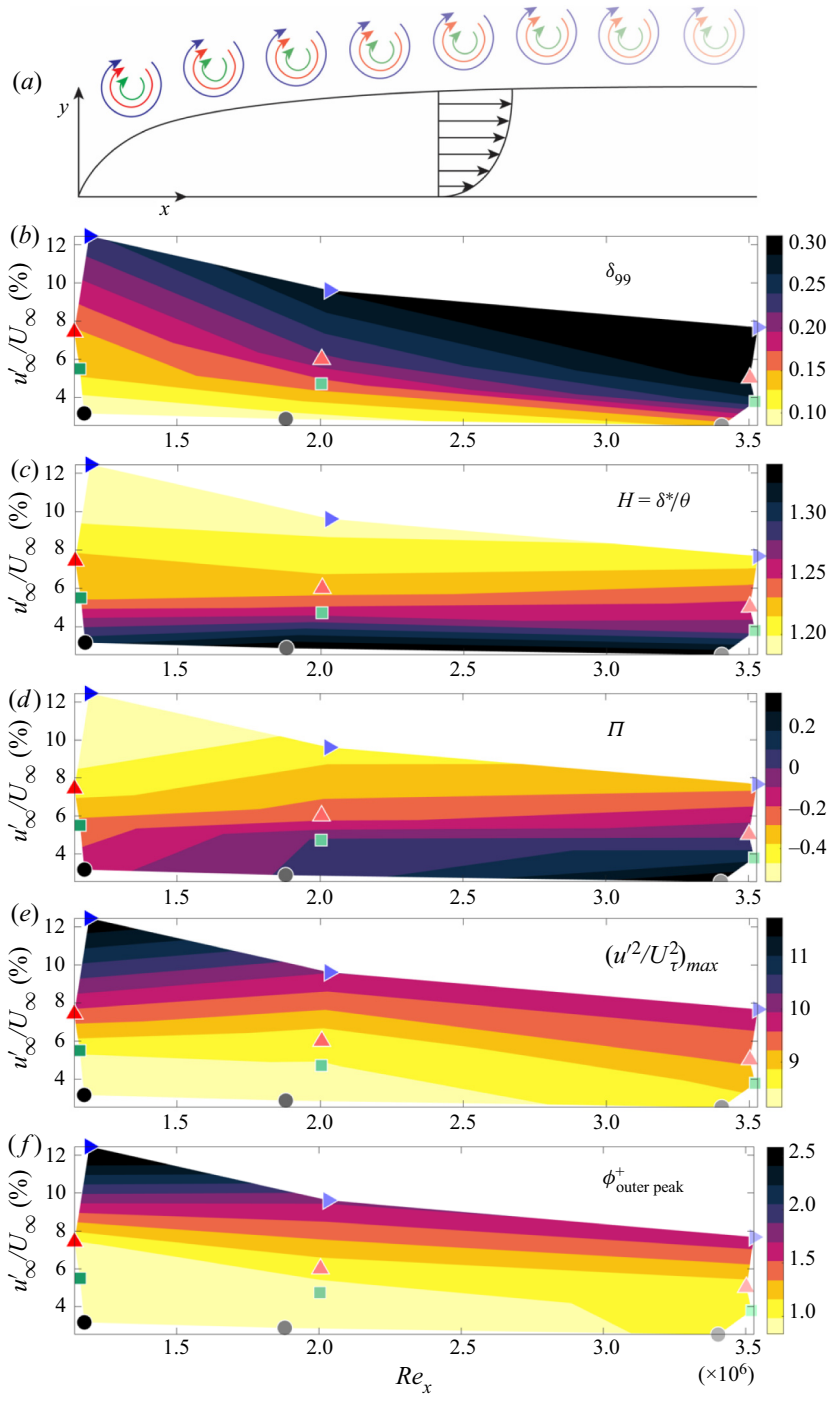

FIGURE 11. Trends for an evolving turbulent boundary layer subjected to different levels of freestream turbulence. Case REF ●; A ■, green; B ▲, red; C ►, blue with fading colours indicating increasing streamwise distance from the grid.

becomes more pronounced. The overall change of Π with spatial evolution is more substantial than the change to H. For the lower turbulence intensities, Π approaches the analytical value of 0.55 (Coles 1956), and a visible wake region re-emerges within the investigated spatial development range (figure 5). The change in shape of the boundary layer indicates that the FST penetrates the boundary layer and has an influence on its evolution.

How deep and how significant that influence is becomes evident when looking at the modulation of the near-wall variance peak at $y^+ \approx 15$. The magnitude is strongly dependent on the level of turbulence in the freestream, with a higher turbulence intensity correlating with a higher peak in the variance. For canonical TBLs, the near-wall peak increases with the evolution of the boundary layer until the profiles become self-similar. This behaviour can be observed for lower initial freestream turbulence up to $u_0'/U_0 = 5.5\,\%$. For the highest freestream turbulence intensity, the decay of the turbulence proves to be dominant, as the near-wall variance peak decreases in magnitude as the flow evolves.

For high enough Re_τ, TBLs develop an outer peak in the spectral energy distribution (Hutchins & Marusic 2007). This state can also be reached by subjecting the boundary layer to high-intensity freestream turbulence (Dogan *et al.* 2016; Hearst *et al.* 2018). For canonical TBLs, this peak develops as the boundary layer grows spatially and Re_τ increases. This is observed for the lower freestream turbulence cases $3.2\,\% \leqslant u_0'/U_0 \leqslant 7.4\,\%$ here. Initially there is no outer peak visible in the spectrograms, but as the boundary layer develops, the magnitude of the outer peak gradually increases. This evolution looks very different for the highest level of freestream turbulence. A strong peak exists at the first measurement position, then proceeds to decrease with streamwise evolution of the flow. For this case, the decay of the FST appears to drive the phenomenology. The drop in outer peak magnitude is significantly higher than the observed increase for the lower FST cases (figure 11*f*). We thus again arrive at the conclusion that these flows must be parameterized by Re_τ, u_∞'/U_∞ and the streamwise development of the flow.

7. Conclusions

The evolution of a turbulent boundary layer subjected to different freestream turbulent flows was studied experimentally for $1210 \leqslant Re_\tau \leqslant 5060$. The freestream turbulence was generated with an active grid in a water channel. Boundary layer profiles were taken at three streamwise positions for four inflow turbulence intensities $3.2\,\% \leqslant u_0'/U_0 \leqslant 12.5\,\%$. It is important to appreciate that the conclusions presented herein are derived from the results of the present measurement campaign and the investigated turbulence intensities, integral scales and anisotropy. This is the first in-depth analysis of how freestream turbulence influences the characteristics of a spatially evolving turbulent boundary layer at Reynolds numbers of this magnitude. In particular, the interaction of decaying freestream turbulence with a developing turbulent boundary layer was examined. The main findings of this study are:

(i) The development of the boundary layer mean velocity profile changes in the presence of freestream turbulence. Instead of a decrease in shape factor, as observed in canonical turbulent boundary layers (Monkewitz *et al.* 2008), H increases as the freestream turbulence decays. The suppression of the wake region for high freestream turbulence intensities observed in accordance with Blair (1983*a*), Thole & Bogard (1996) and Dogan *et al.* (2016) can be reversed as the flow

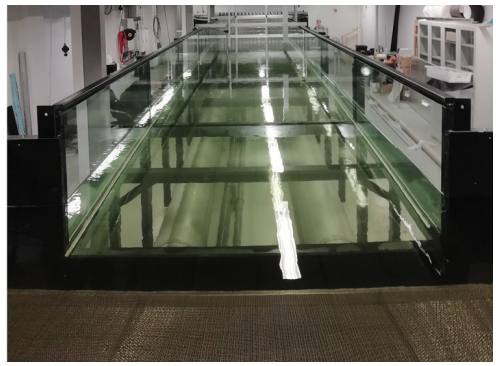

FIGURE 12. Water channel facility viewed from the end tank.

evolves downstream. It was shown that as the freestream turbulence decays below $u'_\infty \approx 5\,\%$, the wake region is recovered.

(ii) The influence of the freestream turbulence on the magnitude of the near-wall variance peak decreases as the freestream turbulence decays in the spatially developing flow. For high-intensity FST cases, a decrease in near-wall variance peak magnitude was observed contrarily to lower freestream turbulence levels where an increase was noted with the development of the boundary layer. The latter is similar to canonical turbulent boundary layers without freestream turbulence.

(iii) Spectral analysis showed that an outer peak in the spectrograms can be formed in two ways, and that this is pivotal for the evolution of the spectrograms. For $u'_0/U_0 =$ 3.2-7.4 %, it emerges gradually as the boundary layer evolves as observed for canonical boundary layers by Hutchins & Marusic (2007) and Marusic *et al.* (2015). The mechanisms at the wall that naturally generate this peak are dominant here. However, an outer spectral peak can also be imprinted by high intensity freestream turbulence (Sharp *et al.* 2009; Dogan *et al.* 2016; Hearst *et al.* 2018). For the latter, it was demonstrated that as the flow develops spatially and the freestream turbulence decays, the outer spectral peak becomes weaker, and hence the flow does not remember that it had an outer peak earlier in its evolution. The information available in the literature does not suggest that the boundary layer would effectively regress to a less mature state once the freestream turbulence decayed, and evidence of this is presented herein for the first time.

Generally, it was found that for turbulent boundary layers subjected to freestream turbulence, the previous perspective that one could parameterize the flow with just a few parameters, i.e. Re_τ or Re_θ, u'_∞/U_∞ and $L_{u,\infty}$, is incorrect. For example, flows with similar Re_τ, u'_∞/U_∞ or $L_{u,\infty}/\delta$ can have significantly different boundary layer characteristics depending on the evolution of the freestream turbulence and boundary layer. Thus, the relative evolution of the freestream turbulence and the boundary layer must also be considered.

Funding

This work was funded by the Research Council of Norway project no. 288046 (WallMix).

Declaration of interests

The authors report no conflict of interest.

Appendix A. Water channel facility

The water channel is a recirculating facility with a capacity of 65 tons of water. A picture of the facility as viewed from the end tank is shown in figure 12 and a schematic was provided in figure 1. It is driven by two Siemens 1AV2186B 3-phase squirrel-cage motors each connected to two counter-rotating propellers. Each motor-pump assembly forms a part of the return pipe system that runs the length of the water channel underneath the test section. The motors are controlled via two ABB ACS550 variable frequency drives. The two return pipes supply water to the channel through a 90° bend each into a polyethylene settling chamber. The end section of the outlet is constructed from porous sheet metal to provide a diffuse source of water. A flat circular plate is also secured within the porous section to minimize the size of the water jet from the outlet. A large acrylic surface plate with adjustable height is placed above the outlet to dampen the surface waves caused by the water flowing out of the exits. After the outlet, the water flows through a porous plate, followed by a honeycomb and then a pair of stainless steel screens with progressively smaller mesh size for flow conditioning. A 4 : 1 fibreglass contraction connects the settling chamber and the test section. Between the contraction and the test section, there is a slot measuring 200 mm wide intended for the installation of turbulence generating grids. This section consists of permanently mounted acrylic frames with interchangeable inner skins, allowing for an active grid, passive grid or clean flow. The test section measures 11 m $\times$ 1.8 m $\times$ 1 m internally and is constructed from float glass panes supported by stainless steel frames. The maximum water level is 0.8 m. The clear glass construction provides optical access for laser diagnostic measurements and other optically-based measurement techniques. The water exits the test section into a stainless steel end tank, where it recirculates back to the return pipes. A stainless steel frame with wire meshes on both sides is installed in the end tank at an angle. This device acts as a wave energy dissipator to prevent large reflected waves from the end tank. The height and angle of the dissipator are adjustable. The water is kept free from debris and algae through a filter system consisting of a pump, a cyclone filter, a particle filter and a UV-lamp. There is no active temperature control for the water channel; however, once the water reaches an equilibrium with the room temperature, the daily variation in water temperature is less than 0.5 °C, which is monitored with a thermocouple.

The freestream flow velocity is measured through a Höntzsch ZS25 vane wheel flow sensor with an accuracy of 0.01 m s^{-1}. The flow sensor has an analogue current output, which is converted to an analogue voltage output and connected to a NI-9125 C series voltage input module. A T-type thermocouple is placed in the test section to measure the water temperature. It is connected to a NI-9210 C series temperature input module. Both modules are plugged into a NI cDAQ-8178 CompactDAQ chassis, which is in turn connected to a data acquisition computer.

Appendix B. Active grid

An active grid is an instrument for controlling freestream turbulence that is gaining popularity. While active grids are becoming more common, comprehensive documentation of them is still sparse. As such, this section offers a detailed description that can be potentially useful for others in the future.

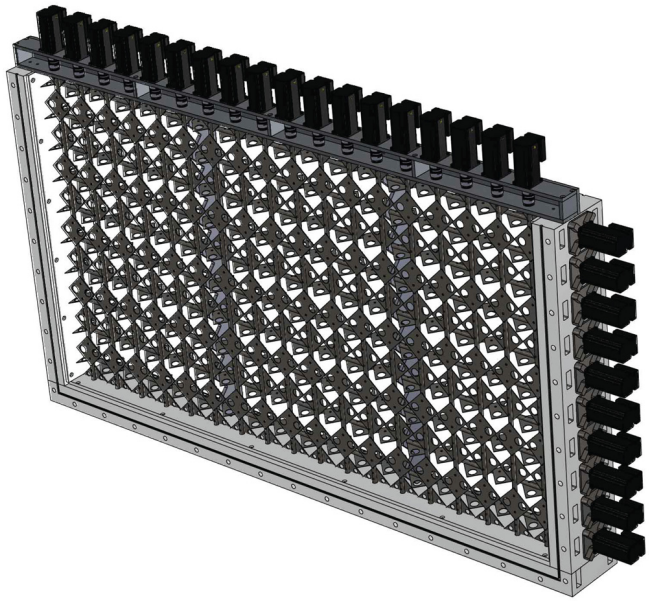

FIGURE 13. Three-dimensional view of the active grid at the water channel facility at the Norwegian University of Science and Technology.

The active grid used in the present study was designed in-house, and a three-dimensional drawing of the design is shown in figure 13. It consists of 28 independently controlled stainless steel rods arranged in a biplanar square mesh, with 10 horizontal rods and 18 vertical rods. The mesh length M defined by the centre to centre distance between the rods is 100 mm, and the rods measure 12 mm in diameter. The grid stretches across the entire cross-sectional area of the test section. Stainless steel 1 mm thick square-shaped wings are attached to the rods in a space-filling manner. The sides of the wings measure 70.71 mm, such that the diagonal measures 100 mm, which matches the mesh length of the grid. Each wing has two 24 mm-diameter holes cut out of it in order to reduce the loading on the motors during actuation sequences, as well as to make sure a 100 % blockage scenario is impossible. The maximum blockage ratio achievable by the active grid is 81.9 %, and the minimum blockage ratio is 22.6 %. The rods are CNC-machined to have a 1 mm deep flat for wing mounting, such that the wings sit flush with the rod. As the maximum water level is 0.8 m, only the bottom eight horizontal rods are submerged at the maximum capacity; the top two rods are always in the air and are meant for possible future expansion of the facility. Figure 2 shows the middle section of the active grid at maximum blockage. The horizontal rods are supported at four locations by low-friction plastic bushings, two at the ends and two within the grid body, located at the $\frac{1}{3}$ grid width positions from the ends. The vertical rods are secured in place at the ends through the same low-friction plastic bushings at the bottom and through stainless steel bearings at the top. The plastic bushings that support the horizontal rods are inlaid inside CNC-machined acrylic plates that attach to the permanent frame between the contraction and the test section. The plates measure 164 mm in width and span the entire inner portion of the permanent frame. They are designed to sit flush with the walls of the test section so that the flow downstream is not affected. The plates are also designed to be removable. The vertical rods are secured at the top through bearings mounted inside a custom-designed aluminium frame. The rods are then attached to the motors through a stainless steel flexible coupling

and a custom-made stainless steel coupling. This coupling is designed to interface between the flexible coupling and the motor, which have different diameter shafts. The coupling is secured onto the motor via set screws. The motors for the vertical rods are secured onto the aluminium frame, which is in turn fastened onto the permanent frame for the active grid. The horizontal rods are connected to the motors through the same mechanism, except for a custom-made water-tight mounting box for the motor. The water-tight box features a custom-designed double lip seal from Trelleborg AB sandwiched between a plastic bushing and a stainless steel bearing. The bushing is on the wet side of the seal while the bearing is on the dry side. The same custom-made coupling mentioned previously goes through the seal assembly to connect to the motor, and the motor is mounted to the dry side of the water-tight box. Large drainage openings are milled into the water-tight box so that in the event of a leakage, the water would drain away before reaching the motor, thus protecting the motors from water damage. The entire vertical rod assembly, which includes the rods with wings, aluminium frame and motors, is designed to be removable as one unit, while the horizontal rods are designed to be removable from the flexible couplings. The motors for the horizontal rods along with the water-tight boxes are permanently mounted to the side of the frame.

The motors used are STM23S-3RE stepper motors from Moons Ltd. (also marketed as Applied Motion Products in other countries). The motors are equipped with internal encoders and motion controllers. Power is supplied by two TDK-Lambda 48 V 52 A DC power supplies. Each motor can draw up to 2.5 A at 48 V. The motors are daisy-chained together and connected to a PCI serial adapter card in a computer. Unique ASCII names are given to each motor for identification by the controlling scripts. Control commands are generated and transmitted through MATLAB scripts, which can independently control each motor's rotation speed, acceleration, direction and duration. To the authors' best knowledge, this is the largest active grid installation for a water channel facility in the world at the time of writing.

Appendix C. A note on the empirical parameter of Hancock & Bradshaw (1983)

Seminal experimental works on the influence of FST on a TBL from the 1980s placed emphasis on both the turbulence intensity and the integral scale (Hancock & Bradshaw 1983, 1989; Castro 1984). In fact, Hancock & Bradshaw (1983) developed an empirical parameter, $\beta = (u'_\infty/U_\infty)/(L_{u,\infty}/\delta + 2)$, which appeared to correlate well with the wall shear stress and wake in their flows. More recent studies have placed more emphasis on the turbulence intensity – e.g. Dogan *et al.* (2016); Hearst *et al.* (2018) – with the latter even proposing that for higher turbulence intensities, the integral scale does not necessarily play a significant role. The primary difference between the earlier studies and contemporary ones is that the recent use of active grids has allowed for high turbulence intensity ($>10\,\%$) to be achieved much farther downstream from the turbulence generating grid ($x/M > 30$). Hearst *et al.* (2018) noticed that one of the reasons for this result appeared to be that δ adjusts itself such that the peak in the premultiplied energy spectrum is at approximately $\sim 10\delta$. This appeared to be true for all 17 of their cases with $7\,\% \lesssim u'_\infty/U_\infty \lesssim 13\,\%$, see their figure 1(*b*). This was in fact first noticed by Dogan *et al.* (2016) in their figure 8, although they did not emphasize it as strongly. This is also approximately true in the present investigation, particularly for the more turbulent cases, as depicted in figure 14. This relationship suggests that given sufficient coevolution distance, the energy containing scales and the boundary layer height adjust to keep a constant proportionality between them (Hearst *et al.* 2018). Thus, $L_{u,\infty}$ and δ are co-dependent, and the ratio $L_{u,\infty}/\delta$ is relatively constant, whilst the turbulence intensity decays, resulting in the appearance

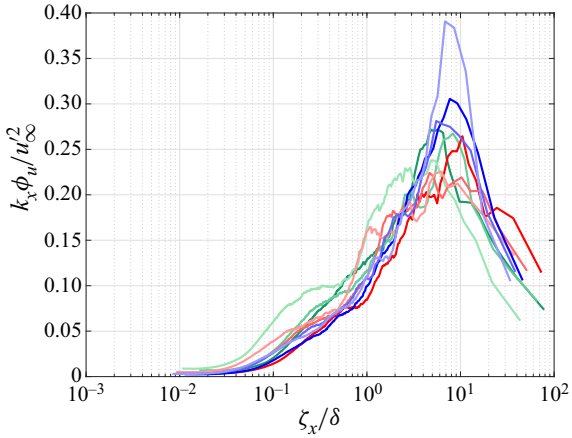

FIGURE 14. Normalized pre-multiplied velocity spectra in the freestream for cases A solid green line, B solid red line, C solid blue line with fading colours indicating increasing streamwise distance from the grid.

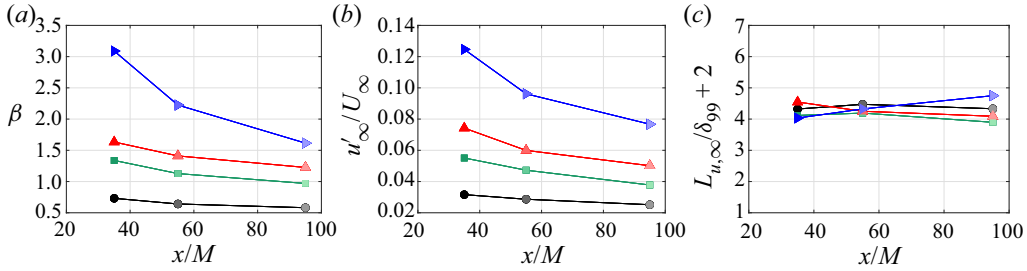

FIGURE 15. Analysis of the empirical parameter β introduced by Hancock & Bradshaw (1983) for cases REF ●; A ■, green; B ▲, red; C ▸, blue. Note that the scaling on these figures was chosen to represent equal changes in β and the two contributing parameters included in it.

of primary dependence on the turbulence intensity. It is important to acknowledge that although this result has been observed in two different facilities, it is possible that it is a consequence of the integral scales produced in those studies, and that if significantly larger or smaller integral scales were investigated, a different result or trend may emerge.

For completeness, we present β along with u'_∞/U_∞ and $L_{u,\infty}/\delta + 2$ in figure 15, with the y-axis scaled to show the same percentage change on all figures. It is evident that when scaled in this way, β predominantly follows u'_∞/U_∞, and $L_{u,\infty}/\delta + 2$ is approximately constant. In §§ 4 and 5 it was also shown that for cases with similar $L_{u,\infty}/\delta$, the mean profiles and spectrograms could look very different. Thus, while the integral scale likely does play some role, this role is small compared to the turbulence intensity and evolution history, at least for the test cases investigated herein.

REFERENCES

ADRIAN, R. J. & YAO, C. S. 1986 Power spectra of fluid velocities measured by laser Doppler velocimetry. *Exp. Fluids* **5** (1), 17–28.

ANDERSON, J. D. 2010 *Fundamentals of Aerodynamics*. McGraw-Hill Education.

BAARS, W. J., HUTCHINS, N. & MARUSIC, I. 2016 Spectral stochastic estimation of high-Reynolds-number wall-bounded turbulence for a refined inner-outer interaction model. *Phys. Rev. Fluids* **1** (5), 054406.

BLAIR, M. F. 1983*a* Influence of free-stream turbulence on turbulent boundary layer heat transfer and mean profile development, part ii—analysis of results. *Trans. ASME: J. Heat Transfer* **105** (1), 41–47.

BLAIR, M. F. 1983*b* Influence of free-stream turbulence on turbulent boundary layer heat transfer and mean profile development, part i—experimental data. *Trans. ASME: J. Heat Transfer* **105** (1), 33–40.

BOYER, L. & SEARBY, G. 1986 Random sampling: distortion and reconstruction of velocity spectra from fast Fourier-transform analysis of the analog signal of a laser Doppler processor. *J. Appl. Phys.* **60** (8), 2699–2707.

CASTRO, I. P. 1984 Effects of free stream turbulence on low Reynolds number boundary layers. *Trans. ASME: J. Fluids Engng* **106** (3), 298–306.

CHAUHAN, K. A., MONKEWITZ, P. A. & NAGIB, H. M. 2009 Criteria for assessing experiments in zero pressure gradient boundary layers. *Fluid Dyn. Res.* **41** (2), 021404.

COLES, D. 1956 The law of the wake in the turbulent boundary layer. *J. Fluid Mech.* **1** (2), 191–226.

COMTE-BELLOT, G. & CORRSIN, S. 1966 The use of a contraction to improve the isotropy of grid-generated turbulence. *J. Fluid Mech.* **25** (4), 657–682.

DEVINANT, P., LAVERNE, T. & HUREAU, J. 2002 Experimental study of wind-turbine airfoil aerodynamics in high turbulence. *J. Wind Engng Ind. Aerodyn.* **90** (6), 689–707.

DOGAN, E., HANSON, R. E. & GANAPATHISUBRAMANI, B. 2016 Interactions of large-scale free-stream turbulence with turbulent boundary layers. *J. Fluid Mech.* **802**, 79–107.

DOGAN, E., HEARST, R. J. & GANAPATHISUBRAMANI, B. 2017 Modelling high Reynolds number wall–turbulence interactions in laboratory experiments using large-scale free-stream turbulence. *Phil. Trans. R. Soc.* A **375** (2089), 20160091.

DOGAN, E., HEARST, R. J., HANSON, R. E. & GANAPATHISUBRAMANI, B. 2019 Spatial characteristics of a zero-pressure-gradient turbulent boundary layer in the presence of free-stream turbulence. *Phys. Rev. Fluids* **4** (8), 084601.

EITEL-AMOR, G., ÖRLÜ, R. & SCHLATTER, P. 2014 Simulation and validation of a spatially evolving turbulent boundary layer up to $Re_\theta = 8300$. *Intl J. Heat Fluid Flow* **47**, 57–69.

ERTUNÇ, Ö., ÖZYILMAZ, N., LIENHART, H., DURST, F. & BERONOV, K. 2010 Homogeneity of turbulence generated by static-grid structures. *J. Fluid Mech.* **654**, 473–500.

ESTEBAN, L. B., DOGAN, E., RODRÍGUEZ-LÓPEZ, E. & GANAPATHISUBRAMANI, B. 2017 Skin-friction measurements in a turbulent boundary layer under the influence of free-stream turbulence. *Exp. Fluids* **58** (9), 115.

FERRANTE, A. & ELGHOBASHI, S. 2004 On the physical mechanisms of drag reduction in a spatially developing turbulent boundary layer laden with microbubbles. *J. Fluid Mech.* **503**, 345–355.

GANAPATHISUBRAMANI, B. 2018 Law of the wall for small-scale streamwise turbulence intensity in high-Reynolds-number turbulent boundary layers. *Phys. Rev. Fluids* **3** (10), 104607.

HANCOCK, P. E. & BRADSHAW, P. 1983 The effect of free-stream turbulence on turbulent boundary layers. *Trans. ASME: J. Fluids Engng* **105** (3), 284–289.

HANCOCK, P. E. & BRADSHAW, P. 1989 Turbulence structure of a boundary layer beneath a turbulent free stream. *J. Fluid Mech.* **205**, 45–76.

HEARST, R. J., BUXTON, O. R. H., GANAPATHISUBRAMANI, B. & LAVOIE, P. 2012 Experimental estimation of fluctuating velocity and scalar gradients in turbulence. *Exp. Fluids* **53** (4), 925–942.

HEARST, R. J., DOGAN, E. & GANAPATHISUBRAMANI, B. 2018 Robust features of a turbulent boundary layer subjected to high-intensity free-stream turbulence. *J. Fluid Mech.* **851**, 416–435.

HEARST, R. J. & LAVOIE, P. 2015 The effect of active grid initial conditions on high Reynolds number turbulence. *Exp. Fluids* **56** (10), 185.

HUTCHINS, N. & MARUSIC, I. 2007 Evidence of very long meandering features in the logarithmic region of turbulent boundary layers. *J. Fluid Mech.* **579**, 1–28.

ISAZA, J. C., SALAZAR, R. & WARHAFT, Z. 2014 On grid-generated turbulence in the near- and far field regions. *J. Fluid Mech.* **753**, 402–426.

KANG, H. S., CHESTER, S. & MENEVEAU, C. 2003 Decaying turbulence in an active-grid-generated flow and comparisons with large-eddy simulation. *J. Fluid Mech.* **480**, 129–160.

KOZUL, M., HEARST, R. J., MONTY, J. P., GANAPATHISUBRAMANI, B. & CHUNG, D. 2020 Response of the temporal turbulent boundary layer to decaying free-stream turbulence. *J. Fluid Mech.* **896**, A11.

LARSSEN, J. V. & DEVENPORT, W. J. 2011 On the generation of large-scale homogeneous turbulence. *Exp. Fluids* **50** (5), 1207–1223.

LASKARI, A., DE KAT, R., HEARST, R. J. & GANAPATHISUBRAMANI, B. 2018 Time evolution of uniform momentum zones in a turbulent boundary layer. *J. Fluid Mech.* **842**, 554–590.

LAVOIE, P., DJENIDI, L. & ANTONIA, R. A. 2007 Effects of initial conditions in decaying turbulence generated by passive grids. *J. Fluid Mech.* **585**, 395–420.

MAKITA, H. 1991 Realization of a large-scale turbulence field in a small wind tunnel. *Fluid Dyn. Res.* **8**, 53.

MALDONADO, V., CASTILLO, L., THORMANN, A. & MENEVEAU, C. 2015 The role of free stream turbulence with large integral scale on the aerodynamic performance of an experimental low Reynolds number S809 wind turbine blade. *J. Wind Engng Ind. Aerodyn.* **142**, 246–257.

MARUSIC, I., CHAUHAN, K. A., KULANDAIVELU, V. & HUTCHINS, N. 2015 Evolution of zero-pressure-gradient boundary layers from different tripping conditions. *J. Fluid Mech.* **783**, 379–411.

MARUSIC, I., MCKEON, B. J., MONKEWITZ, P. A., NAGIB, H. M., SMITS, A. J. & SREENIVASAN, K. R. 2010 Wall-bounded turbulent flows at high Reynolds numbers: recent advances and key issues. *Phys. Fluids* **22** (6), 065103.

MARUSIC, I., MONTY, J. P., HULTMARK, M. & SMITS, A. J. 2013 On the logarithmic region in wall turbulence. *J. Fluid Mech.* **716**, R3.

MOHAMED, M. S. & LARUE, J. C. 1990 The decay power law in grid-generated turbulence. *J. Fluid Mech.* **219**, 195–214.

MONKEWITZ, P. A., CHAUHAN, K. A. & NAGIB, H. M. 2008 Comparison of mean flow similarity laws in zero pressure gradient turbulent boundary layers. *Phys. Fluids* **20** (10), 105102.

PERRY, A. E., MARUSIC, I. & JONES, M. B. 1998 New evolution equations for turbulent boundary layers in arbitrary pressure gradients. *Sadhana* **23** (5), 443–457.

PRANDTL, L. 1905 über Flüssigkeitsbewegung bei sehr kleiner Reibung. In *Proceedings of the 3rd International Congress of Mathematicians, Heidelberg, 1904*, *Leipzig*, pp. 485–491. B. G. Teubner.

RAUSHAN, P. K., SINGH, S. K. & DEBNATH, K. 2018 Grid generated turbulence under the rigid boundary influence. *J. Wind Engng Ind. Aerodyn.* **182**, 252–261.

RODRÍGUEZ-LÓPEZ, E., BRUCE, P. J. K. & BUXTON, O. R. H. 2015 A robust post-processing method to determine skin friction in turbulent boundary layers from the velocity profile. *Exp. Fluids* **56** (4), 68.

SHARP, N. S., NEUSCAMMAN, S. & WARHAFT, Z. 2009 Effects of large-scale free stream turbulence on a turbulent boundary layer. *Phys. Fluids* **21** (9), 095105.

SILLERO, J. A., JIMÉNEZ, J. & MOSER, R. D. 2013 One-point statistics for turbulent wall-bounded flows at Reynolds numbers up to $\delta^+ \approx 2000$. *Phys. Fluids* **25** (10), 105102.

SMITS, A. J. & MARUSIC, I. 2013 Wall-bounded turbulence. *Phys. Today* **66** (9), 25.

STEFES, B. & FERNHOLZ, H. H. 2004 Skin friction and turbulence measurements in a boundary layer with zero-pressure-gradient under the influence of high intensity free-stream turbulence. *Eur. J. Mech. B/Fluids* **23** (2), 303–318.

THOLE, K. A. & BOGARD, D. G. 1996 High freestream turbulence effects on turbulent boundary layers. *Trans. ASME: J. Fluids Engng* **118** (2), 276–284.

VINCENTI, P., KLEWICKI, J., MORRILL-WINTER, C., WHITE, C. M. & WOSNIK, M. 2013 Streamwise velocity statistics in turbulent boundary layers that spatially develop to high Reynolds number. *Exp. Fluids* **54** (12), 1629.

WANG, S., ZHOU, Y., ALAM, M. M. & YANG, H. 2014 Turbulent intensity and Reynolds number effects on an airfoil at low Reynolds numbers. *Phys. Fluids* **26** (11), 115107.

WU, X. & MOIN, P. 2009 Direct numerical simulation of turbulence in a nominally zero-pressure-gradient flat-plate boundary layer. *J. Fluid Mech.* **630**, 5–41.

WU, X., MOIN, P., WALLACE, J. M., SKARDA, J., LOZANO-DURÁN, A. & HICKEY, J.-P. 2017 Transitional–turbulent spots and turbulent–turbulent spots in boundary layers. *Proc. Natl Acad. Sci.* **114** (27), E5292–E5299.

WU, X., WALLACE, J. M. & HICKEY, J.-P. 2019 Boundary layer turbulence and freestream turbulence interface, turbulent spot and freestream turbulence interface, laminar boundary layer and freestream turbulence interface. *Phys. Fluids* **31** (4), 045104.

YOU, J. & ZAKI, T. A. 2019 Conditional statistics and flow structures in turbulent boundary layers buffeted by free-stream disturbances. *J. Fluid Mech.* **866**, 526–566.

The influence of freestream turbulence on the temporal pressure distribution and lift of an airfoil

Journal of Wind Engineering & Industrial Aerodynamics 209 (2021) 104456

Contents lists available at ScienceDirect

Journal of Wind Engineering & Industrial Aerodynamics

journal homepage: www.elsevier.com/locate/jweia

The influence of freestream turbulence on the temporal pressure distribution and lift of an airfoil

Leon Li , R. Jason Hearst *

Department of Energy and Process Engineering, Norwegian University of Science and Technology, Kolbjørn Hejes vei 2, 7034, Trondheim, Norway

ARTICLE INFO

Keywords:
Wind turbine airfoil
Grid turbulence

ABSTRACT

To gain insight on how freestream turbulence (FST) affects the aerodynamics of an airfoil in a systematic manner, the present study investigates a NREL S826 airfoil subjected to seven different incoming flows with varying degrees of FST. The Reynolds number was held at $Re_c = 4.0 \times 10^5$, while the turbulence intensity (T_i) was varied between 0.4% and 5.4%. An increase in T_i increases the maximum lift while having negligible effects on the stall angle. The lift slope in the linear region also generally increased with higher T_i. The latter observation contrasts with some earlier studies, and incoming flow homogeneity is a potential contributing factor to the differences seen here. Periodic pressure fluctuations are seen in the computed lift time-series signal when T_i is between 1% and 2% and the airfoil is operating in the linear region. These fluctuations arise from surface pressure oscillations that are likely excited by the relatively low incoming T_i. The overall effect is a reduction in the time-averaged lift under these operating conditions. At higher T_i, more energetic boundary layers develop over the airfoil's suction side and the effect of these periodic pressure fluctuations is suppressed, leading to an increase in the produced lift.

1. Introduction

Airfoils employed in the field often experience a wide range of incoming flow conditions, especially within the atmospheric boundary layer (ABL); for example, wind turbines in a wind farm or an aircraft on its landing approach. Within the ABL, turbulent flow is inevitable due to the presence of shear, different terrain, and weather systems. In such conditions, the airfoil's flow characteristics can have significant variations. Mücke et al. (2011) conducted a survey at the GROWIAN facility in Germany to measure the atmospheric turbulence intensity between 50 m and 150 m in elevation, and found that the freestream turbulence intensity (T_i) can exceed 40%, with the average being between 5% and 10%. These large variations can have significant impact on the aerodynamic performance of airfoils operating within this environment. Here, $T_i \equiv \langle u'^2 \rangle^{1/2}/U$, where u' is the velocity fluctuations, U is the mean velocity, and $\langle \cdot \rangle$ denotes a time average.

Stack (1931) was one of the first to investigate the effect of freestream turbulence (FST) on the aerodynamic properties of an airfoil by means of a coarse screen mounted in a wind tunnel. The airfoil models were placed at approximately 11.3M downstream of the screen, where M is the mesh length. One of the airfoils tested was a NACA0021 profile, and an increase in T_i caused an increase in the maximum lift and the stall angle, while the lift slope in the linear region remained relatively constant. Similar behaviour was observed for the Clark-Y profile, which is a cambered airfoil with medium thickness, except that the lift slope for the Clark-Y decreased with increasing T_i. In contrast, a NACA0006 airfoil (thin and symmetric) did not exhibit a strong dependence on T_i. This early work highlighted that different airfoils, particularly thin and thick airfoils, respond differently to FST. The subsequent decades saw an explosion in the development of airfoils for a wide range of applications. Some of the studies focused on laminar to turbulent transition in the airfoil boundary layer, such as the early works of Owen and Klanfer (1953) and Gaster (1967). This is important for the development of airfoils for low speed, subsonic applications, where a significant portion of the boundary layer over the airfoil surface could be laminar. Mueller et al. (1983) highlighted the sensitivity of airfoil performance to Reynolds number, airfoil surface finish, and FST. They stressed the need for future investigations to carefully isolate the effect of each of these factors that influences the aerodynamics of an airfoil. Hoffmann (1991) tested a NACA0015 airfoil subjected to five different incoming turbulent flows ranging from 0.25% to 12% in T_i created by a set of rods. The airfoil was placed at $x/M = 7.6$ for the highest T_i case. There was a marked increased in the maximum lift and the stall angle when T_i increased from 0.25% to 9%. Furthermore, the maximum lift coefficient (C_l) showed a linear trend

* Corresponding author.
E-mail addresses: leon.li@ntnu.no (L. Li), jason.hearst@ntnu.no (R.J. Hearst).

https://doi.org/10.1016/j.jweia.2020.104456
Received 19 June 2020; Received in revised form 30 October 2020; Accepted 21 November 2020
Available online xxxx

with respect to T_i up to 9%, after which it plateaued. Here $C_l = \frac{L'}{\frac{1}{2}\rho_\infty U_\infty^2 c}$, where L' is the sectional lift force per unit span, ρ_∞ is the freestream fluid density, U_∞ is the freestream velocity, and c is the chord length of the airfoil. Swalwell et al. (2001) investigated a NACA0021 profile subjected to three different T_i at 0.6%, 4%, and 7% at a chord Reynolds number $Re_c \approx 3.5 \times 10^5$. The lift slope did not change significantly, but the stall angle increased with increasing T_i. Butler et al. (2001) studied the effect of different integral length scales on the heat transfer of an array of low-pressure gas turbine blades. It was found that the pressure distribution, Reynolds number, and turbulence intensities had a higher impact on the location of the suction-side boundary layer transition than integral length scale. Although this was primarily a study on heat transfer, it still gave some insights into the aerodynamic behaviour of a highly cambered airfoil exposed to elevated FST. As T_i increases, the transition point moves upstream, and thus more of the airfoil is covered by a turbulent boundary layer, which is more resistant to flow separation. Another experimental study for gas turbine airfoils was done by Michálek et al. (2012) on a T106C low-pressure turbine blade with up to $T_i = 3.2\%$. The overall effect of elevated T_i is that it promotes boundary layer reattachment, consistent with the observations made by Butler et al. (2001). The effect is, however, diminished at higher Reynolds numbers on the order of 10^5. At the lower end of turbulence intensity levels, Huang and Lee (1999) focused on the effect of FST between 0.2% and 0.65% on a NACA0012 profile. It was observed that even for $T_i < 1\%$, FST has a marked positive effect on the maximum lift and stall angle. Wang et al. (2014) extended T_i to 6%, also for a NACA0012 profile, and found a similar increase in the maximum lift at $Re_c = 2.0 \times 10^4$, with no significant variations in the stall angle. Furthermore, the lift slope did not change significantly even at $T_i = 6\%$. It should be noted here that both studies on the NACA0012 profile had Re_c on the order of 10^3 to 10^5, with no clear evidence that the behaviour observed were Reynolds number independent. Ravi et al. (2012a) investigated the lift of a thin flat-plate with an elliptical leading edge and tapered trailing edge subjected to T_i from 1.2% to 12.6%, and found that the lift slope decreased with increasing T_i, while the stall angle increased. The airfoil model for the most turbulent case was placed around $x/M = 13$ downstream of the passive turbulence grid. The differences observed for the lift slope behaviour by Wang et al. (2014) and Ravi et al. (2012a) again highlight the different behaviour of thick and thin airfoils.

Focusing on wind turbine applications, Devinant et al. (2002) observed that the maximum lift and the stall angle of a NACA 65_4-421 airfoil increased with higher T_i, but the lift slope decreased. This is similar to the trend observed by Ravi et al. (2012a) even though the two airfoils investigated are drastically different (thin flat plate for micro aerial vehicles compared to thick cambered airfoils for wind turbines). The FST was generated through passive grids, the largest of which was able to achieve a T_i of 15.4%. Although in this configuration, the airfoil model was placed at $x/M = 5$. At this location, grid generated turbulent flows show significant inhomogeneity in their mean velocity profiles (Ertunç et al., 2010; Hearst and Lavoie, 2014; Isaza et al., 2014). The observed decrease in lift slope with increasing T_i is somewhat contrary to the observations of Wang et al. (2014), as well as with those by Schneemann et al. (2010), who also reported that the lift slope showed no significant change with increasing T_i for a Wortmann FX79-W-151A wind turbine airfoil. Furthermore, Wang et al. (2014) found the effects of FST on their lift curve to be limited to near stall, as only $C_{l,\,\max}$ increased while both the lift slope and stall angle remained relatively constant. Cao et al. (2011) tested a Selig S1223 airfoil with turbulence intensities of 4.1% and 9.5%. The airfoil was originally developed for high-lift low Reynolds number applications, but in their study it is considered as a candidate for vertical axis wind turbines. The stall characteristics are much smoother in the more turbulent case, and this was observed for Reynolds numbers from 5.5×10^4 to 1.0×10^5. Contrary to other studies, there were no significant improvements in either the maximum lift or the stall angle with increasing T_i. Kamada et al. (2011) tested a DU93-W-210 wind turbine airfoil for two flow conditions, T_i at 0.15% and 11%. The trend observed is similar to Devinant et al. (2002) in that the maximum lift increased and the lift slope decreased with elevated T_i. A passive grid was used in this study and the model was placed at about $x/M = 6.6$ downstream. Maldonado et al. (2015) used an active grid to generate T_i of 6.14% for the testing of a NREL S809 wind turbine airfoil. The model was placed at $x/M \approx 39$ downstream of the grid, and an overall improvement in its aerodynamic properties was observed. Both the lift slope and the maximum lift increased, while the stall angle remained the same. The pressure suction peak was also higher for every angle of attack (α) except 0°. Particle image velocimetry (PIV) analysis showed that at $\alpha = 16°$, the flow separation point is farther downstream on the suction side with higher T_i. Li et al. (2016) tested a self-developed wind turbine airfoil and found that the maximum lift increased with higher T_i, with no significant change to the lift slope in the linear region. The study covered T_i up to 13.9% and Reynolds numbers up to 2.0×10^5. Turbulence was generated by a set of four passive grids, the largest of which was placed $x/M = 7$ upstream of the model. Recently, Sarlak et al. (2018), studying a NREL S826 airfoil, found that an increase in T_i up to 2% gave a significant improvement in the lift performance at $Re_c = 4.0 \times 10^4$, but it offered no visible improvement at $Re_c = 1.0 \times 10^5$. In this case, FST was generated by sets of three wires of different diameters placed $5.5c$ upstream of the airfoil, not by a turbulence grid that covers the entire cross-section of the test-section. As as result, the FST generated by Sarlak et al. (2018) is not homogeneous across the test section. However, the study's main focus was on the dynamic stall behaviour of this airfoil, not on the effect of FST, and has yielded some interesting results that will be discussed later in this section.

Table 1 summarizes the details from selected previous investigations. The numerous studies investigating the effect of FST on airfoil aerodynamics sometimes produce contradictory results. Some reported that the lift slope decreased while the maximum lift increased with increasing FST (Devinant et al., 2002; Ravi et al., 2012a; Kamada et al., 2011), others reported an increase in both the lift slope and the maximum lift (Maldonado et al., 2015), while still others reported no changes to the lift slope (Wang et al., 2014; Schneemann et al., 2010; Li et al., 2016). It would appear that most disagreements are on the behaviour of the lift slope as FST increases. This can be attributed to several factors, including different airfoil profiles, Reynolds number dependency, and incoming flow conditions. The present study seeks to address these three issues. The airfoil profile used for this investigation is the NREL S826 wind turbine airfoil. Originally published by Somers (2005) from the National Renewable Energy Laboratory in the USA, it was designed for horizontal-axis wind turbines with rotor diameters between 20 m and 40 m. This airfoil has already been used in several experimental and numerical studies as a generic reference wind turbine airfoil (e.g., Sarmast and Mikkelsen, 2012; Sarlak et al., 2014; Sarlak and Sørensen, 2018; Sarlak et al., 2018; Yalçın et al., 2018; Bartl et al., 2019; Hann et al., 2020), and the present study seeks to contribute to the growing body of data available. There are some complex flow phenomena for this airfoil at low to moderate Reynolds numbers (4.0×10^4 to 2.0×10^5), such as a stall hysteresis loop and 3-D stall cells. Interestingly, the stall cells are more prominent at $Re_c = 1.0 \times 10^5$ and 2.0×10^5 than at lower Re_c (Sarlak et al., 2018; Sarlak and Sørensen, 2018). Nevertheless, one of the objectives of this study is to remove Reynolds number dependence as a potential factor that influences the aerodynamic characteristics of this airfoil. As the goal is to focus only on the effect of FST on pressure and lift behaviour, it is desirable that the Reynolds number be kept as high as possible. The design Reynolds number of this airfoil is $\sim 1.5 \times 10^6$. While this was not achievable with our present experimental facility, the experiments were conducted at a sufficiently high Reynolds number to remove any Reynolds number dependence, as will be shown in later sections. Thus, the results obtained are representative of the field behaviour of this airfoil.

The incoming flow homogeneity is another potential factor contributing to the observed differences in lift slope behaviour. As stated earlier,

Table 1
Summary of selected previous studies on the effect of FST on airfoil aerodynamics; ↑ denotes increase, ↓ denotes decrease, and ≈ denotes constant. Missing information are denoted by ·. The experimental parameters of the present study are also listed for comparison purposes. x/M^* is the position of the airfoil relative to the turbulence generating grid for the highest T_i case only. x/M for Sarlak et al. (2018) is not applicable as they used sets of three wires instead of a space-filling turbulence grid.

Study	Geometry	Application	Re_c [$\times 10^3$]	T_i [%]	x/M^*	$C_{l,\,max}$	As FST increases, Stall α	Lift slope
	USA 35-A	·				↓	·	·
	USN PS6	·				↓	·	·
Stack (1931)	Clark-Y	General	52–3400	·	11.3	↑	↑	↓
	NACA0006	General				≈	·	·
	NACA0021	General				↑	↑	≈
Swalwell et al. (2001)	NACA0021	General	350	0.6–7	·	↑	↑	≈
Huang and Lee (1999)	NACA0012	General	82–173	0.2–0.7	·	↑	↑	≈
Wang et al. (2014)	NACA0012	General	5.3–20	0.6–6	14	↑	≈	≈
Hoffmann (1991)	NACA0015	General	250	0.25–12	7.6	↑	↑	≈
Cao et al. (2011)	S1223	Low *Re*	55–100	4.1–9.5	12.4	≈	≈	≈
Ravi et al. (2012a)	Thin flat plate	Low *Re*	75	1.2–12.6	13	↑	↑	↓
Devinant et al. (2002)	NACA 65_4-421	Wind turbine	100–700	0.5–15.4	5	↑	↑	↓
Schneemann et al. (2010)	FX79-W-151A	Wind turbine	700	$<1-6.7$	·	↑	↑	≈
Kamada et al. (2011)	DU93-W-210	Wind turbine	350	0.5, 11	6.6	↑	↑	↓
Maldonado et al. (2015)	NREL S809	Wind turbine	208	6.14	39	↑	≈	↑
Li et al. (2016)	Self-developed	Wind turbine	50–200	0.15–13.9	7	↑	↑	≈
Sarlak et al. (2018)	NREL S826	Wind turbine	40	0.1–1.9	N/A	↑	≈	↑
			100	0.2–1.7	N/A	≈	≈	≈
Present study	NREL S826	Wind turbine	400	0.4–5.4	16.1	↑	≈	↑

flow conditions at $x/M < 10$ show significant inhomogeneity in both the mean velocity and the velocity fluctuation profiles (Ertunç et al., 2010; Hearst and Lavoie, 2014; Isaza et al., 2014). Typically for grid turbulence, approximately homogeneous isotropic turbulence is achieved at around $x/M = 30$ (e.g., Comte-Bellot and Corrsin, 1966). This is important for experimental aerodynamics for airfoils as the forces are typically either directly measured or integrated from pressure distributions. The latter is especially sensitive to flow inhomogeneity as it only computes the sectional lift at one span location, and if the flow is inhomogeneous, it follows that the computed forces are highly dependent on the spanwise location of the measurement plane. Direct force measurements give the averaged forces across the entire measured span, thus integrating the inhomogeneous effects. It follows that the results would vary depending on the degree of flow inhomogeneity. In addition, it has been documented that at high α, airfoils can develop 3-D stall structures on the surface near stall (Sarlak et al., 2018; Sarlak and Sørensen, 2018). Any non-uniformity in the incoming flow is likely to interact with these 3-D structures and cause unintentional effects. Thus, in order to isolate the effect of FST on the aerodynamic behaviour of an airfoil, particularly near stall, the incoming flow needs to be as homogeneous as possible. There is evidence in previous studies that flow inhomogeneity has a general effect on airfoil aerodynamics. The investigations of Devinant et al. (2002) and Kamada et al. (2011) were performed at $x/M = 5$ and 6.6, respectively, and both reported a decrease in the lift slope with increasing T_i. In contrast, Maldonado et al. (2015) performed their experiments at $x/M = 39$, within the homogeneous flow region, and reported the opposite behaviour. All three investigations performed tests at ~ 5% turbulence intensity on wind turbine airfoils.

The present investigation incorporates combinations of passive turbulence grids to generate seven different T_i, the largest of which has the airfoil model located at a similar mesh lengths distance as Wang et al. (2014), who reported a root mean squared velocity profile variation of less than 0.9%. Additionally, the T_i achieved in the present study are representative of the flow conditions seen in the field. Given that modern wind turbines often have tip speed ratios (TSRs) between 6 and 8 for maximum power efficiency (Bianchi et al., 2007), and the largest wind gusts can exceed 40% (Mücke et al., 2011), it follows that the actual T_i experienced by the majority of the blade is below 10%. This is especially true for the S826 airfoil, which is primarily intended to be used at the tip section of the blade, corresponding to the 0.95 blade radial position. A typical atmospheric T_i of 10% would correspond to a T_i of 1.7% as experienced by the rotor tips, assuming a TSR of 6. The T_i range chosen for this study, the highest of which is 5.4%, thus covers the expected field flow conditions for this airfoil. We would like to note that although the T_i values of the present study match those found in field, we cannot match the scales of turbulent eddies found in typical ABLs, which can exceed the turbine size.

Lastly, we seek to combine the spectral analyses of the pressure and lift coefficients with their time-averaged counterparts. Spectral analysis of the lift coefficients has been done by Blackburn and Melbourne (1996) and Sicot et al. (2006) on a cylinder and an airfoil respectively, while Ravi et al. (2012b) and Watkins et al. (2010) performed spectral analysis on the pressure distributions. Sarlak et al. (2018) analyzed the surface pressure fluctuations of the NREL S826 airfoil, but stopped short of examining the frequency content of the fluctuations. There has been very few studies to date that focus on the temporal analysis of pressure on an airfoil surface. To the authors' knowledge, this is the first attempt at combining the spectral analyses of both the lift and pressure signals with their time-averaged counterparts for a study on the aerodynamics of an airfoil subjected to different turbulent incoming flows.

2. Experimental equipment and procedure

The experiment was performed in the large closed-loop wind tunnel at the Norwegian University of Science and Technology. The test section has a rectangular cross section measuring 1.85 m × 2.71 m, and its length is 11.15 m. The wind tunnel is driven by a 220 kW fan controlled via a variable frequency drive. The fan is located downstream of the test section. The roof panels of the test section are adjustable to achieve an approximately zero-pressure gradient potential core in the test section. The maximum speed achievable is around 23 m/s. The wind tunnel is instrumented with a Pitot-static tube near the inlet of the test section and a thermocouple for temperature measurements. The dynamic pressure and test section ambient temperature were measured for each α for all the test cases. The ambient atmospheric pressure was measured at the beginning and end of each test case with a mercury barometer.

The airfoil was manufactured from synthetic polyurethane blocks through CNC-machining. The surface is sanded and painted to be aerodynamically smooth. For more information about the airfoil model's design and manufacturing process, see Bartl et al. (2019). The model is

mounted vertically in the test section and secured to a turntable in the floor. No end plates were used because the airfoil extends from the floor to the ceiling and the boundary layer effects have been shown to be negligible in the centre 2/3 of the span (Bartl et al., 2019). Regardless, the sectional pressure measurements do not integrate the loads across the entire airfoil, but only represent the loads in the measurement plane. The leading edge of the airfoil is located 3.85 m, or 8.56c from the inlet of the test section, where $c = 0.45$ m is the chord length of the airfoil. This was fixed due to the mounting mechanism of the model to the turntable. A schematic drawing of the setup can be found in Fig. 1. At the mid-span of the airfoil, there are 32 pressure taps distributed around the circumference, with 19 taps on the suction side and 13 taps on the pressure side. The locations of the pressure taps are shown in Fig. 2. The pressure taps are connected to a Scanivalve MPS4264 miniature pressure scanner mounted inside the model, which can sample all 32 ports simultaneously. The turntable enables α to be changed from -8° to $+18^\circ$, covering the operating, stall, and post-stall regions of the airfoil. The maximum blockage ratio of the model is estimated to be about 5.6%. Blockage correction was not applied as this is within the range where such corrections can be avoided (West and Apelt, 1982). Indeed, the freestream velocity is only increased by less than 0.2% according to the solid blockage correction estimated from Barlow et al. (1999), which is within the measurement accuracy of the present set-up. At each α, the pressure distribution data was measured with the scanner at 800 Hz for 60 s. The pressure time-series signals were digitally filtered with a 7th-order low-pass Butterworth filter at a cutoff frequency $f_c = 140$ Hz in order to remove the frequency content associated with the noise floor. The sampling frequency of 800 Hz is well above the required Nyquist frequency for this cutoff. It should be noted here that 140 Hz represents the frequency response limitation of the setup, and not the frequency bound of the underlying physics. The freestream velocity U_∞ was set to 14.5 m/s, for a chord Reynolds number $Re_c = 4.0 \times 10^5$.

Additional tests were carried out for $Re_c = 2.0 \times 10^5$, 3.0×10^5, and 4.4×10^5 for different freestream turbulence levels ranging from $<1\%$ to 4% to check for Reynolds number invariance of the lift and pressure characteristics. Fig. 3 shows the lift coefficients for $T_i = 0.40\%$ and 3.93%. It can be seen that the lift curves for $Re_c = 4.0 \times 10^5$ and 4.4×10^5 collapse with each other for both cases, and thus the behaviour of the airfoil is effectively Reynolds number independent at the primary test Re_c. We chose to test this airfoil at this Re_c because we want to remove Reynolds number dependence as a potential factor that influences the aerodynamic behaviour assessed in the present experiments. Numerous previous studies have demonstrated the Reynolds number dependence of this airfoil at low to moderate Reynolds numbers of around 10^5, and our test Re_c avoids this flow regime. Bartl et al. (2019) also found the lift characteristics of this airfoil to be relatively Reynolds number independent for $Re_c \geq 4.0 \times 10^5$. We note that this is still an order of magnitude below the intended operating conditions for this airfoil, $Re_c \approx 1.5 \times 10^6$ (Somers, 2005), but is in the highest range of achievable Re_c in this experimental facility and roughly Re_c-independent for this range of Reynolds numbers.

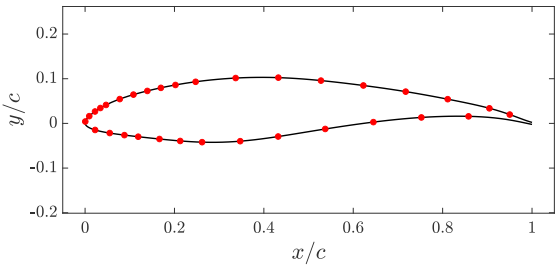

Fig. 2. Airfoil cross section with pressure port locations marked in solid red circles. (For interpretation of the references to colour in this figure legend, the reader is referred to the Web version of this article.)

To generate the turbulent freestream flows, four different passive grids were used in combination to create a total of seven different flow cases, including a quasi-laminar reference case denoted as REF. The freestream turbulence intensity, T_i, for REF measured at the leading edge of the airfoil is around 0.40%. This flow was achieved by mounting a fine steel mesh, which is one of the grids used, at the test section inlet. The other different flow conditions were made by having two locations for inserting the grids. The first one is placed at the inlet of the test section, and the second location is 2.57 m downstream. The physical properties of the four grids are listed in Table 2. The seven different incoming flows and their homogeneity and turbulence statistics are provided in Table 3. For the two-grid configurations, the normalized airfoil leading edge location, x/M, is measured from the second grid and uses the mesh size of the second grid. Due to the limitation of the setup, the location of the airfoil model was fixed with respect to the wind tunnel, and its position relative to the grids varies with different grid configurations. The naming convention given to the six turbulent flow cases contains the T_i values measured at the leading edge of the airfoil at mid-span, rounded to the first decimal place. For the most turbulent case FST5.4, the airfoil was located 16.1M downstream of the aft grid. The root mean squared (RMS) variation in U for this flow case is $I_U/U\ (y) = 0.88\%$ as shown in Table 3, where $I_U = \left(\frac{1}{N-1}\sum (U(y_i) - \overline{U(y)})^2\right)^{\frac{1}{2}}$ is the standard deviation of the velocity profile, and $U\ (y)$ is the averaged value of the spanwise velocity profile. While 16.1M is less than the 30M usually found in the literature for homogeneous isotropic grid turbulence, it is still much farther downstream than the set-up in Devinant et al. (2002), and is similar to Wang et al. (2014), who reported $I_U/U < 0.9\%$ at 14M.

The turbulence statistics were measured with a Dantec 55P11 single hot-wire probe. It has a tungsten sensing element measuring 1.25 mm in

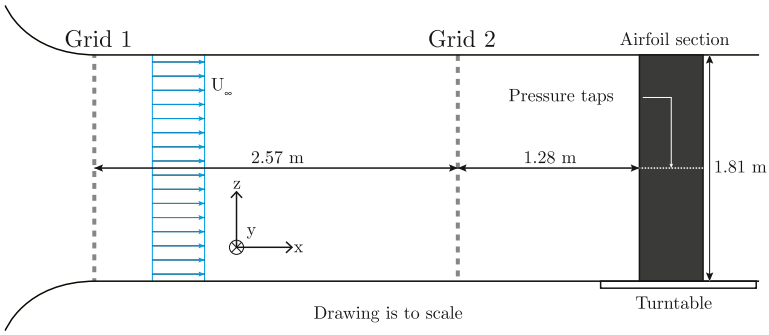

Fig. 1. Schematic of the experimental setup.

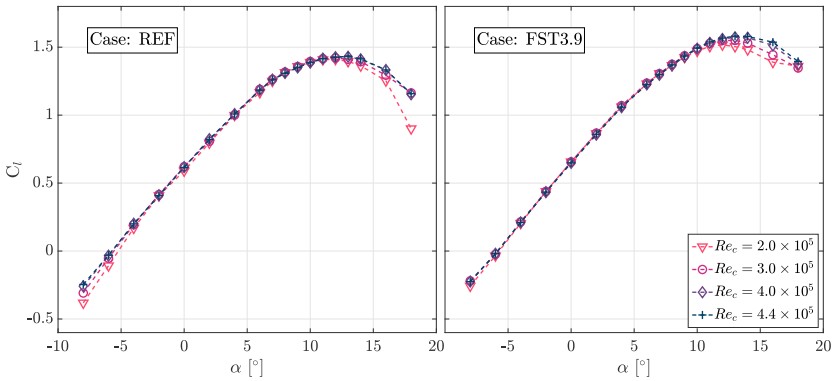

Fig. 3. Lift coefficient for REF and FST3.9 for multiple Reynolds numbers.

Table 2
Summary of the grid physical properties.

Grid	Description	Mesh length, M	Solidity, σ
SG1	Mono-planar steel square mesh	3.00 mm	0.33
SG2	Mono-planar steel square grid	40.0 mm	0.44
WG1	Bi-planar wooden square grid	123 mm	0.33
WG2	Bi-planar wooden square grid	240 mm	0.35

Table 3
Summary of the flow homogeneity and turbulence properties of the incoming flows. The turbulence properties are taken at the leading edge of the airfoil, at mid-span. x/M is measured from the farthest downstream grid (when there is one grid, it is Grid 1; when there are two grids, it is Grid 2).

Case	Grid 1	Grid 2	x/M	I_U/U (y) [%]	u'/U [%]	L_{ux}/c
REF	SG1	–	1638	0.43	0.40	–
FST1.1	SG2	SG1	546	0.44	1.13	0.067
FST1.6	SG2	–	96.4	0.58	1.61	0.073
FST2.1	WG1	SG1	546	0.25	2.14	0.100
FST3.0	WG1	–	31.3	0.58	3.00	0.131
FST3.9	WG2	SG1	546	0.42	3.93	0.156
FST5.4	WG2	–	16.1	0.88	5.39	0.227

length and 5 μm in diameter. The probe was operated at an overheat ratio of 1.8, and was controlled via a Dantec StreamLine Pro anemometer. To measure the turbulence statistics at the leading edge of the airfoil, the probe was secured to a rigid metal stand that was fastened to the test section floor. Homogeneity scans were carried out by mounting the probe via a sting to a traverse system with three degrees of freedom. To avoid mechanical vibrations of the hot-wire holder, the homogeneity scans were performed at a lower Reynolds number of 3.0×10^5. This is, however, still representative of the flow homogeneity at the test chord Reynolds number of 4.0×10^5 since homogeneity in grid turbulence is largely Reynolds number independent (e.g., Larssen and Devenport, 2011). The scan consists of 17 equally spaced measurement points spanning $-1.6 \leq y/c \leq +1.6$. The overall uncertainty in the measured turbulence intensity is estimated to be on the order of 1% according to the method of Benedict and Gould (1996). Standard Reynolds decomposition is used to separate the velocity $u(y)$ into a time-averaged component $U(y)$ and a fluctuating component $u'(y)$, namely $u(y) = U(y) + u'(y)$. Fig. 4 shows the flow homogeneity profiles of the normalized freestream velocity $U(y)/U_0$, velocity fluctuation $u'(y)/U(y)$, and integral length scale $L_{ux}(y)/c$ for all the cases. U_0 is the average of $U(y)$ for each case.

3. Mean pressure distributions and lift coefficients

The time-averaged pressure measurements were computed for each pressure port location. The same technique as used by Bartl et al. (2019) was used here to close and integrate the normalized pressure distribution $C_p = \frac{P-P_\infty}{\frac{1}{2}\rho_\infty U_\infty^2}$, where P is the local surface pressure and P_∞ is the freestream static pressure. Fig. 5 shows the C_p distributions for all test cases at selected α. The angles shown are the zero-lift angle ($\alpha \approx -6°$), the zero angle, linear region angles ($\alpha = 6°, 10°$), the stall angle ($\alpha = 13°$), and a post-stall angle ($\alpha = 18°$). The REF measurements presented herein are in good agreement with previous measurements on the same model in the same facility using different equipment (Bartl et al., 2019). For the turbulent cases, it can be observed that within the linear range ($-6° \leq \alpha \leq 7°$), cases with higher FST exhibit more negative C_p values around the suction peak, which implies that more lift is generated for these cases. At

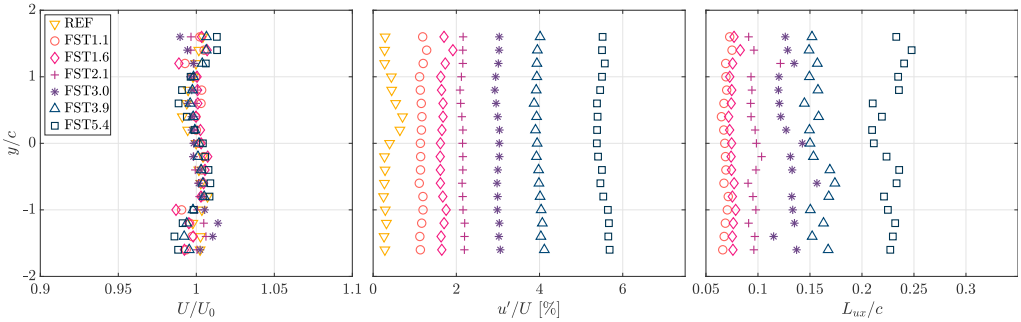

Fig. 4. Flow homogeneity profiles for all test cases for U/U_0, u'/U [%], and L_{ux}/c.

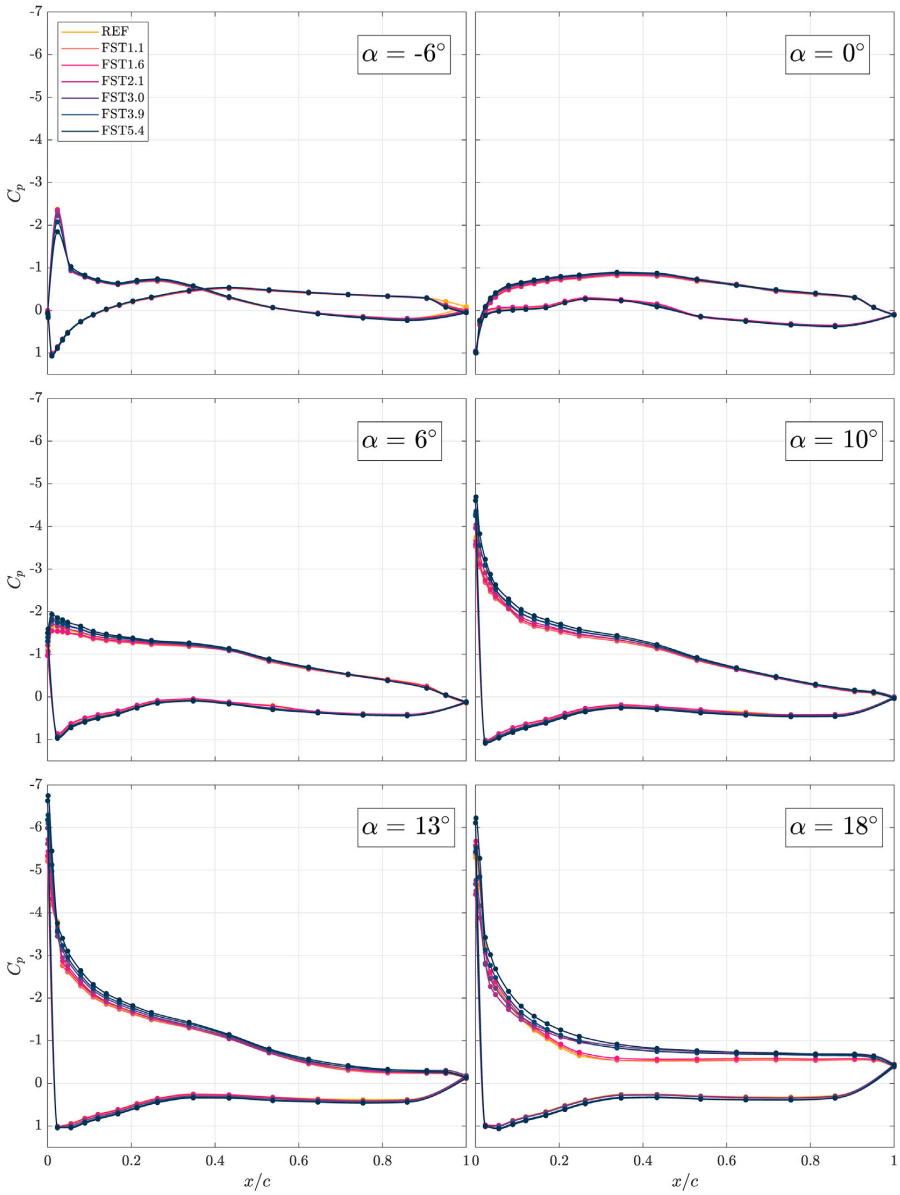

Fig. 5. Pressure coefficient C_p for all cases at selected α.

the highest α, there is a distinct grouping of the C_p distribution on the suction side for $x/c > 0.1$. Cases where $T_i > 2\%$ show a gentler pressure recovery and more negative values than cases with $T_i < 2\%$. Flow separation on the airfoil surface causes a region with relatively constant low pressure, and this manifests as plateaus in the suction side C_p distribution. The start of the plateaus marks the start of the separated flows. The C_p distributions at $\alpha = 18°$ show a delayed onset of the plateau region for $T_i > 2\%$. This suggests that flow separation in the post-stall region under elevated FST is delayed.

Fig. 6 shows the C_l vs. α relation for all test cases calculated from integrating the C_p distributions. The pressure drag can be similarly calculated, however, it is just one, relatively small, constituent part of the total drag and thus we primarily focus on the lift in the present work. Both the maximum lift and the lift slope in the linear region generally increase with T_i, while C_l for $\alpha \leq -4°$ remains relatively unaffected by FST. The zero-lift angle remains constant at $-6°$ for all cases and appears to be the point where the C_l curves "fan out" as FST increases. This behaviour is consistent with the observations of previous studies such as Devinant et al. (2002) and Wang et al. (2014). Fig. 7 shows the extracted maximum lift coefficient from each case, and it can be seen that $C_{l,\,\max}$ is relatively constant from REF to $T_i = 1.1\%$, then it increases in a linear fashion with respect to T_i. This is consistent with the observations of Devinant et al. (2002) and Wang et al. (2014). The stall angle where $C_{l,\,\max}$ is reached appears unaffected by turbulence intensity, as it remains

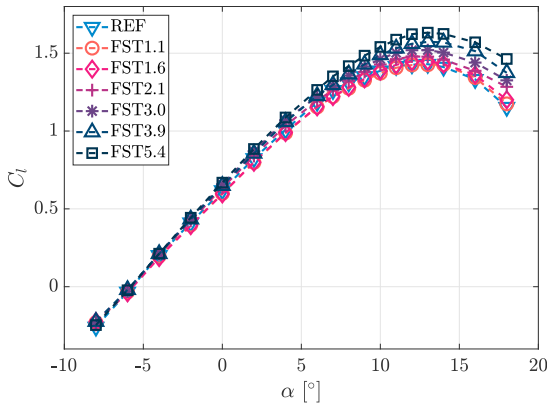

Fig. 6. Lift coefficient C_l for all test cases at $Re_c = 4.0 \times 10^5$.

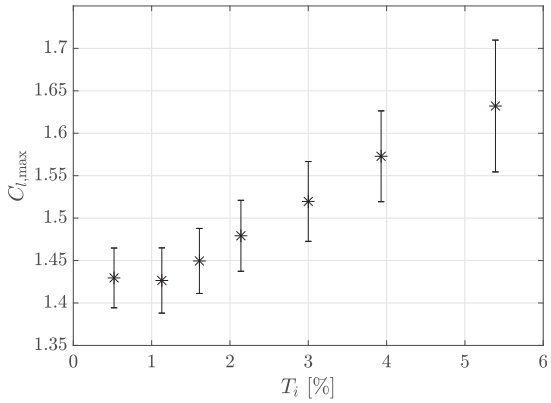

Fig. 7. $C_{l,\max}$ at the stall angle for all test cases; marker sizes are representative of the uncertainty for T_i.

relatively constant at $\alpha = 13°$, as can be seen in Fig. 6. This contrasts with the results of Devinant et al. (2002) and Kamada et al. (2011), where the stall angle increased with FST. However, the constant stall angle behaviour agrees with the observations of Wang et al. (2014) and Maldonado et al. (2015). It is possible that flow homogeneity plays a role in the behaviour of stall angles here, as Wang et al. (2014) and Maldonado et al. (2015) conducted their experiments farther downstream of their grids ($x/M = 14$ and 39, respectively) than Devinant et al. (2002) and Kamada et al. (2011) ($x/M = 5$ and 6.6, respectively). The stall angle behaviour in the present study agrees with Wang et al. (2014) and Maldonado et al. (2015) in that it remains constant, and the common feature is that all three studies were sufficiently far from the grids, suggesting a grid-based dependency of the other two studies. We would like to note that this is not conclusive evidence that flow homogeneity is the most significant factor in the stall angle behaviour, as other factors exist, such as the different airfoil profiles.

The lift slopes in the linear range for all cases are shown in Fig. 8. The first two cases, FST1.1 and FST 1.6, show lower lift slopes than REF, while all other cases with greater T_i show higher values. It would appear that T_i between 1% and 2% causes a reduction in lift in the linear range, while T_i greater than 2% increases lift. These trends are more prominently shown in Fig. 9, where the relative difference of C_l compared to REF is plotted. There is a clear division into two distinct groups based on T_i. FST1.1 and FST1.6 show consistently lower C_l in the linear region than

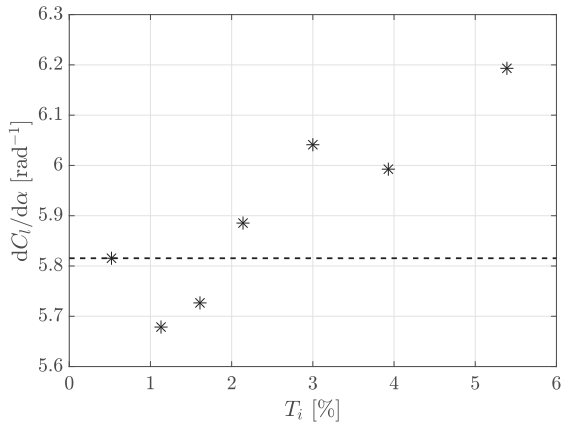

Fig. 8. C_l slope in the linear region for all test cases; the dotted line denotes the lift slope of REF.

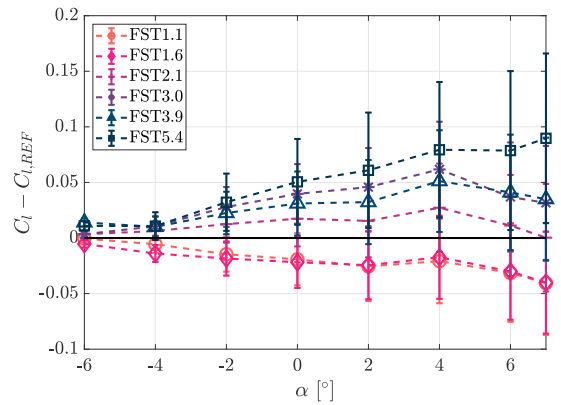

Fig. 9. C_l differences in the linear region for all test cases compared to REF.

REF while all the other cases show higher C_l. It should be noted that the differences shown by FST1.1 and FST1.6 in C_l are near the limit of the estimated uncertainties in the measurements. Nevertheless, the C_l for these two cases in the linear region are consistently lower than that of REF, suggesting the observed trend is real. Upon further examination of the C_p distributions, it was found that this decrease in C_l for FST1.1 and FST1.6 is caused by a reduction in the suction peak region. An example at $\alpha = 7°$ is shown in Fig. 10. The differences in C_p is the greatest at the suction peak.

The overall effect of increasing the FST is an increase in $C_{l,\max}$ and a general increase in the lift slope within the linear region. However, for relatively low T_i (between 1% and 2%), both the lift slope and the absolute C_l values are lower than those for REF in the linear region. This is caused by a reduction in the suction peak of the C_p distributions. In the next section, analysis of the magnitude and frequency content of the fluctuating pressure time-series gives additional insight into the dependence of the pressure and lift characteristics of the airfoil on FST.

4. Time-series analysis of the pressure and lift

While several studies (e.g., those listed in Table 1) have investigated the mean aerodynamic properties for airfoils in FST, as discussed in the previous section, very few explore the time-series information. The RMS

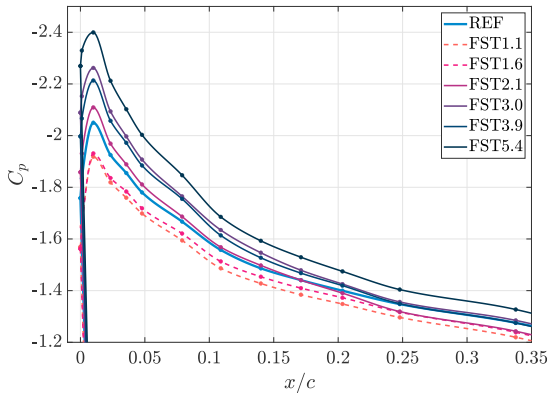

Fig. 10. C_p for $\alpha = 7^\circ$ for all cases, focusing on the suction peak region.

of the suction side pressure fluctuations, p', is calculated for each pressure port for all angles of attack. The results are plotted as contours in Fig. 11, which are normalized by the maximum pressure fluctuations p'_{max} when $\alpha = 16^\circ$ for each case. The locations of laminar separation bubbles (LSBs) are superimposed unto the contours. Laminar separation bubbles are regions of recirculating flow, and their presence can be detected through the time-averaged C_p distributions. Separation is marked by the start of a pressure "plateau" on the suction side, laminar-turbulent transition marked by the end of the plateau, and reattachment marked by the return to "normal" pressure recovery on the suction side (Gaster, 1967). Example C_p distributions are shown in Fig. 12 along with the identification of the separation (S), transition (T), and reattachment (R) points. A grey dotted line is added to $\alpha = 2^\circ$ in Fig. 12 in order to highlight the signature that LSBs leave on the C_p distribution. The grey line qualitatively represents the C_p distribution if the bubble were not present. The separation point is marked by where the C_p starts to deviate from the grey line, showing a slower pressure recovery; the transition point is marked by a sudden increase in pressure recovery; and the reattachment point is marked by where the C_p returns to the grey line. Due to the relatively high Reynolds number of the present study, the C_p signature of the LSBs, if present, is not always well-defined, as can be seen in the lack of an identifiable separation point for $\alpha = 7^\circ$ for REF in Fig. 12. Therefore, Fig. 11 only shows the separation, transition, and reattachment points of the LSBs that are clearly identifiable from the C_p distributions. The flow separation points associated with near- and post-stall conditions are also included, as marked by the start of a region of constant pressure near $x/c = 0.3$ for $\alpha = 18^\circ$ for REF in Fig. 12. At $\alpha = 18^\circ$, there is a delay in the separation point for cases where $T_i > 2\%$ (FST2.1, FST 3.0, FST3.9, and FST5.4). Furthermore, in these cases, the pressure fluctuations at the leading edge are significantly higher at $\alpha = 18^\circ$ than all the other α. For REF, FST1.1, and FST1.6, this was not observed. The relatively large leading edge pressure fluctuations suggest that the boundary layer is highly energetic at the leading edge, and that the more energetic boundary layer delays flow separation on the suction side of the airfoil at $\alpha = 18^\circ$. This is consistent with the observed higher C_l values at this α for these cases, as well as the delayed separation point extracted from the C_p distributions.

Another observation is that in REF, FST1.1, and FST1.6, the chordwise location of the maximum C_p fluctuations moves upstream with increasing α. This manifests as a series of peaks in Fig. 11 that propagate upstream with increasing α. The peak locations correspond to the transition-reattachment regions found through the C_p distribution, as can be seen in the superimposed points. This suggests that the peaks in the pressure fluctuations on the suction side are associated with the transition and reattachment process in the LSBs. For the other cases, the peaks decrease in prominence, which is reflected in the decreasingly identifiable separation and reattachment points in the C_p distributions. Examining the bubble regions in Fig. 11, it can be observed that for α between 0° and 7°, the bubbles form between $0.5 < x/c < 0.8$. Additionally, small separation bubbles near the leading edge can be observed for α between 9° and 13°. Like the larger bubbles at lower α, these small bubbles also leave decreasingly identifiable signatures on the C_p distributions as T_i increases. Furthermore, for α between 0° and 7°, the relative pressure fluctuations at the leading edge is significantly higher for cases where T_i is greater than 2%. As the pressure fluctuations are normalized by the maximum fluctuations, which occurs near the leading edge, it shows that as T_i increases, the relative intensity of the leading edge pressure fluctuations increase. The observed effect of this is a reduction in the relative pressure fluctuation intensities associated with the separation bubbles. This suggests that the effect of laminar separation bubbles, if present, on the surface pressure fluctuations decrease with increasing T_i.

The increase in leading edge pressure fluctuations can be better observed in Fig. 13, which shows the normalized differences in the suction side pressure fluctuations with respect to REF. For FST1.1 and FST1.6, the differences near the leading edge are not significantly different from the rest of the suction side. However, starting from FST2.1, the leading edge pressure fluctuation differences become much higher than the rest of the suction side, and the region where this difference is prominent expands with increasing T_i. In addition, the pressure fluctuation differences at the highest α for FST2.1 to FST5.4 are significantly higher than that of the other α. This reflects the earlier observation of high levels of pressure fluctuations for these cases at this α, and of delays in flow separation that results in higher C_l in this post-stall region. It is also interesting to note that when REF is subtracted from the other cases, the series of peaks in the pressure fluctuations observed in REF in Fig. 11 leaves its trace in all the difference contours in Fig. 13. The trace manifests itself as a series of negative peaks in the contours, revealing that the pressure fluctuations associated with bubble transition and reattachment in REF are higher than those in the other cases. It is also evident that as FST increases, the pressure fluctuations along this trace decrease, reflected through the increasingly negative values seen in the peaks. This further suggests that as FST increases, the effect of laminar separation bubbles on the flow over the suction side decreases, and it is instead increasingly dominated by the more energetic boundary layer at the leading edge.

Fig. 14 examines the frequency content of the suction side pressure fluctuations at $\alpha = 4^\circ$, 12°, and 18°, representing the linear, near-stall, and post-stall regimes. Localized peaks near normalized frequencies $fc/U_\infty = 0.1$ and 0.2 are observed for nearly all conditions shown. These peaks also extend over the entire suction side surface. These peaks are most prominent for FST1.1 and FST1.6, where we also see a cluster of secondary peaks near $fc/U_\infty = 1$ over the entire surface for $\alpha = 4^\circ$. This secondary cluster is reduced in prominence for cases with higher FST, and is more restricted to the aft portion of the airfoil, as opposed to the entire surface for FST1.1 and FST1.6. In fact, as FST increases, more and more of the airfoil suction side exhibits more energetic pressure fluctuations across a broad bandwidth than the energy contained in this cluster of secondary peaks near $fc/U_\infty = 1$. Similar behaviour is observed for $\alpha = 12^\circ$, except at this angle, the front portion of the airfoil for FST1.1 and FST1.6 exhibits stronger pressure fluctuations across a broad bandwidth, similar to the behaviour seen for higher FST cases. It is postulated that these secondary surface pressure fluctuations are causing flow instabilities on the suction side, which in turn leads to a reduction in the time-averaged lift produced by the airfoil. The increased FST in the other flow cases is believed to have influenced the flow on the suction side sufficiently such that the pressure fluctuations at $fc/U_\infty = 1$ are suppressed, so that they do not have an adverse impact on the overall lift performance of the airfoil. While we do not make the claim here that vortex shedding is present in the airfoil's wake under the tested flow conditions, it is possible that these pressure fluctuations are traces left by potential velocity fluctuations in the flow around the airfoil, and that the

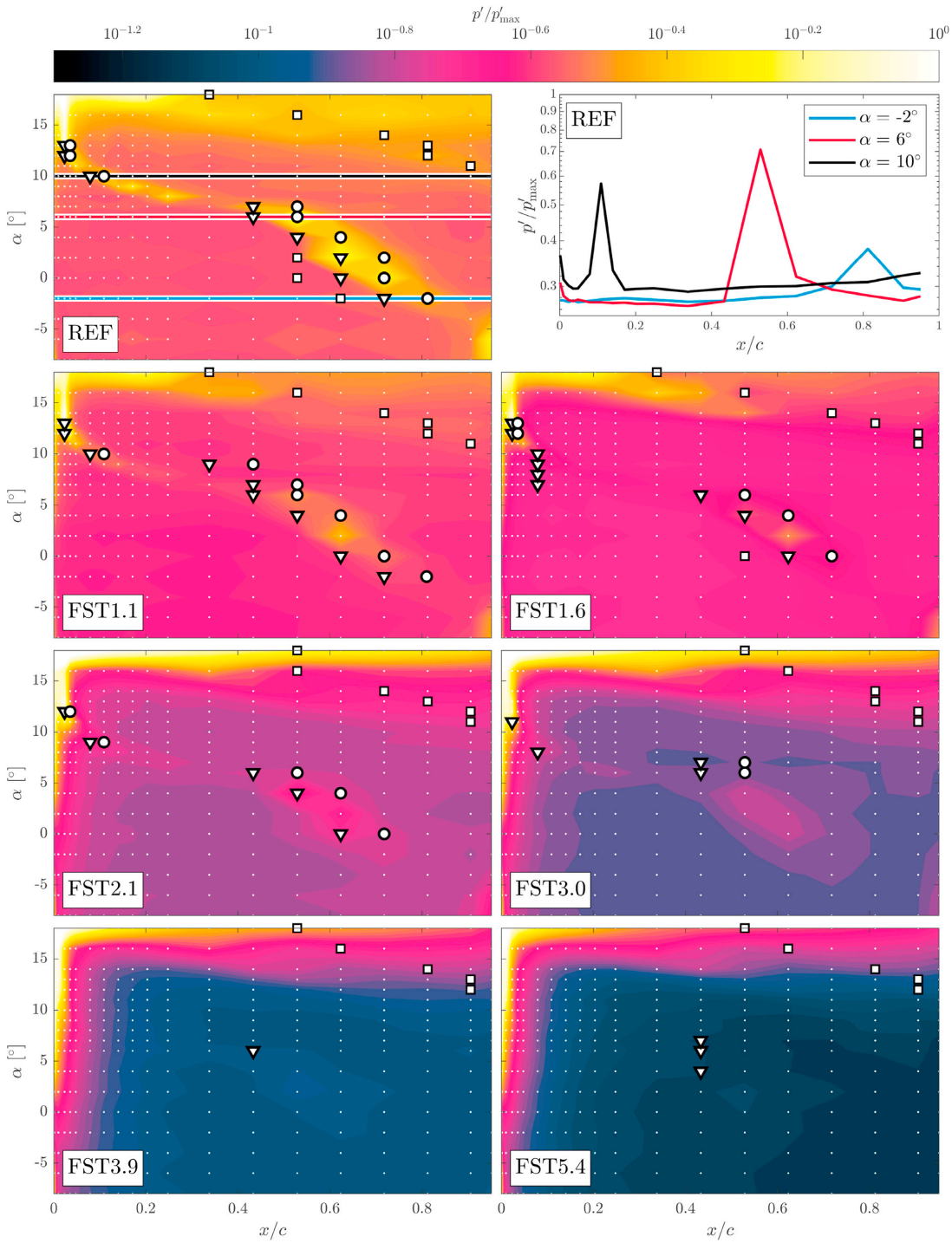

Fig. 11. Normalized suction side pressure fluctuations. Example 2-D pressure fluctuations are also plotted for REF for selected α, highlighting the progression of the fluctuation peak as α increases; the corresponding αs are noted in the contour for REF as horizontal lines. The transition and reattachment points estimated from the C_p distributions are superimposed; ($\triangledown$) denotes transition, ($\circ$) denotes reattachment, and ($\square$) denotes separation. When no symbols are present for a given α, it implies that these points cannot be distinctly identified through the C_p distributions. The white dots identify measurement points.

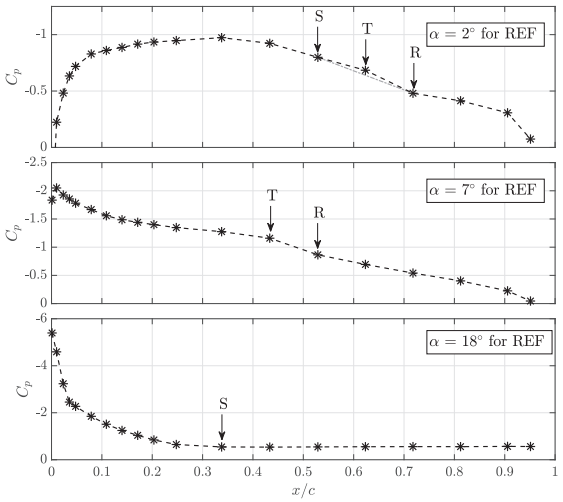

Fig. 12. Example suction side C_p distributions for demonstrating the identification of separation (S), transition (T), and reattachment (R) points for LSBs and near- and post-stall flow separation. A grey dotted line is added to the C_p distribution for $\alpha = 2°$ to highlight the C_p signature of a LSB.

elevated T_i has a suppression effect on them. Interestingly, this cluster of secondary peaks appears to be the least prominent in REF, where FST is the lowest. This suggests that T_i between 1% and 2% excites these fluctuations, leading to their noticeable presence in FST1.1 and FST1.6. Taniguchi et al. (2012) found that low FST (<4%) causes noticeable velocity fluctuations to develop in the shear layer of LSBs through Kelvin-Helmholtz instabilities on a low pressure turbine blade. At higher T_i, bypass transition occurs in the airfoil boundary layer, leading to an overall diminished effect of the LSBs on the flow field. Similar observations have been made by Istvan and Yarusevych (2018) for a NACA0018 airfoil. Fransson et al. (2005) found that in a boundary layer on a flat plate, the initial disturbance energy $E = u'^2/U^2$ scales with T_i^2, which implies that a small increment in T_i can lead to a large increase in the initial disturbance energy in the boundary layer, leading to an earlier onset of bypass transition. It is possible that in the present study, when the FST is relatively low (between 1% and 2%), it amplified the velocity fluctuations in the LSB shear layer while not being strong enough to induce an early onset of bypass transition in the boundary layer. These velocity fluctuations then leave their signature in the surface pressure fluctuations as peaks near $fc/U_\infty = 1$. As T_i increases, it becomes strong enough to induce an early onset of bypass transition, thus diminishing the overall effect of the LSBs, leading to a suppression of these peaks. This earlier onset of bypass transition in the boundary layer can potentially be reflected by the leading edge pressure exhibiting increasingly energetic fluctuations across a broad bandwidth, starting from FST2.1. This is consistent with the observation of increased pressure fluctuations at the leading edge as FST increases. It is also interesting to note that for REF, FST1.1, and FST1.6 at $\alpha = 18°$, the front portion of the airfoil experiences high energy pressure fluctuations at relatively low frequencies ($fc/U_\infty < 0.1$), while the aft portion of the airfoil does not. This can be seen in Fig. 14 as two groupings of the spectra for $fc/U_\infty < 0.1$, for REF, FST1.1, and FST1.6 at $\alpha = 18°$. The split in the grouping occurs near $x/c = 0.3$, which is where flow separation occurs as identified from the C_p distributions. For all the other cases, the pressure fluctuations extend across most of the airfoil and include higher frequency content. The change is also gradual as opposed to the abrupt change seen in REF, FST1.1, and FST1.6. This observation further suggests that the increased T_i beyond 2% is able to energize the boundary layer sufficiently to delay flow separation in the post-stall region. Lastly, the increase in energy associated with the pressure fluctuation peaks caused by laminar separation bubbles can be seen in Fig. 14 as elevated spectra in comparison to their neighbours. The increase in energy is broadband, suggesting that the transition and reattachment mechanisms do not influence the airfoil surface pressure within that region at distinct frequencies.

Fig. 15 shows the spectrogram of the computed C_l time-series for all cases. In FST1.1 and FST1.6, traces of the pressure spectral peaks near $fc/U_\infty = 0.2$ and 1 are evident in the spectra for C_l. The peak at $fc/U_\infty = 0.2$ is less prominent in REF, and all localized peaks are suppressed in the other flow cases with higher FST. The main difference in the C_l spectrograms between REF, FST1.1, and FST1.6 is the presence of the peaks near $fc/U_\infty = 1$ for the latter cases. It suggests the possible presence of LSB shear layer velocity fluctuations as observed by Taniguchi et al. (2012), and that these fluctuations are amplified by the relatively low T_i. As the FST increases, the high energy pressure fluctuations observed near the leading edge dominate the frequency space behaviour of C_l.

Finally, the partial variance of C_l is calculated by integrating the PSD from $f = 20$ Hz–40 Hz, as the secondary peaks near $fc/U_\infty = 1$ correspond to $f \approx 30$ Hz. This is done to examine the fraction of the fluctuations contained near the secondary peaks. The results are shown in Fig. 16, normalized by the total C_l variance. From $\alpha = 5°$–$14°$, FST1.1 and FST1.6 show the highest fraction in terms of energy contained in the fluctuations near $fc/U_\infty = 1$, while REF shows the lowest. This is consistent with the results shown in the C_l spectrogram, as well as the pressure fluctuation PSDs, in that FST1.1 and FST1.6 show the most prominent peaks near $fc/U_\infty = 1$, and that their C_l are most affected by them. In order to reduce data clutter, only REF, FST1.1, FST1.6 and FST3.9 are shown in Fig. 16, but these cases are representative.

The analyses of the pressure and computed C_l time-series suggest that areas of high pressure fluctuations are associated with the transition and reattachment mechanisms of LSBs. Pressure fluctuations at certain localized frequencies are seen for FST1.1 and FST1.6, and to a lesser extent for REF. They can be potentially related to vortex shedding in the LSB shear layer as observed by Taniguchi et al. (2012). Higher levels of T_i diminish the overall effects of these pressure fluctuations on C_l, possibly through inducing an earlier onset of bypass transition in the boundary layer, as was observed by Istvan and Yarusevych (2018). This has the effect of reducing the influence of LSBs on the airfoil. Indeed the appearance of these localized peaks in the C_l spectrogram for FST1.1 and FST1.6 suggests that these fluctuations are possibly causing flow instabilities to develop over the suction side. This is a possible cause for the reduction of the suction peak in the time-averaged C_p, with the overall effect being a reduction in the time-averaged lift produced by the airfoil.

5. Conclusions

In the present study, a reference wind turbine airfoil was subjected to seven different incoming flows with varying turbulence intensities. It was found that an increase in T_i caused a general increase in the maximum lift coefficient, which is consistent with past investigations into other airfoils. The lift slope was also found to increase with increasing T_i. This contrasts with the findings from some previous studies, but this is suspected to be caused by differences in the homogeneity of the incoming flow. Wang et al. (2014) and Maldonado et al. (2015) reported lift slopes that were either unchanged or increased with increasing T_i; both studies had strong flow homogeneity at a position well downstream of the turbulence generation, similar to the present investigation. We do not make the claim that flow homogeneity is the most significant factor at play, but it certainly would have an effect. A rigorous investigation of the impact of homogeneity would be insightful, but is out of the scope of the present investigation. The stall angle was not found to be strongly influenced by FST. Through the analysis of C_p distributions and integrated lift curves, it was observed that within the linear operational region of the airfoil, T_i between 1% and 2% caused a reduction in the pressure suction peak compared to the reference quasi-laminar case (REF), and as a consequence, the C_l values decreased. This may be of interest to the field

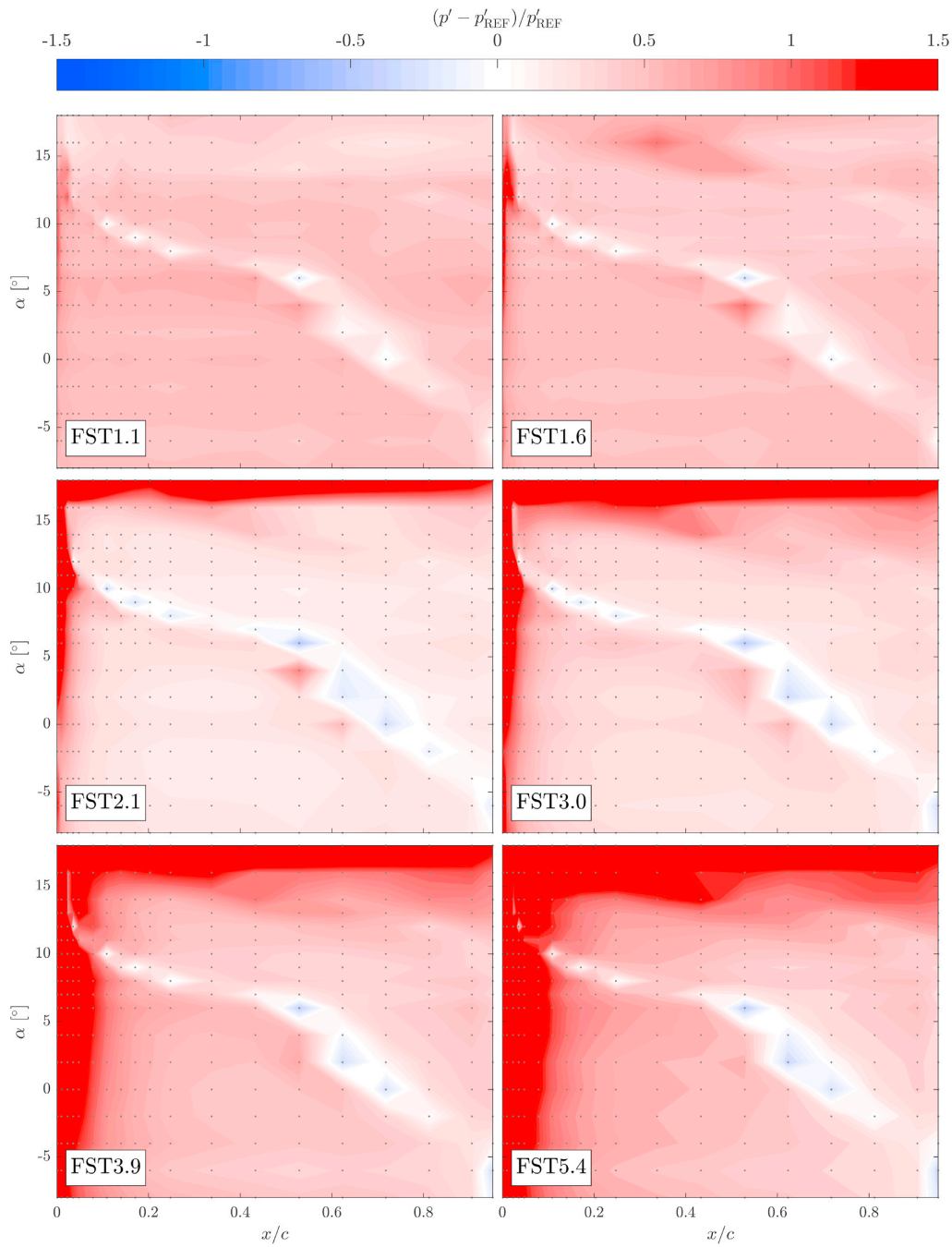

Fig. 13. Normalized suction side pressure fluctuation difference. The grey dots identify measurement points.

application of this airfoil, as it is designed to be used at the tips of rotor blades, and consequently would experience atmospheric turbulence intensities of similar level when TSR is taken into account. At higher values of T_i, the pressure suction peak increased with respect to REF, resulting in both higher absolute values of C_l and C_l slope. Examinations of the frequency content of the surface pressure signals revealed the presence of localized peaks at $fc/U_\infty = 0.2$ and 1 for these low FST cases. It is postulated that T_i between 1% and 2% excites these periodic oscillations, which in turn causes flow instabilities on the suction side of the airfoil. The overall effect is a reduction in the time-averaged lift. Higher T_i

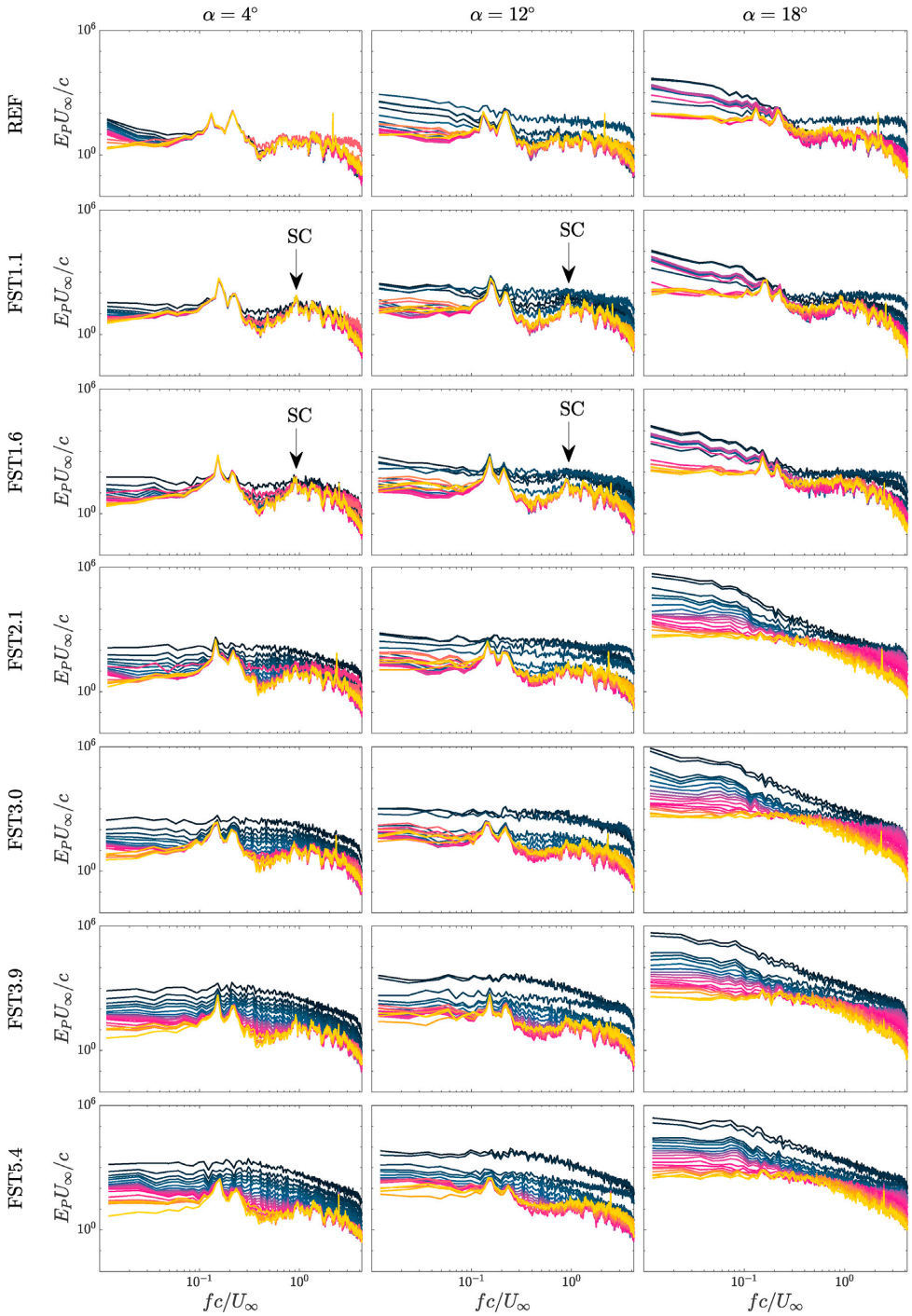

Fig. 14. Normalized suction side pressure fluctuation power spectral density for all flow cases at selected α. The light to dark colours denote pressure port positions from the trailing edge to the leading edge; prominent occurrences of the secondary cluster are marked with an arrow and "SC". (For interpretation of the references to colour in this figure legend, the reader is referred to the Web version of this article.)

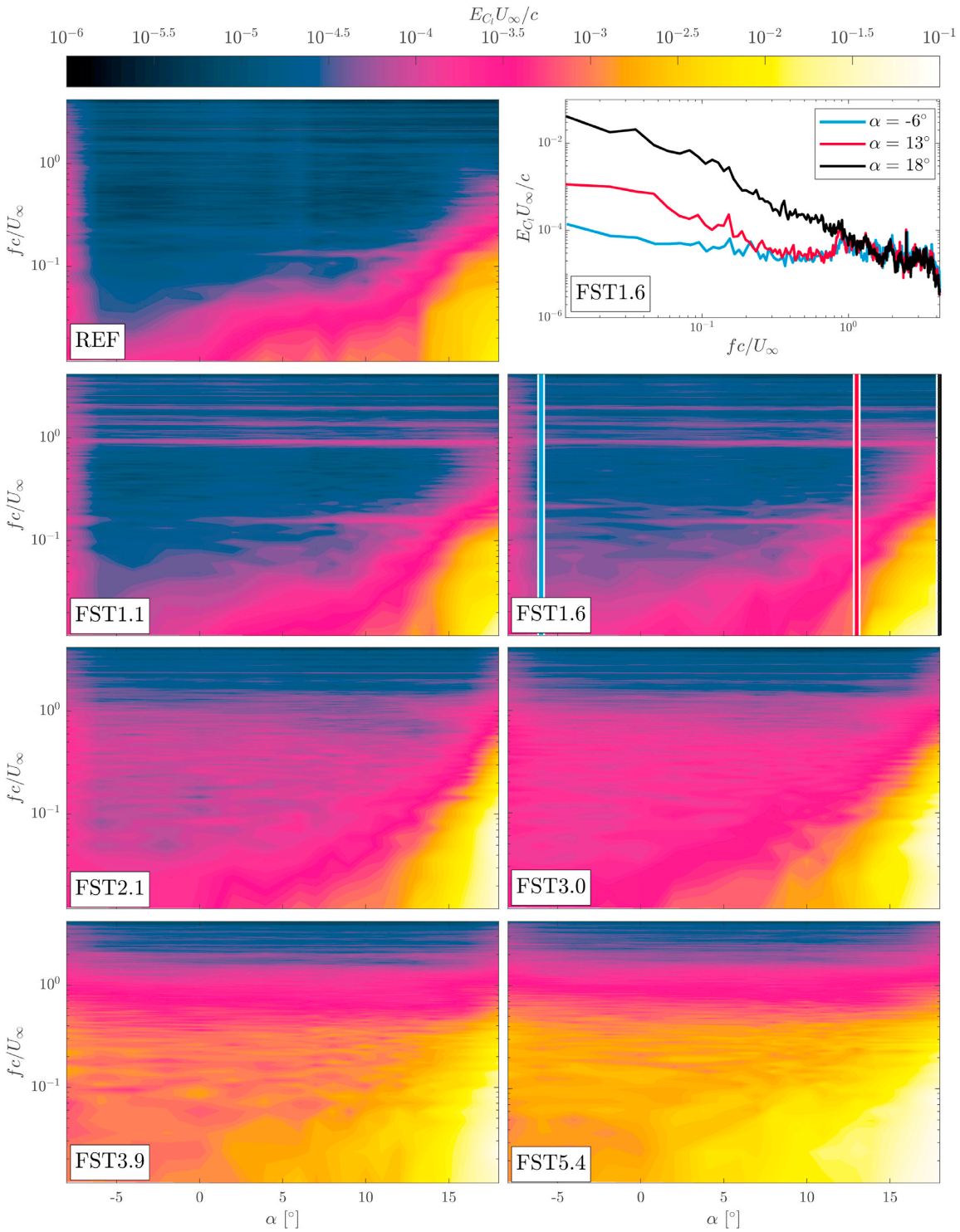

Fig. 15. Normalized spectrogram of the lift coefficient power spectral density for all flow cases. Example 2-D PSDs are plotted for FST1.6 to highlight the local peaks near $fc/U_\infty = 1$. The αs shown in the example plot are highlighted in the spectrogram for FST1.6 as vertical lines.

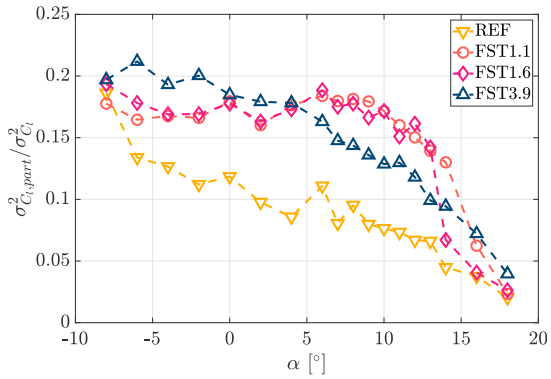

Fig. 16. Partial variance of C_l calculated by integrating the C_l PSD from $f = 20$ Hz–40 Hz, normalized by the total variance. Only REF, FST1.1, FST1.6, and FST3.9 are shown to reduce clutter; the behaviour of FST3.9 is representative of the other omitted cases.

suppressed these peaks, leading to an increase in lift produced by the airfoil. In the post-stall regime, elevated FST delayed flow separation and increased lift.

The present work investigated seven different flow cases, which is more than previous studies of a similar nature. It also combined time-averaged pressure and lift characteristics with the spectral analysis of their frequency content to offer further insight into the underlying physics. Lastly, the turbulence intensities as well as the Reynolds number investigated here are representative of the field application of this airfoil, thus the results presented herein provide valuable performance and validation data for future uses and studies of this airfoil.

Division of work

LL and RJH conceived of the idea for this work. LL conducted the experiments, performed the analysis, and was the primary author of the manuscript with support from RJH. RJH supervised the project. All authors read and contributed to the manuscript.

CRediT authorship contribution statement

Leon Li: Methodology, Software, Formal analysis, Investigation, Writing - original draft, Visualization. **R. Jason Hearst:** Conceptualization, Methodology, Resources, Writing - review & editing, Supervision, Project administration, Funding acquisition.

Declaration of competing interest

The authors declare that they have no known competing financial interests or personal relationships that could have appeared to influence the work reported in this paper.

Acknowledgement

We would like to thank Magnus K. Vinnes and Håkon T. Nygård for their help in setting up and running parts of the experiment. We would also like to thank Professor Ole Øiseth from the Department of Structural Engineering at NTNU for lending us the pressure scanner for the airfoil measurements.

References

Barlow, J.B., Rae, W.H., Pope, A., 1999. Low-speed Wind Tunnel Testing, third ed.Ch. 9. John wiley & sons, pp. 352–355.

Bartl, J., Sagmo, K.F., Bracchi, T., Sætran, L., 2019. Performance of the NREL S826 airfoil at low to moderate Reynolds numbers - a reference experiment for CFD models. Eur. J. Mech. B Fluid 75, 180–192.

Benedict, L., Gould, R., 1996. Towards better uncertainty estimates for turbulence statistics. Exp. Fluid 22 (2), 129–136.

Bianchi, F.D., Mantz, R.J., Battista, H.D., 2007. The Wind and Wind Turbines. Springer.

Blackburn, H.M., Melbourne, W.H., 1996. The effect of free-stream turbulence on sectional lift forces on a circular cylinder. J. Fluid Mech. 306, 267–292.

Butler, R.J., Byerley, A.R., VanTreuren, K., Baughn, J.W., apr 2001. The effect of turbulence intensity and length scale on low-pressure turbine blade aerodynamics. Int. J. Heat Fluid Flow 22 (2), 123–133.

Cao, N., Ting, D.S.-K., Carriveau, R., 2011. The performance of a high-lift airfoil in turbulent wind. Wind Eng. 35 (2), 179–196.

Comte-Bellot, G., Corrsin, S., 1966. The use of a contraction to improve the isotropy of grid-generated turbulence. J. Fluid Mech. 25, 657–682.

Devinant, P., Laverne, T., Hureau, J., jun, 2002. Experimental study of wind-turbine airfoil aerodynamics in high turbulence. J. Wind Eng. Ind. Aerod. 90 (6), 689–707.

Ertunç, O., Özyilmaz, N., Lienhart, H., Durst, F., Beronov, K., 2010. Homogeneity of turbulence generated by static-grid structures. J. Fluid Mech. 654, 473–500.

Fransson, J.H., Matsubara, M., Alfredsson, P.H., 2005. Transition induced by free-stream turbulence. J. Fluid Mech. 527, 1–25.

Gaster, M., 1967. The Structure and Behaviour of Laminar Separation Bubbles. NPL.

Hann, R., Hearst, R.J., Sætran, L.R., Bracchi, T., 2020. Experimental and numerical icing penalties of an S826 airfoil at low Reynolds numbers. Aerospace 7 (4), 46.

Hearst, R.J., Lavoie, P., 2014. Decay of turbulence generated by a square-fractal-element grid. J. Fluid Mech. 741, 567–584.

Hoffmann, J.A., 1991. Effects of freestream turbulence on the performance characteristisc of an airfoil. AIAA J. 29 (9), 1353–1354.

Huang, R.F., Lee, H.W., 1999. Effects of freestream turbulence on wing-surface flow and aerodynamic performance. J. Aircraft 36 (6), 965–972.

Isaza, J., Salazar, R., Warhaft, Z., 2014. On grid-generated turbulence in the near- and far field regions. J. Fluid Mech. 753, 402–426.

Istvan, M.S., Yarusevych, S., 2018. Effects of free-stream turbulence intensity on transition in a laminar separation bubble formed over an airfoil. Exp. Fluid 59 (3), 52.

Kamada, Y., Maeda, T., Murata, J., Toki, T., Tobuchi, A., 2011. Effects of turbulence intensity on dynamic characterstics of wind turbine airfoil. J. Fluid Sci. Technol. 6 (3), 333–341.

Larssen, J.V., Devenport, W.J., 2011. On the generation of large-scale homogenous turbulence. Exp. Fluid 50, 1207–1223.

Li, Q.A., Kamada, Y., Maeda, T., Murata, J., Nishida, Y., 2016. Effect of turbulent inflows on airfoil performance for a Horizontal Axis Wind Turbine at low Reynolds numbers (Part I: static pressure measurement). Energy 111, 701–712.

Maldonado, V., Castillo, L., Thormann, A., Meneveau, C., 2015. The role of free stream turbulence with large integral scale on the aerodynamic performance of an experimental low Reynolds number S809 wind turbine blade. J. Wind Eng. Ind. Aerod. 142, 246–257.

Michálek, J., Monaldi, M., Arts, T., 2012. Aerodynamic performance of a very high lift low pressure turbine airfoil (T106C) at low Reynolds and high mach number with effect of free stream turbulence intensity. J. Turbomach. 134.

Mücke, T., Kleinhans, D., Peinke, J., Feb 2011. Atmospheric turbulence and its influence on the alternating loads on wind turbines. Wind Energy 14 (2), 301–316.

Mueller, T.J., Pohlen, L.J., Conigliaro, P.E., Jansen, B.J., 1983. The influence of free-stream disturbances on low Reynolds number airfoil experiments. Exp. Fluid 1 (1), 3–14.

Owen, P.R., Klanfer, L., 1953. On the Laminar Boundary Layer Separation from the Leading Edge of a Thin Aerofoil. Tech. Rep.. AERONAUTICAL RESEARCH COUNCIL LONDON (UNITED KINGDOM).

Ravi, S., Watkins, S., Watmuff, J., Massey, K., Petersen, P., Marino, M., 2012a. Influence of large-scale freestream turbulence on the performance of a thin airfoil. AIAA J. 50 (11).

Ravi, S., Watkins, S., Watmuff, J., Massey, K., Petersen, P., Marino, M., Ravi, A., 2012b. The flow over a thin airfoil subjected to elevated levels of freestream turbulence at low Reynolds numbers. Exp. Fluid 53, 637–653.

Sarlak, H., Frère, A., Mikkelsen, R., Sørensen, J.N., 2018. Experimental investigation of static stall hysteresis and 3-dimensional flow structures for an NREL S826 wing section of finite span. Energies 11 (6).

Sarlak, H., Mikkelsen, R., Sarmast, S., Sørensen, J.N., 2014. Aerodynamic behaviour of NREL S826 airfoil at Re= 100,000. In: J. Physics: Conference Series, vol. 524. IOP Publishing, 012027.

Sarlak Chivaee, H., Sørensen, J.N., 2018. Characterisation of mushroom structures on airfoils: CFD and wind tunnel investigation. In: 21st Australasian Fluid Mechanics Conference.

Sarmast, S., Mikkelsen, R.F., 2012. The Experimental Results of the NREL S826 Airfoil at Low Reynolds Numbers.

Schneemann, J., Knebel, P., Milan, P., Peinke, J., 2010. Lift measurements in unsteady flow conditions. In: DEWEK 2010.

Sicot, C., Aubrun, S., Loyer, S., Devinant, P., 2006. Unstead characteristics of the static stall of an airfoil subjected to freestream turbulence level up to 16%. Exp. Fluid 41, 641–648.

Somers, D.M., 2005. The S825 and S826 Airfoils. Tech. rep., SR-500-36344, NREL. https://wind.nrel.gov/airfoils/Documents/S825,S826_Design.pdf.

Stack, J., 1931. Test in the variable density wind tunnel to investigate the effects of scale and turbulence on airfoil characteristics. Tech. Rep. 364. NACA.

Swalwell, K.E., Sheridan, J., Melbourne, W.H., 2001. The effect of turbulence intensity on stall of the NACA 0021 aerofoil. In: 14th Australasian Fluids Mechanics Conference.

Taniguchi, H., Sakai, H., Funazaki, K.-i., 2012. Effects of freestream turbulence on bypass transition of separated boundary layer on low-pressure turbine airfoils. J. Therm. Sci. 21 (3), 230–235.
Wang, S., Zhou, Y., Alam, M.M., Yang, H., 2014. Turbulence intensity and Reynolds number effects on an airfoil at low Reynolds number. Phys. Fluids 26 (115107).
Watkins, S., Ravi, S., Loxton, B., 2010. The effect of turbulence on the aerodynamics of low Reynolds number wings. Eng. Lett. 18 (3).
West, G.S., Apelt, C.J., 1982. The effects of tunnel blockage and aspect ratio on the mean flow past a circular cylinder with Reynolds numbers between 10^4 and 10^5. J. Fluid Mech. 114, 361–377.
Yalçın, Ö., Cengiz, K., Özyörük, Y., 2018. High-order detached eddy simulation of unsteady flow around NREL S826 airfoil. J. Wind Eng. Ind. Aerod. 179, 125–134.

The near-field of a lab-scale wind turbine in tailored turbulent shear flows

Renewable Energy 149 (2020) 735–748

Contents lists available at ScienceDirect

Renewable Energy

journal homepage: www.elsevier.com/locate/renene

The near-field of a lab-scale wind turbine in tailored turbulent shear flows

L. Li [a, *], R.J. Hearst [a], M.A. Ferreira [b], B. Ganapathisubramani [b]

[a] Department of Energy and Process Engineering, Norwegian University of Science and Technology, Trondheim, Norway
[b] Engineering and Physical Sciences, University of Southampton, Southampton, UK

ARTICLE INFO

Article history:
Received 16 April 2019
Received in revised form
21 November 2019
Accepted 9 December 2019
Available online 13 December 2019

Keywords:
Wind turbine
Tailored turbulence
Shear flow
Lab-scale

ABSTRACT

Real wind turbines experience a wide range of turbulent shear flows that naturally occur within the atmospheric boundary layer, however, these are often difficult to simulate in experiments. An active grid was used to expand the testable parameter space compared to conventional methods. Specific focus was placed on decoupling the shear from the turbulence intensity. Particle image velocimetry was used to capture the mean velocity and velocity fluctuation fields in the near-field wake of a model wind turbine subjected to seven different combinations of shear and turbulence intensity. It was found that if the incoming mean profile was removed, the velocity deficit is approximately symmetric about the hub, even for highly sheared cases. The absolute wake velocity deficit profiles are asymmetric for the sheared cases, and the combination of the wake and shear flow results in a local increase in shear on the high-velocity side of the wake immediately downstream of the turbine. This in turn leads to higher turbulence production within that region, leading to larger velocity fluctuations. It is also demonstrated that the mean power of the model turbine is not particularly sensitive to the incoming shear, but the power fluctuations scale linearly with the incoming turbulence intensity.

1. Introduction

Wind turbines are often grouped together in wind farms. As a result, many individual turbines operate in the wakes of upstream turbines. The velocity deficit caused by one or more combinations of wind turbine wakes can lead to significant reductions in power. For instance, Adaramola & Krogstad [1] found a 20%–46% reduction in power output for individual turbines depending on local environment and wind farm layout. Although power losses can be reduced through careful layout planning, the total power loss is still between 10% and 20% compared to an ideal case where every turbine is in the freestream [2,3]. In addition to velocity deficit, the high degree of velocity fluctuations present in the wake causes periodic aerodynamic loading on the blades of downstream turbines, leading to shorter lifespans and higher maintenance costs [3]. Vermeer et al. [4] published an extensive review of available experimental and numerical studies of wind turbine wake structures, and highlighted the need for systematic investigations into the wake structures behind individual wind turbine and wind farms, especially in the near-field wake region.

Adding to the complexity of wind turbine wakes is the fact that wind turbines operate within the atmospheric boundary layer (ABL) where significant shear and freestream turbulence (FST) exist. Modern wind turbines can have rotor diameters around 120 m, and with a tower height of around 100 m, this means that rotors can cover a height from 40 m to 160 m, spanning a non-negligible portion of the ABL, which has thickness on the order of hundreds of meters [5]. The shear flow profile is often parameterized for wind turbine applications as a power-law of the form,

$$\frac{U(z)}{U_r} = \left(\frac{z}{z_r}\right)^{\alpha}, \tag{1}$$

where z is the vertical direction and $U(z)$ is the freestream velocity profile in the wall-normal direction (as a function of z). The subscript r denotes a reference location where U_r and z_r are measured [6]. For a neutrally buoyant atmospheric boundary layer $\alpha \approx 0.143$, and for uniform flow $\alpha = 0$. In the real-world, however, there are significant variations in shear profiles. Wagner et al. [7] classified 2340 independent atmospheric shear measurements into 173 different profiles, and Wagner et al. [6] found that 396 out of

* Corresponding author.
E-mail addresses: leon.li@ntnu.no (L. Li), jason.hearst@ntnu.no (R.J. Hearst).

https://doi.org/10.1016/j.renene.2019.12.049

907, or 44% of their real-world shear profiles at their measurement station could not be adequately described by Equation (1). Furthermore, Dimitrov et al. [8] showed that α has dependencies on both mean wind speed and turbulence intensity, and can range from −0.20 to 0.36. The turbulence intensity experienced by wind turbines also has a wide range of values due to different surface roughness, upstream terrain obstacles and natural oscillations in the atmospheric winds. The survey by Mücke et al. [9] found that turbulence intensity measured from 50 m to 150 m at GROWIAN was typically between 5% and 15%, with gusts reaching up to more than 40%. The high variance in turbulence can have significant impact on wind turbine operations. Milan et al. [10] found that a wind farm's power output can vary by as much as 50% in a time-span of only 2 min, with extreme power changes up to 15 standard deviations occurring on the order of seconds. Therefore, it is evident that most real turbulent shear flows cannot be adequately described by a single or even a few profiles, and thus there is a need to determine the impact of shear and turbulence intensity on a wind turbine in general.

In order to account for the variation in local velocity across the swept area of a wind turbine, Wagner et al. [7] developed a discretized formulation of an equivalent velocity to replace the hub centreline velocity often used in wind turbine power calculations. The equivalent velocity is of the form

$$U_{\mathrm{eq}} = \left[\frac{1}{A}\left(\sum_i \overline{U_i^3} A_i\right)\right]^{1/3}, \tag{2}$$

where A is the frontal swept area of the wind turbine, and the subscript i denotes discretized segments across the span of the rotor. Both U_i and A_i are functions of z. Choukulkar et al. [11] expanded this expression to include the influence from freestream turbulence intensity and yaw angle, via

$$U_{\mathrm{eq,turb}} = \left\{\frac{1}{A}\sum_i \overline{U_i^3}\left[1+3\left(\frac{u_i'}{\overline{U_i}}\right)^2\right]\left[1-\frac{\overline{\phi_i^2}}{2}-\frac{\phi_i'^2}{2}\right]^3 A_i\right\}^{1/3}, \tag{3}$$

where u'_i is the velocity fluctuation, φ_i is the incoming wind angle, and φ'_i is the wind angle fluctuation. It can be seen that an increase in velocity fluctuation will increase the U_{eq} for the same mean velocity profile.

Several methodologies have been used to generate turbulent shear flows in a laboratory setting. The simplest method is augmenting the naturally developing boundary layer on the walls with a series of spires. Using this technique, Counihan [12,13] was able to reproduce both a neutral atmospheric boundary layer and an urban boundary layer with $\alpha = 0.28$, with average turbulence intensities around 7.5%. A more recent effort by Vanderwel & Tavoularis [14] to generate homogeneous turbulent shear flow used a combination of a shear generator and a flow straightener. The main drawback of these passive techniques is that they can only cover a limited range of the parameter space that describes a realistic turbulence shear flow, and each setup needs to be specifically tailored to meet a single set of parameters. On the effects of freestream turbulence alone, it has been shown that an increased freestream turbulence level reduces wake width due to the increased transport of momentum from the freestream into the wake [15]. However this effect was only observed for regions more than two rotor diameters downstream. The same observation was made by Hattori et al. [16]. Both of these studies used passive grids to generate freestream turbulence; Medici & Alfredsson [15] compared clean flow to one grid turbulence flow at 4.5% FST, while Hattori et al. [16] used 4 different grids to generate FST ranging from 7.5% to 15%. However these studies were also limited in their ability to explore a wider parameter space as a result of their physical setup. In particular, most passive set-ups have focused on reproducing the neutral stability conditions, because this is a reasonably well-understood theoretical state. However, the field measurements of Wagner et al. [7] did not identify this profile as one of the 10 most likely to occur at their site, and therefore it may not actually be particularly representative of the flows encountered by wind turbines. Overall, using passive flow modification devices has been successful in producing a few basic examples of turbulent shear flows, but they are not well suited to expand this parameter space or separate shear from turbulence profiles.

The advent of active grids has opened a new frontier of possibilities in producing a wide range of tailored turbulent flow with a single setup. First popularized by the seminal work of Makita [17], active grids have since been used in a variety of studies. The general operational principle of these devices is that a grid of square wings can be actuated in a controlled sequence to augment the turbulence produced downstream; for example, controlled patterns to recreate time-series of field measurements, or random motions that produce turbulence that is approximately homogeneous in transverse planes and locally isotropic. Recently, several studies have used active grids to generate highly-tailored inflow conditions for wind turbine or ABL experiments. Knebel et al. [18] generated highly intermittent turbulent wind fields through the use of an active grid in a wind tunnel, and Neunaber et al. [19] studied the effects of continuous and intermittent turbulent inflows on wake development behind a wind turbine. Shen & Warhaft [20] were the first to incorporate an active grid in a shear flow study by inserting variable solidity screens downstream of the active grid, and later Cekli & van de Water [21] were the first to attempt to create shear flow with an active grid alone. This was accomplished by setting the initial positions of the wings to different angles, and then having each set of wings flap about this angle. Schottler et al. [22] set their active wings to two sets of static positions to create a classical and an inverted shear profile. Rockel et al. [23] used an active grid in passive and active modes to create inflow conditions with low and high turbulence intensities and found that with increasing turbulence intensity, the vortex shedding from the blade tips are destabilized. Talavera & Shu [24] created three different simulations of turbulent ABLs using a single active grid setup, with turbulence intensities ranging from 3% to 17.4% at the centre of the turbine. However they did not explore the possibility of creating different shear velocity profiles in their study. Hearst & Ganapathisubramani [25] were the first to decouple shear and turbulence intensity. This was accomplished by using one plane of wings to create different porosity, and thus shear flow, and the other plane of wings to produce different turbulence intensity levels. The method for producing shear differs slightly between Cekli & van de Water [21] and Hearst & Ganapathisubramani [25], in that Hearst & Ganapathisubramani [25] initially set all the wings parallel to the flow, and oscillated each set of wings by different amplitudes. The work by Hearst & Ganapathisubramani [25] offered unprecedented freedom to explore a large number of parameters for turbulent shear flows with one single setup, and forms the basis for the present study.

2. Experimental procedure

The present experiments were carried out in the University of Southampton's open loop suction wind tunnel, which has a test section measuring 0.9 m × 0.6 m × 4.5 m. The freestream turbulence intensity is approximately 0.2% in the empty tunnel.

The same active grid used by Hearst & Ganapathisubramani [25] and Dogan et al. [26] was used here. The design of the grid is similar to those found in past studies, such as Makita [17] and Hearst &

Lavoie [27]. The grid consists of 11 × 7 rods in a bi-planar layout. Each rod has a diameter of 10 mm. The mesh length $M = 81$ mm is defined as the spacing between the rods. The rods are controlled independently by a computer via 18 daisy-chained stepper motors. Mounted to the rods are square wings with sides measuring 55.86 mm. Solid square wings were used, resulting in a maximum blockage of 100% when all wings are perpendicular to the flow, however, this is never allowed to happen. The active grid was mounted at the inlet of the test section, just after the contraction.

The model wind turbine, detailed in Fig. 1, was designed to achieve a blockage ratio below 7%, including its swept area and the exposed cross-sectional area of the tower. It was driven at fixed, predetermined velocities by a Kollmorgan AKM33H servo motor that was mounted below the test section, coupled to a Futek FSH01987 torque sensor that is accurate to ±20 mNm. A 5 mm diameter driveshaft runs through the tower and is coupled to the horizontal turbine shaft via a built-in right-angle bevel gearbox. A series of ball-bearings at critical locations prevent wobbling and the transmission of vibrations into the system. The tower was built in the form of a NACA0020 airfoil to minimise wake interference with measurements downstream, and is tapered towards the top to increase the surface area in contact with the base plate, which is in turn bolted onto the wind tunnel floor. The profile of the tower fairing does not represent the tower of a real wind turbine, but rather is meant to be a low-flow-disturbance sting. Thus, the rig approximately represents a 'floating' turbine positioned in the centre of the tunnel.

A three-blade rotor, 208 mm diameter, was designed based on the NACA4418 airfoil with a uniform chord distribution $c = 20$ mm. The blade twist profile comes from the NREL reference airfoil [28]. It is mounted to the test section floor 3.05 m downstream of the active grid, corresponding to $37.7M$. The specified rotational velocity was $\omega = 15$ Hz for all cases. It has previously been demonstrated that the wakes of motor-driven and flow-driven wind turbines at this scale are comparable [29]. As the rotational velocity of the turbine was actively kept constant by the control system, the torque (τ) could be used to measure the power from $P = \omega\tau$. A decrease in the power of the system represents an increase in energy extraction because the power does not need to be supplied by the servomotor. Setting the hub centreline freestream velocity at 10 m/s gave a tip speed ratio (TSR) $\lambda \equiv \omega R/U_0 \approx 1$, where R is the radius of the rotor assembly. This is the highest TSR that could be achieved without mechanical vibrations becoming a problem. While we understand that this imposed a limitation to the present study, it is of similar magnitude to the typical TSR of 2–14 found in real wind turbines [30] and we present this study as a demonstration of the experimental capabilities of this approach to model testing rather than as a direct comparison to a full-scale rotor.

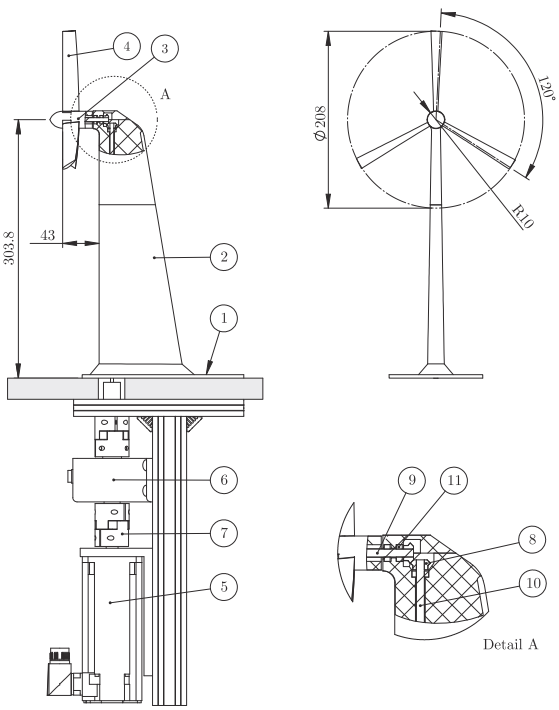

Fig. 1. Model wind turbine design, with side-view on left, front view on the upper-right corner, and a breakout section detailing the bevel gearbox at the bottom right. (1) base plate; (2) tower; (3) hub; (4) blades; (5) motor; (6) torque encoder; (7) coupling; (8) right-angle bevel gearbox; (9) turbine shaft; (10) vertical driveshaft; (11) ball-bearing. Dimensions are in millimetres.

The coordinate system used for this study is identical to the one used by Hearst & Ganapathisubramani [25]; and shown in Fig. 2. The side of the active grid with more degrees-of-freedom was used to create shear flow because it offered greater control for creating different profiles. The z-axis was chosen to coincide with this dimension in order to keep the standard convention of aligning the z-axis with the vertical plane used in atmospheric boundary layer and real wind turbine studies, e.g., Refs. [6,8,9], and [12].

An extended laser sheet upstream and downstream of the wind turbine model was created with two synchronised Litron Nd:YAG lasers (532 nm, 200 mJ per pulse). The laser plane coincides with the hub centreline. Two LaVision ImagerProLX 16 mega-pixel cameras equipped with Sigma DG 50 mm lenses were placed along the streamwise direction. The total field-of-view (FoV) of the two-camera set up was 338 mm wide and 730 mm long. The overlapping region between the FoV from individual cameras is 66 mm long, or about 13% of the length of each camera's FoV. For the laminar uniform flow baseline case, 600 image pairs were acquired, while for all the other test cases 1200 image pairs were acquired at 0.6 Hz.

Vector fields were calculated with DaVis 8.4.0 on central processing units, beginning with a single pass on a coarse grid of 128 pixels × 128 pixels and then down to three passes at a finer grid of 32 pixels × 32 pixels, with a 50% overlap for each pass. Vector field stitching was done post-calculation in MATLAB using a weighted blend of error and linear functions for averaging and smoothing the overlapping regions between the two frames. Fig. 3 shows representative instantaneous flow fields for all the test cases. While the details of these test cases will be discussed in the next section, we would like to highlight some of the qualitative differences observed in Fig. 3. The reference case REF has the most homogeneous incoming flow and the smallest turbulence intensity. Cases 0L and 0H are uniform flows with higher turbulence intensities, and this can be seen through the increasing prominence of randomly distributed high- and low-velocity regions in the incoming flow. The other cases are shear flows, and have distinctly stratified high- and low-velocity regions in the incoming flow, representing velocities below and above the hub centreline velocity, respectively.

3. Incoming flow conditions

A total of seven different incoming flow conditions were generated for this study. They are the same as those in Hearst & Ganapathisubramani [25], where a more detailed description of the flow conditions can be found. A brief summary will be given here.

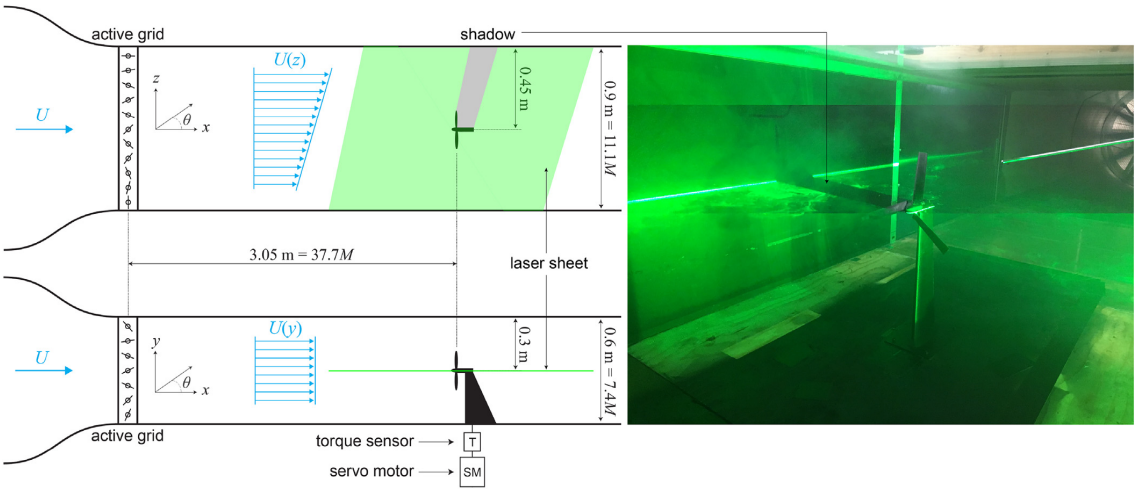

Fig. 2. Schematic of the experimental setup.

Shear was created by oscillating the 11 vertical bars through different angles ranging from 0° to 90°. A small oscillation angle creates a larger apparent porosity, leading to higher local velocity, and vice versa. For this study, three different shear profiles were chosen from the available list in Hearst & Ganapathisubramani [25]. The cases were chosen to represent a variety of turbulence and shear conditions. An additional uniform flow case was added to provide baseline measurements. The shear flow profiles are shown in Fig. 4a, where the incoming flow profile is denoted as U_i. The seven horizontal bars were used to vary the incoming turbulence intensity. The input control parameters were rotational velocity of the wing, rotation duration, and acceleration. The fully random mode of actuation described in Hearst & Lavoie [27] is used here, where each motor is given a sequence of random values of these three control parameters. A measurement was also taken with the active grid removed to obtain a "laminar" flow baseline. The turbulence intensity (u'/U) profiles are shown in Fig. 4b. Fig. 4c and d shows the w-component velocity fluctuation and turbulence isotropy, respectively. The isotropy is comparable to values from other studies that used an active grid to generate freestream turbulence (e.g. Hearst & Lavoie [27]).

A naming convention was developed for the seven incoming flow fields. The baseline case with no grid is denoted as "REF" for reference, and all others were assigned two-character names. The first is a number denoting shear profile shape, and the second is a letter denoting u'/U level. For shear profile shapes, 0 denotes uniform flow, 1 & 2 denote power law profiles with increasing shear gradient (i.e. 2M would have a greater gradient than 1M), and 3 denotes non-power-law profiles. For turbulence intensity the letters L, M, and H are used to denote low, medium and high intensities. Low intensity is defined as less than 5%, medium intensity is defined as between 5% and 13%, and high intensity is defined as 13% or higher.

The freestream mean velocity (U_i) and u'/U profiles shown in Fig. 4 are all computed from the calculated PIV vector fields. The incoming fields are calculated for the range $-0.8 \leq x/D \leq -0.7$. This location corresponds to $35.5M$ downstream from the active grid, which is within the region where grid-generated turbulence is normally considered homogeneous [27,31]. The homogeneity at the turbine location was presented by Hearst & Ganapathisubramani [25] and shown to be strong for a region that exceeds the rotor area. Table 1 lists the α values and turbulence intensities at hub height for all cases. The parameter α is calculated through the same method as described in Hearst & Ganapathisubramani [25]. The minor differences between the incoming flow parameters shown here and in [25] can be attributed to the difference in the PIV of the present measurements compared to the earlier hot-wire measurements.

4. Mean velocity fields

Fig. 5a shows the wake velocity profiles at $x/D =$ 1, 1.5, & 2 normalized by the incoming hub centreline velocity U_0. This is a measure of the absolute velocity in the wake region. The incoming profiles at $x/D = -0.7$ are superimposed for comparison with the wake velocity gradient. The absolute wake velocity profiles are symmetric about the hub for the uniform flow cases, as expected. However, for the shear flows, the distributions are skewed by the incoming flow and thus asymmetric. It can also be seen in Fig. 5a that the wake core velocity is approximately the same for all cases. These two effects combine to create a wake velocity gradient that increases with incoming velocity gradient on the high-velocity side, and this wake velocity gradient is greater than that of the incoming flow. While this could imply that subsequent turbines downstream could potentially experience an incoming flow with increased shear, this study is limited to the near-field wake behaviour and further investigations are required to examine wake recovery farther downstream.

It is postulated that this asymmetry in the absolute wake velocity profiles for shear flows is due to the superposition of the incoming shear with the wake. Fig. 5b shows the relative wake velocity profiles at the same downstream locations as in Fig. 5a. These profiles are normalized by having the incoming velocity profiles removed, i.e., $(U - U_i)/U_0$. The relative wake velocity profiles are symmetric about the hub for all test cases, suggesting that the asymmetry found in the absolute wake profiles is indeed caused by the incoming sheared flow. This has significance for modelling the averaged velocity field in the near-wake region, in that the field can be modelled as a linear addition of a wake profile from a uniform flow, and an incoming shear flow, as suggested by

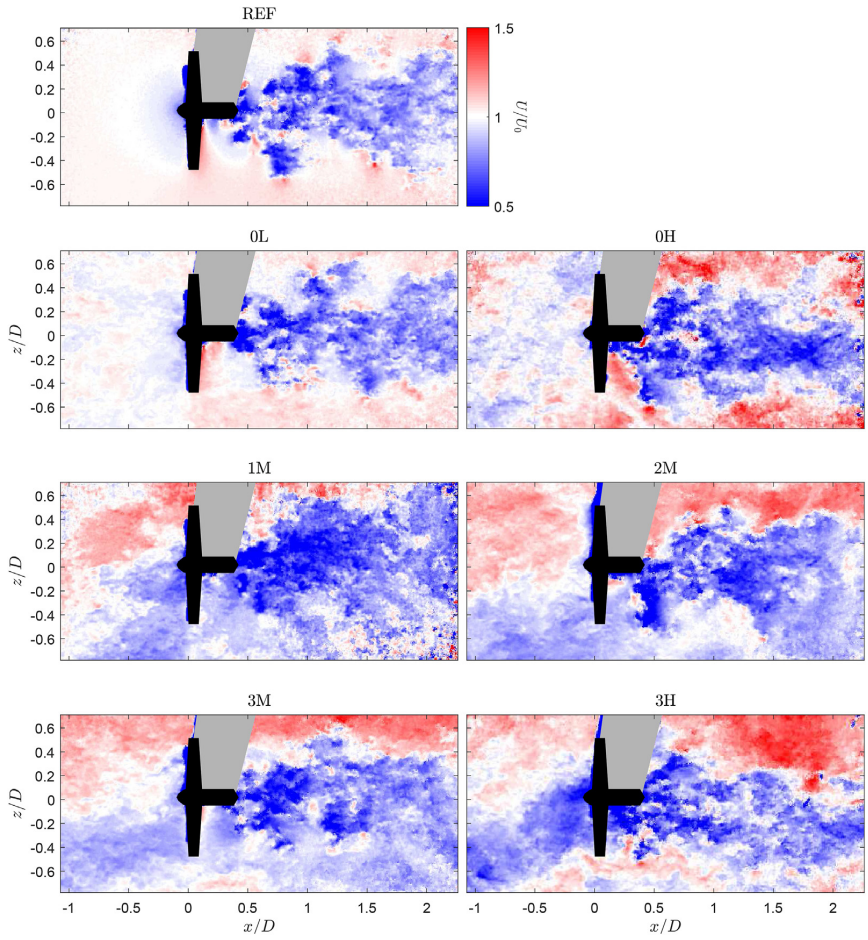

Fig. 3. Representative instantaneous normalized U velocity field for all seven test cases.

Chamorro & Porté-Agel [32]. Fig. 5b also shows reasonable collapse between profiles for a given downstream location, indicating that the macroscopic wake behaviour does not vary significantly with respect to the incoming flow. The two cases with the lowest incoming turbulence intensity, REF and 0L, have wake profiles that are less smooth. It can be seen in Fig. 5b that these two cases have additional relative velocity deficit "bumps" between $0.3 < |z/D| < 0.5$ compared to the other cases. The locations of these bumps corresponds to strong vortex streaks downstream of the rotor tips, which are absent from the higher turbulence intensity cases (Fig. 6). This is expected as higher turbulence intensity promotes mixing in the wake [33], thus producing a wake profile without the additional velocity deficit peaks associated with the rotor tips. The location of the rotor tip vortex streak can be more readily seen in Fig. 7, where the cross-sectional averaged vorticity is shown for $x/D = 1$, 1.5, and 2. The rotor tip vortex streaks for cases REF and 0L are centred at $z/D \sim \pm 0.5$ and are pronounced compared to the other cases. Cases REF and 0L also show a slightly higher velocity deficit at $x/D = 2$ compared with the rest. Again this is expected as higher incoming turbulence level transports more flow from the free-stream into the wake, promoting wake recovery [15]. This is only observed at $x/D = 2$, which is also consistent with the findings of Medici & Alfredsson [15], in that the near-field wake is not significantly affected by different incoming turbulence levels for region $x/D < 2$.

Overall, the absolute and relative wake velocity profiles show that in the presence of a shear flow, the average wake velocity profiles can be linearly decomposed into a symmetric component associated with the wake in a uniform flow, and an asymmetric component that is the incoming shear profile. This is significant because it shows that wind turbine wakes are relatively robust to different incoming turbulent shear flows, and the interactions between the turbine and the different flow conditions produce no observable non-linear effects on the average velocity field in the near-wake. This assertion is more rigorously tested and validated by the present measurements than in previous studies that investigated only a pair of test cases. We would like to note that this observation only applies to the average velocity field, and not the higher-order turbulence statistics.

To further examine the robustness of the near-field relative wake profiles to the different incoming flows, the wake geometries are extracted from the velocity fields for all the test cases and

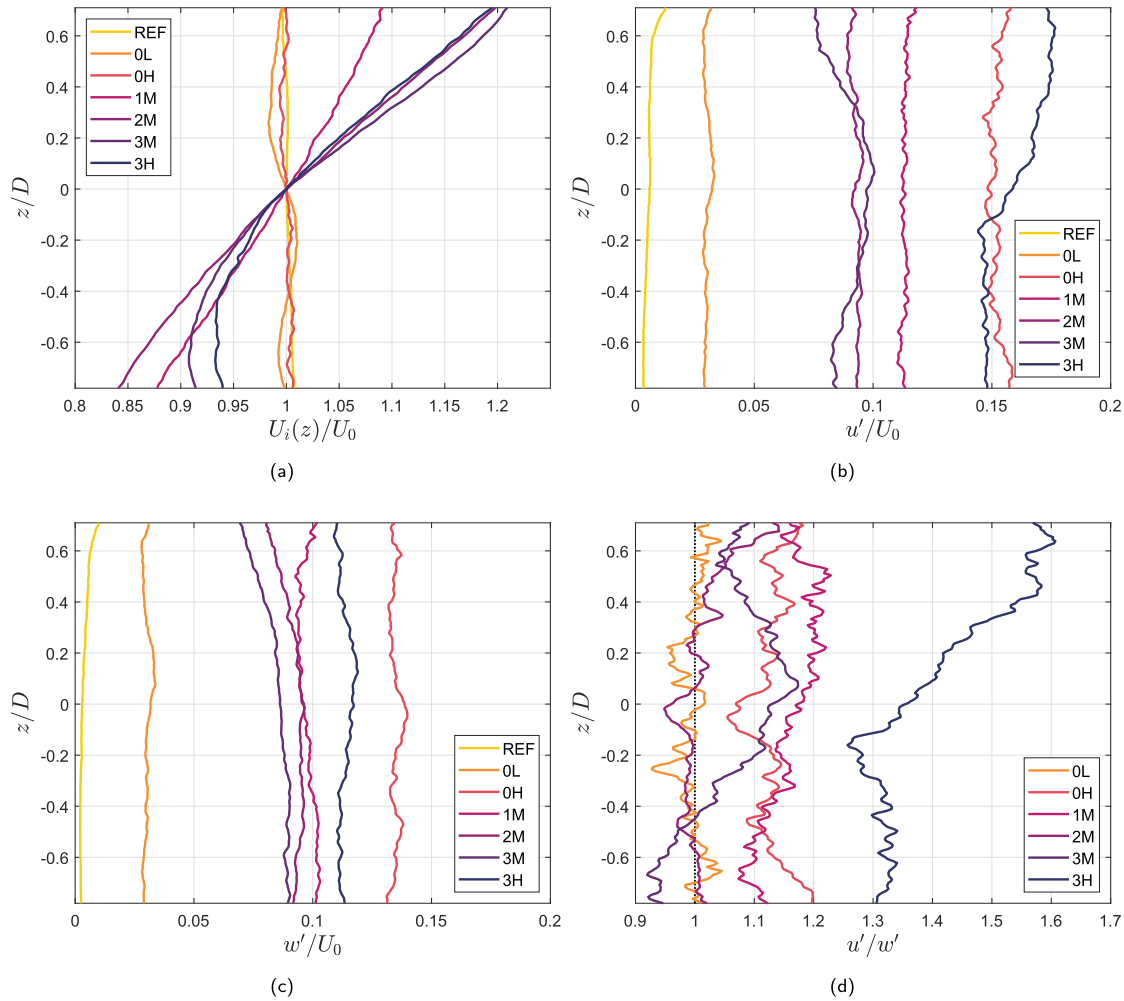

Fig. 4. Flow profiles of a) normalized mean streamwise velocity U_i/U_0, b) u'$/U_0$, and c) w'$/U_0$ for all cases; d) u'$/$w' for all cases with active grid installed. z-axis is normalized by rotor diameter $D = 0.21$ m.

Table 1
Summary of incoming flow characteristics at $x/D = -0.7$.

Mode	α	u'$_0/U_0$ [%]	U_{eq}/U_0	$U_{eq,turb}/U_0$
REF	0	0.6	1.000	1.000
0L	0	3.2	0.997	0.998
0H	0	14.8	0.999	1.021
1M	0.17	11.2	1.001	1.013
2M	0.29	9.2	1.008	1.017
3M	0.29	9.7	1.015	1.024
3H	0.24	15.8	1.012	1.036

shown in Fig. 8a. The wake boundary is calculated by subtracting the freestream mean velocity profile from the overall velocity field and tracing $(U - U_i)/U_0 = 0$. The wake centre is defined as the local minimum in the $(U - U_i)/U_0$ field in the region along the hub centre. It can be seen that the wake boundaries for all cases stay relatively symmetrical about the hub, with no indication of deflection. The different incoming shear profiles and turbulence intensities appear to have no significant impact on the behaviour of the wake boundaries within the investigated region, when the wake is defined relative to the incoming flow. The same is true of the wake centrelines.

The hub velocity contour line is defined as the trace where $(U - U_0)/U_0 = 0$, or where the velocity in the field is equal to the hub centreline velocity U_0. Fig. 8b shows the contour lines for all the test cases. For uniform flow conditions, these contour lines coincide with the wake boundary and originate from the rotor blade tips. In sheared flows, they are deflected toward the high-velocity side of the incoming shear flow and continue in the wake. Compared to the uniform flow cases, shear flows force the hub velocity contour lines from the blade tip toward the hub, and this forcing increases with local shear gradient. This phenomenon may result from the higher momentum carried by the high-velocity flow in the cases with more shear overcoming the radial flow induced by the rotor. The z/D location of the contour lines in the near-field wake can also be

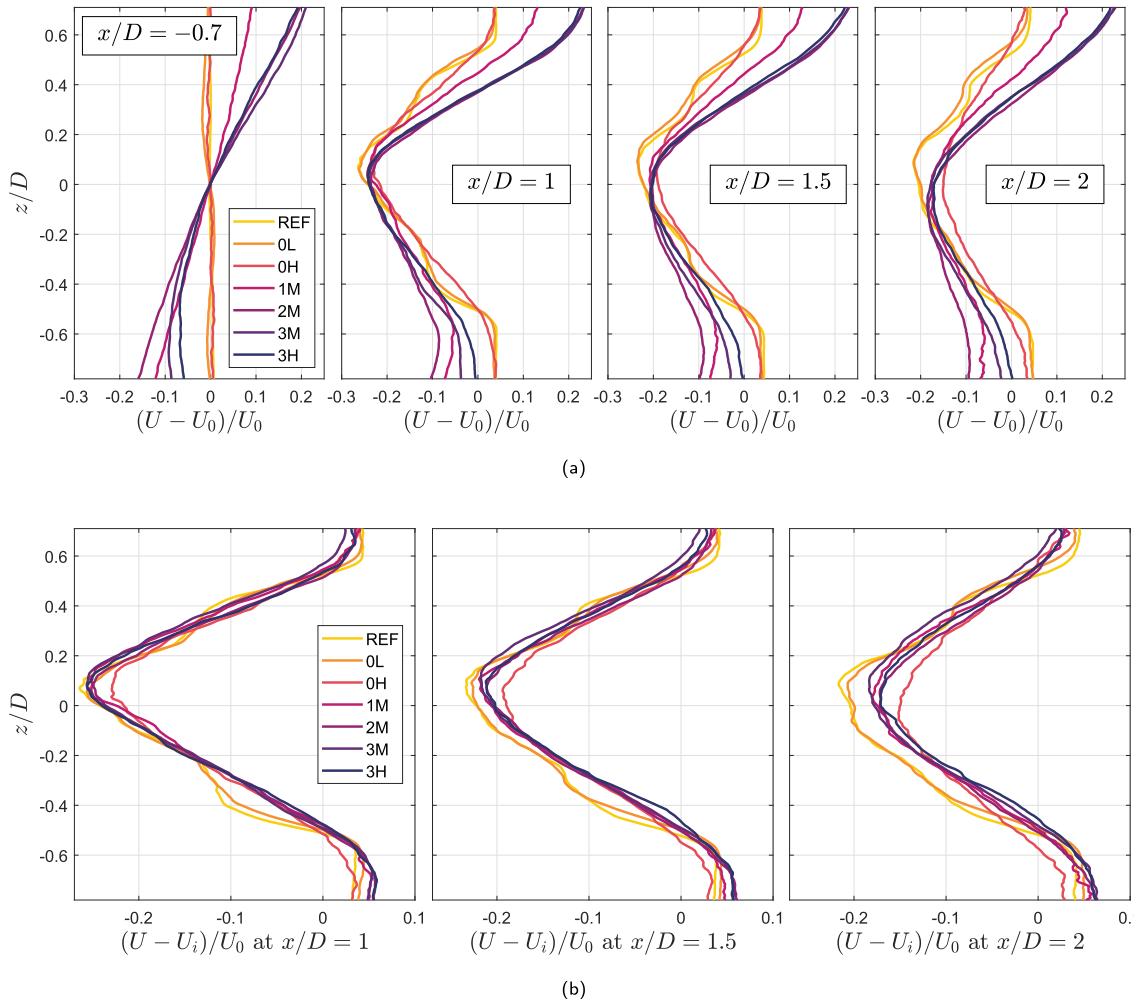

Fig. 5. Two representations of wake profiles at $x/D = 1$, 1.5, & 2 for all cases, where a) is normalized with respect to hub centreline velocity, and b) has their respective freestream velocity profiles removed and normalized by hub centreline velocity. Incoming mean velocity profile is also shown in a), centred at $x/D = -0.7$.

used as a measure of the severity of shear in the absolute wake velocity profile on the high-velocity side. As U_0 is similar for all test cases ($\sim 10 \text{ms}^{-1}$) and it is shown in Fig. 5a that all cases have similar minimum velocity deficit in the wake, the contour lines mark the z/D location where the velocity field must return to U_0. Thus, the closer the contour lines are to the hub, the greater the velocity gradient in the wake must be.

5. Turbulence statistics

In Fig. 5a, it can be seen that the absolute wake velocity gradient on the high-velocity side in a shear flow is higher than the uniform flow cases, while the opposite is true on the low-velocity side. This difference in the shear gradient has an impact on the turbulence statistics distributions in the near-field wake. Fig. 9 shows the *u*', *w*', and turbulence isotropy (*u*'/*w*') profiles in the wake normalized by the hub centreline velocity U_0, at streamwise locations $x/D = 1$, 1.5, & 2. Case 1M at $x/D = 2$ is not shown in these profiles because of data noise contamination for $z/D \lesssim -0.4$, which increased the calculated values for *u*' and *w*', and therefore is not representative of the actual distribution profile. The *u*' fluctuations for the uniform flow cases show two peaks in its spanwise wake distribution, one at each of the blade tips. The prominence of these peaks decreases downstream. This is expected as vortex streaks trailing the blade tips lead to higher production of turbulence [32]. The turbulence intensity reached in the wake for case 0H is comparable to that of the incoming flow. In the shear flow cases, velocity fluctuations are not evenly distributed in the spanwise direction. Instead they are biased toward the high-velocity side of the shear flow. This behaviour is consistent with the observation of Chamorro & Porté-Agel [32]. This observation suggests that higher shear leads to higher velocity fluctuations, or turbulence intensity, in the wake.

The *w*' fluctuations for cases REF and 0L show 4 distinct peaks at $x/D = 1$, associated with vortex shedding from the blade tips and root. Case 0H at the same location does not show these 4 peaks in *w*' distribution, suggesting that the higher freestream turbulence

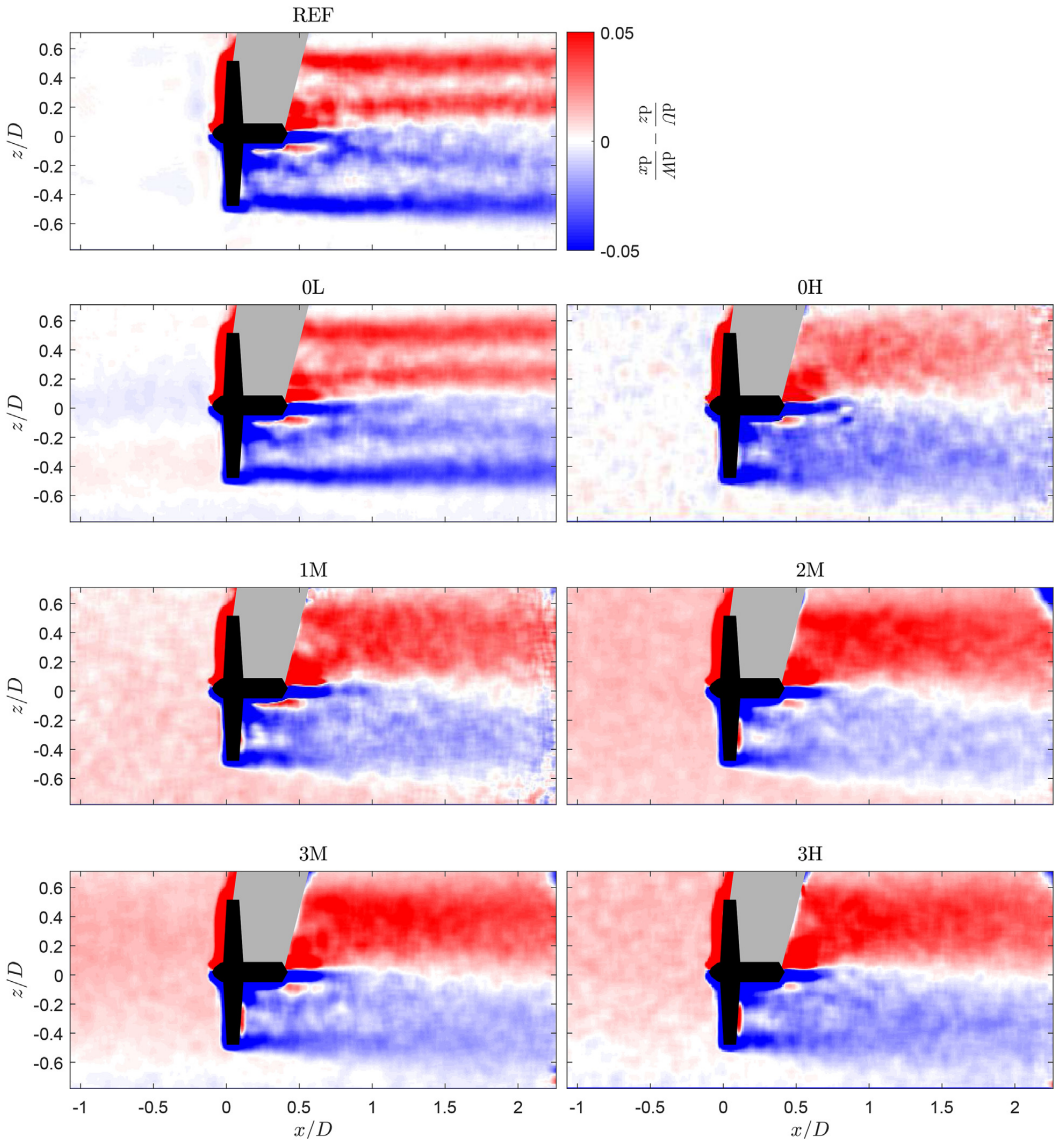

Fig. 6. Averaged vorticity fields for all 7 test cases.

level was sufficient to mix w' into a more uniform distribution. The two peaks associated with the root decay faster than those associated with the tip as the flow progresses downstream in the wake, and they largely disappear by $x/D = 2$, leaving only the two blade tip peaks present in the w' distribution. For the shear flow cases, w' distribution, similar to u', is biased toward the high-velocity side.

Fig. 9c shows the u'/w' profiles in the wake. For cases REF and 0L, there are two prominent peaks associated with the blade tips where $u'/w' > 1$. The flow is more isotropic near the hub ($u'/w' \approx 1$). These two peaks decrease in size downstream, and at $x/D = 2$ are no longer noticeable, and the whole wake region becomes isotropic. This phenomenon is only observed for cases REF and 0L, not 0H, suggesting that increased incoming turbulence level impacts the wake's turbulence isotropy. For case 0H, the wake turbulence is only near isotropic within a narrow region centred about the hub, and anisotropy increases to about the incoming flow level toward the blade tips. At $x/D = 2$, the flow is no longer near isotropic even at the hub centreline. Another interesting phenomenon for cases REF and 0L is that $u'/w' < 1$ just outside of the turbine radius. This only appears for these two cases, and could be due to the blade tip induced radial velocity component promoting w' fluctuation as it "sheds" from the rotor, and increased incoming turbulence level suppresses this action. For the shear flows, the wake turbulence isotropy is asymmetric. The flow is near isotropic

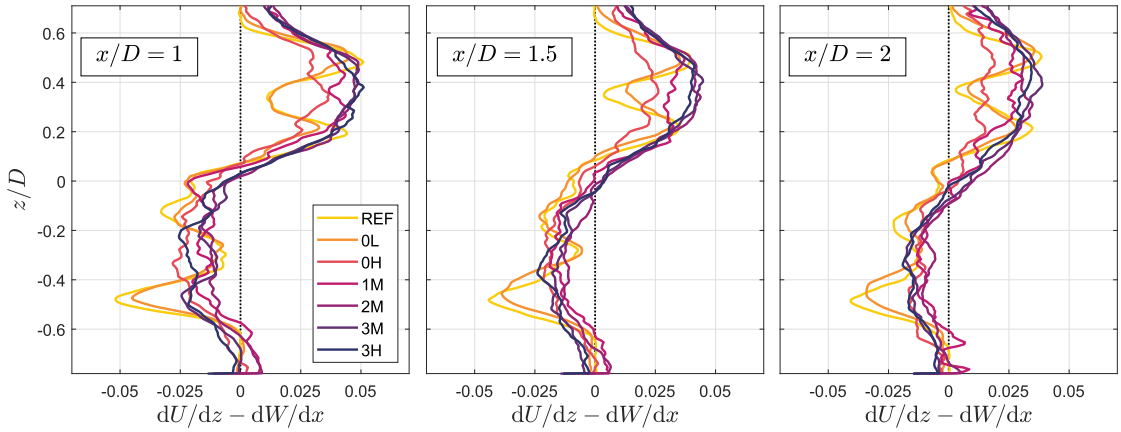

Fig. 7. Vorticity wake profiles at $x/D = 1$, 1.5, & 2 for all cases.

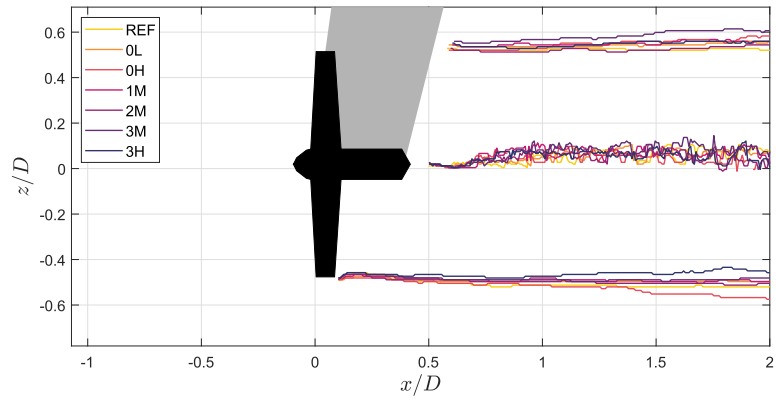

(a)

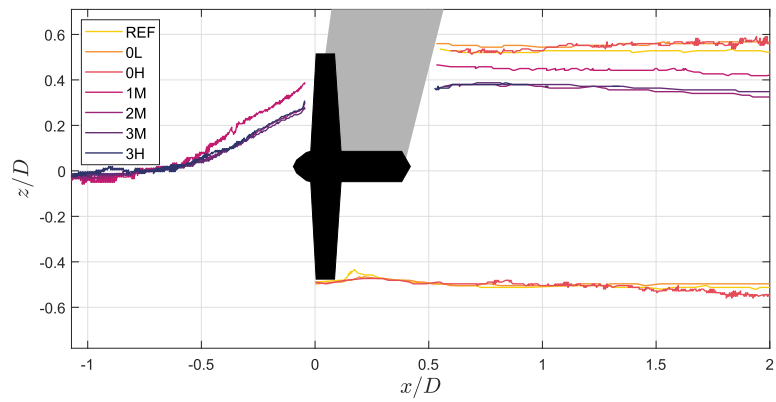

(b)

Fig. 8. a) Wake centreline and boundary of all test cases. b) Hub centreline velocity contour for all test cases.

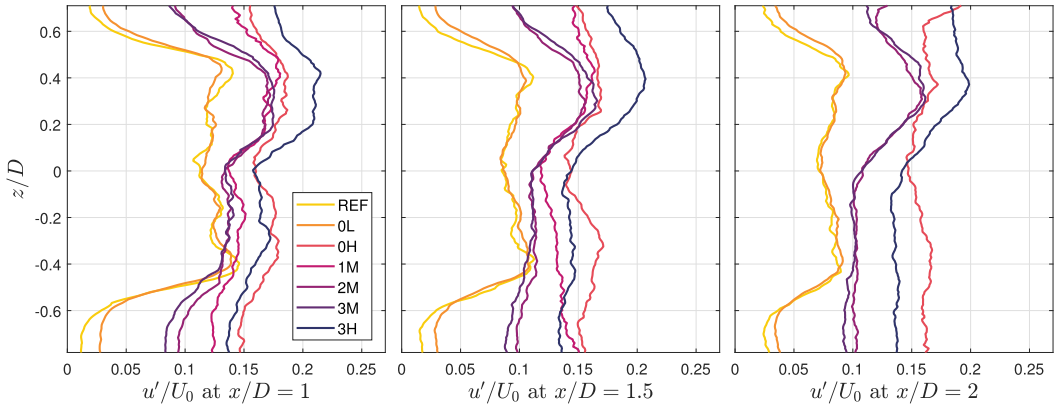

(a)

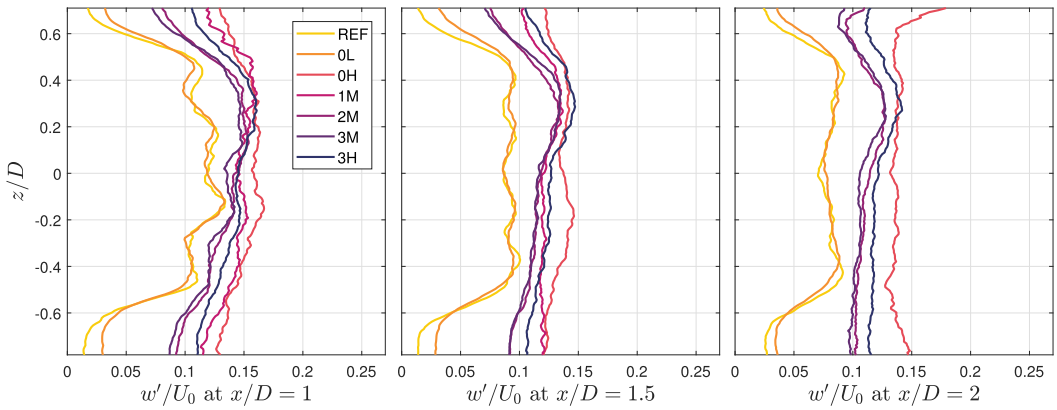

(b)

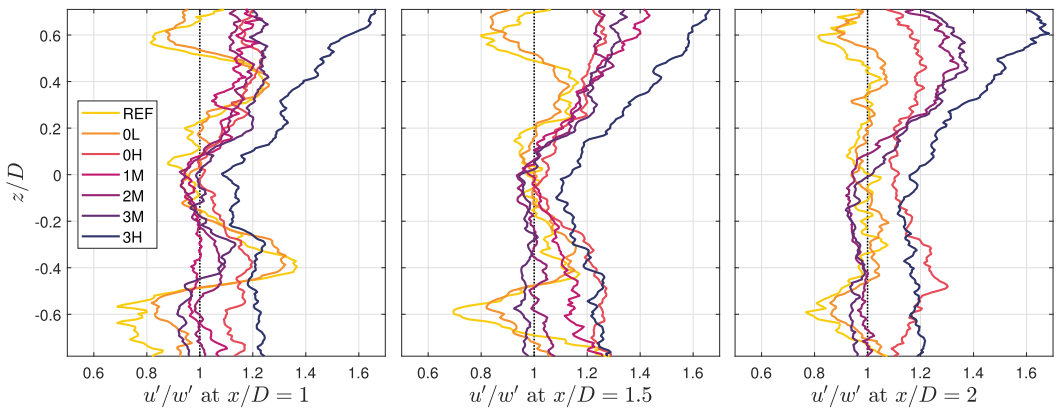

(c)

Fig. 9. a) u'/U wake profiles, b) w'/U wake profiles, and c) turbulence isotropy (u'/w') at x/D = 1, 1.5, & 2 for all cases.

on the low-velocity half of the flow, and more anisotropic on the high-velocity side. This suggests that on top of promoting velocity fluctuations, high shear in the wake also promotes streamwise fluctuations over spanwise. Overall, it appears that both u'_0/U_0 and the shear profile affect the near-wake isotropy, with u'_0/U_0 having more local effects near the hub and blade tips, and the shear profile having a global effect on the symmetry of the isotropy distribution.

The bias of velocity fluctuation toward the high-velocity side in shear flow cases can be seen more prominently in the Reynolds shear stress $-\overline{u'w'}$ distribution shown in Fig. 10. In the uniform flow cases REF, 0L, and 0H, the Reynolds shear stress is symmetric about the hub centreline, with a positive peak located roughly at $z/D = 0.25$, half the distance between the blade tip and the hub centre, and a negative peak at $z/D = -0.25$. The magnitude of the peaks in Reynolds shear stress increases with increasing u'/U. For shear flow cases, the magnitude for the positive peaks on the high-velocity side is significantly higher than that of the negative peaks on the low-velocity side, akin to the asymmetry in the velocity fluctuations. Increasing u'_0/U_0 also increases the local peak magnitudes in Reynolds shear stress distribution for shear flows. The difference diminishes as the flow moves downstream. The different shear levels do not appear to significantly impact the shape of the distribution aside from asymmetry, suggesting that u'_0/U_0 has a greater impact on the Reynolds shear stress for both uniform and shear flows. However, the shear enhances the positive peak while suppressing the negative peak. The degree of reduction in the negative peak resulting from the shear is greater than the degree of enhancement of the positive peak. The Reynolds shear stress has a significant impact on the cross-terms in the production of the total turbulent kinetic energy budget. The combined effects of large values of $-\overline{u'w'}$ and $\partial U/\partial z$ in the high-velocity region in the near wake is expected to have a large influence on the distribution of the turbulent kinetic energy production.

The production $\Sigma u'_i u'_j \frac{dU_i}{dx_j}$ was examined term-by-term to determine the contribution of each component. The term $-\overline{u'w'}\frac{\partial W}{\partial x}$ was found to be negligible compared to the other three terms, and therefore was not included in the sum. This is due to the relatively small variations in W with respect to x in the wake. Note that we only have four components in total because these are 2D flow data. Fig. 11 reveals that there is a higher peak in turbulence production on the high-velocity side for shear flow cases. In particular, case 1M shows a double-peak structure at $x/D = 1.5$ on the high-velocity side, while the other shear cases all show a single peak. At $x/D = 2$, the double-peak in 1M have blended into one. The presence and later mixing of the two peaks suggests an increase in turbulence production in the streamwise direction for case 1M, whereas the presence of a single peak throughout the wake for the other shear flow cases suggests that turbulence production was already high enough to promote mixing into one region, which is consistent with the findings of Rockel et al. [23]. This observation suggests that turbulence production distribution is affected more by shear profile than u'/U in the near-field wake, as case 1M differs most significantly from the other shear cases in local velocity gradient. Turbulence intensity, however, does have an impact on the level of turbulence production, as case 3H shows higher level than cases 2M and 3M.

Fig. 7 shows the vorticity distribution in the wake. As mentioned in the previous section, the REF and 0L cases have a double-peak structure on either side of the hub, associated with vortex streams from the blade tip and the hub. In case 0H these two peaks are blended into one, centred around the middle of the blades. In the shear flow cases, the magnitude of vorticity peak on the high-velocity side is again greater than that on the low-velocity side, consistent with the other observation of biased turbulence production. This would also suggest that vorticity in the near-field wake is more significantly affected by shear than freestream turbulence intensity. It is interesting to note that u'/U has no significant impact on vorticity level. In Fig. 6, aside from showing vortex stream blending due to increased u'/U, it also shows the promotion of vorticity magnitude on the high-velocity side.

The formulations of the equivalent velocity U_{eq} of Wagner et al. [7] (Eq. (2)) and $U_{eq,turb}$ of Choukulkar et al. [11] (Eq. (3)) differ in that Choukulkar et al. [11] consider the effects of u'_0/U_0 and wind angle. Adapting the U_{eq} formulations of both authors to the near wake region can give another measure of how shear profiles and turbulence intensity levels impact the available kinetic energy for the downstream turbine. Fig. 12 shows the percentage difference between U_{eq} and $U_{eq,turb}$ for all the cases. Choukulkar et al. [11]'s formulation is consistently higher than that of Wagner et al. [7] because velocity fluctuations are considered. It thus appears that u'_0/U_0 has a greater impact on the available energy than the shear profile as the data points are roughly separated into three groups of differing u'_0/U_0, regardless of the shear profile. The two cases with the highest u'_0/U_0, 0H and 3H, show an increase in the equivalent wind speed by $\sim 4\%$ at $x/D = 1$, and by $\sim 3\%$ at $x/D = 2$.

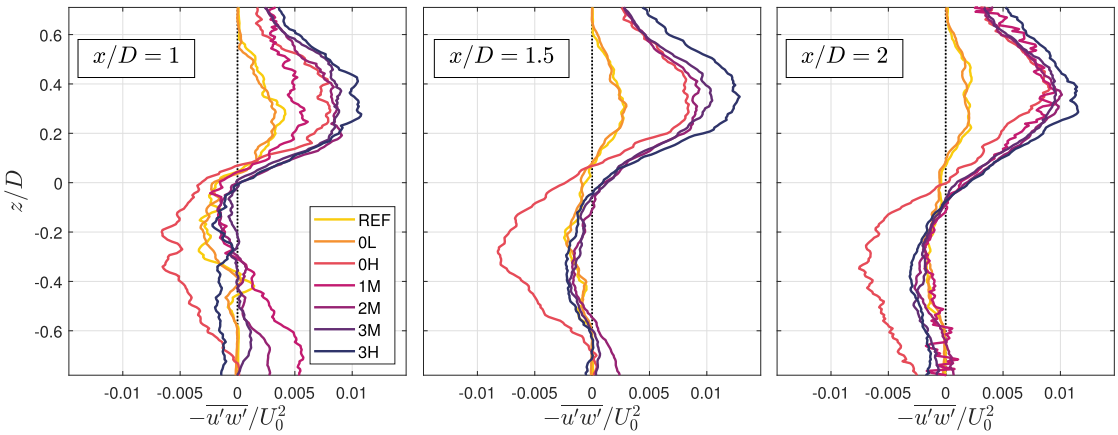

Fig. 10. Non-dimensional Reynolds shear stress wake profiles at $x/D = 1$, 1.5, & 2 for all cases.

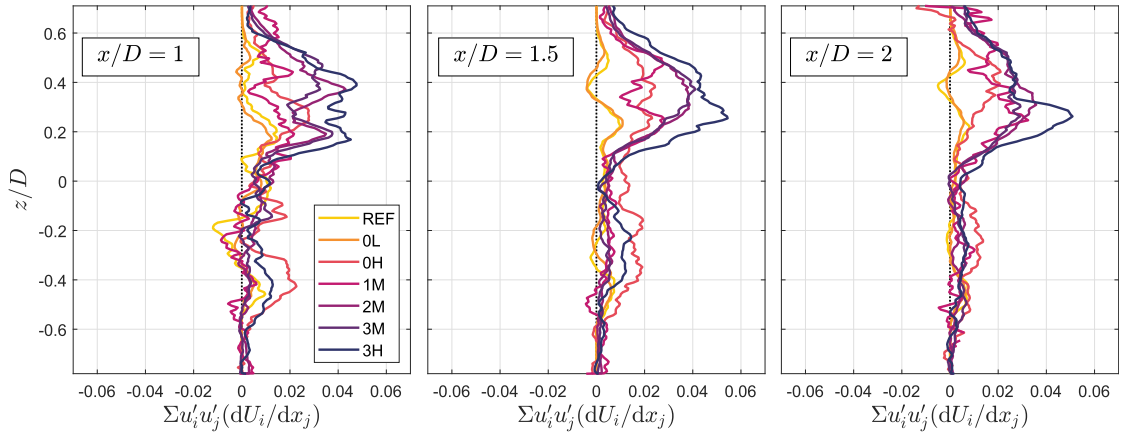

Fig. 11. Turbulence production wake profiles at $x/D = 1$, 1.5, & 2 for all cases.

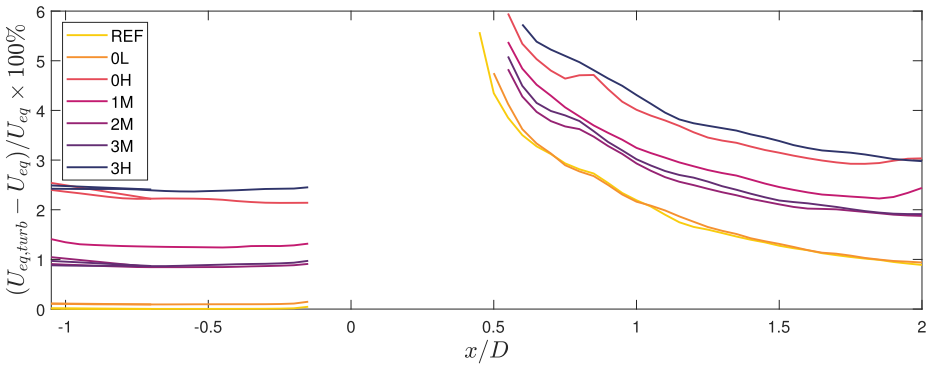

Fig. 12. Percentage differences between U_{eq} and $U_{eq.turb}$ [7].'s formulation is used for U_{eq} and [11]'s formulation is used for $U_{eq.turb}$; differences are shown for upstream and downstream of the turbine for all cases.

The above observation is interesting when it is compared to the torque, and thus power, measurements performed here. In general, the difference in mean power (P) between all cases investigated does not exceed the uncertainty of the sensor. Despite the increased 'relative' energy between the two estimates for the equivalent wind speed presented in Fig. 12, their actual values (reported in Table 1) do not vary significantly between test cases. For instance, the peak-to-peak variation between all test cases is 1.8% for U_{eq} and 3.8% for $U_{eq.turb}$, respectively, where the latter considers the effect of the turbulence intensity in addition to the shear. Given such a small change to the equivalent wind speed, it is perhaps not surprising that the mean power did not change significantly. One must also consider that the shears investigated here are significant, some on the order of 30% change in U across the rotor diameter. The fact that this does not significantly change the equivalent wind estimates or the mean power for a fixed U_0 suggests that it is the absolute value of the hub velocity rather than the meticulous integration of shear that dominates the strong collapse presented in, for instance, Wagner et al. [6], over the entire wind turbine operational range. What is interesting in the present results though is that the standard deviation of the power (p') calculated for frequencies below the rotational rate of the turbine appears to have a linear dependence on the incoming turbulence intensity as illustrated in Fig. 13. Thus, while there are no obvious mean changes to the power extraction, the turbulence intensity certainly impacts the power

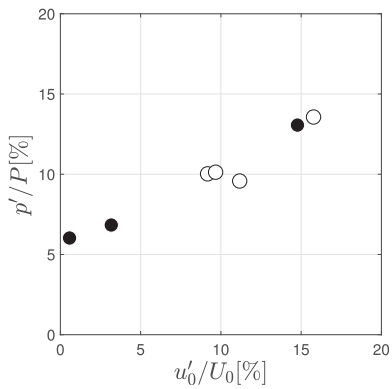

Fig. 13. Variation of power fluctuations measured on the turbine rotor compared to the incoming flow turbulence intensity. Filled symbols are in uniform incoming flows, and empty symbols are the sheared cases.

fluctuations, which would in turn have implications for the turbine lifetime.

It is of note that at $u'/U = 3.2\%$, case 0L has near-identical distributions of all the wake turbulence statistics analyzed as the reference case, suggesting that this level of turbulence intensity is not sufficient to significantly impact the turbulence properties in the wake. The only place it appears to have had an impact is to increase the fluctuations in the power output of the rotor.

6. Conclusions

This study investigated the independent effects of incoming shear and turbulence intensity on the near-field wake of a lab-scale wind turbine. A total of seven different flow fields were generated using an active grid. This approach allowed for a larger range of incoming flow conditions to be assessed than previously achievable with conventional means. The mean velocity field in the wake was examined, and it was found that the absolute velocity deficit can be linearly decomposed into a symmetric relative velocity deficit and the incoming shear profile. This shows that the mean velocity field of the near-wake region of a wind turbine is relatively robust to different types of incoming flow, and highlights a universality of the turbine wake when the incoming flow is removed. This has the implication that the mean wake can be estimated based on uniform flow, and a non-uniform incoming condition can be simply superimposed later. A similar idea was proposed by Chamorro & Porté-Agel [32], but has been assessed and confirmed in a wider range of incoming flow conditions here.

The hub velocity contour line was found to be biased toward the high velocity side of a shear flow. Increasing the shear forced this contour line toward the hub and away from the blade tips. This was attributed to higher momentum in the high-velocity flow overcoming the local outward radial flow induced by the spinning rotor. Examination of the turbulence statistics showed that both turbulence production and vorticity were biased toward the high-velocity side in the shear flows as well. In particular, the spatial distribution of the production and vorticity were highly dependent on the profile of the incoming flow, while the incoming turbulence intensity dominated the magnitude of the production. These phenomena in turn led to higher velocity fluctuations on the high-velocity side of sheared cases. Interestingly, the surrogate power measurements of the present study illustrated that the mean power did not change substantially for the various test cases investigated. However, the power fluctuations appear to have an approximately linear dependence on the incoming turbulence intensity, regardless of the degree of shear. This has repercussions for the lifetime of turbine, suggestion that increased turbulence will reduce total lifetime. It should also be noted that for a uniform flow with incoming turbulence intensity less than 3.2%, the wake properties are nearly-identical to those from the reference quasi-laminar incoming flow.

The experimental setup of this study permitted investigations of the wake up to $x/D = 2$. Future studies should investigate the medium- to far-field of the wake in order to better understand its development and the consequent impact on turbines located downstream. In particular, measurements farther downstream could allow for the development of a new wake model that incorporates the effects of shear and turbulence intensity presented herein. It should also be noted that in a real-world scenario, the rotor wake also interacts with the wake from the tower, causing the centre of the vortex core to be deflected downward towards the ground, leading to asymmetry in the wake geometry [34]; this phenomenon is absent from the present study as a result of the low drag sting used to hold the turbine in the centre of the flow, and would be an interesting topic for future investigations. Finally, this study has been presented as a proof-of-concept for the approach of placing a model wind turbine downstream of an active grid that can produce a wide range of turbulent shear flows. It was demonstrated that the shear and turbulence intensity of the incoming conditions could be changed in a controllable way, and that these changes had an impact on the power and wake of the model turbine. Future studies should apply similar methodology to larger scale models that can more closely match the operating conditions and geometries of full-scale wind turbines. Such facilities already exist in several larger scale labs around the world.

Declaration of competing interest

The authors declare that they have no known competing financial interests or personal relationships that could have appeared to influence the work reported in this paper.

Acknowledgements

The authors gratefully acknowledge the financial support of the EPSRC and NSERC.

The authors declare that they have no conflicts of interest that impact this study.

BG and RJH conceived of the idea for this work. MAF designed the model turbine. RJH conducted the experiments with help from MAF. LL performed the analysis and was the primary author of the manuscript with support from RJH. All authors read and contributed to the manuscript.

Preliminary results from this work were presented at the *Interdisciplinary Turbulence Initiative Conference* in Bertinoro, Italy in 2018 [35]. The present investigation covers significantly more breadth and is wholly original.

References

[1] M.S. Adaramola, P. Krogstad, Experimental investigation of wake effects on wind turbine performance, Renew. Energy 36 (2011) 2078–2086, https://doi.org/10.1016/j.renene.2011.01.024.

[2] R.J. Barthelmie, S.C. Pryor, S.T. Frandsen, K.S. Hansen, J.G. Schepers, K. Rados, W. Schlez, A. Neubert, L.E. Jensen, S. Neckelmann, Quantifying the impact of wind turbine wakes on power output at offshore wind farms, J. Atmos. Ocean. Technol. 27 (2010), https://doi.org/10.1175/2010JTECHA1398.1.

[3] M. Gaumond, P.E. Réthoré, A. Bechmann, S. Ott, G.C. Larsen, A. Peña, K.S. Hansen, Benchmarking of wind turbine wake models in large offshore wind farms, in: Proceedings of the Science of Making Torque from Wind 2012, 2012.

[4] L.J. Vermeer, J.N. Sørensen, A. Crespo, Wind turbine wake aerodynamics, Prog. Aerosp. Sci. 39 (2003) 467–510, https://doi.org/10.1016/S0376-0421(03)00078-2.

[5] F.D. Bianchi, H. de Battista, R.J. Mantz, Wind Turbine Control Systems: Principles, Modelling, and Gain Scheduling Design, Springer, 2006.

[6] R. Wagner, M. Courtney, J. Gottschall, P. Lindelöw-Marsden, Accounting for the speed shear in wind turbine power performance measurement, Wind Energy 14 (2011) 993–1004, https://doi.org/10.1002/we.509.

[7] R. Wagner, I. Antoniou, S.M. Pedersen, M.S. Courtney, H.E. Jørgensen, The influence of the wind speed profile on wind turbine performance measurements, Wind Energy 12 (2009) 348–362, https://doi.org/10.1002/we.297.

[8] N. Dimitrov, A. Natarajan, M. Kelly, Model of wind shear conditional on turbulence and its impact on wind turbine loads, Wind Energy 18 (2015) 1917–1931, https://doi.org/10.1002/we.1797.

[9] T. Mücke, D. Kleinhans, J. Peinke, Atmospheric turbulence and its influence on the alternating loads on wind turbines, Wind Energy 14 (2011) 301–316, https://doi.org/10.1002/we.422.

[10] P. Milan, M. Wächter, J. Peinke, Turbulent character of wind energy, Phys. Rev. Lett. 110 (2013), https://doi.org/10.1103/PhysRevLett.110.138701.

[11] A. Choukulkar, Y. Pichugina, C. Clark, R. Calhoun, R. Banta, A. Brewer, M. Hardesty, A new formulation for rotor equivalent wind speed for wind resource assessment and wind power forecasting, Wind Energy 19 (2016) 1439–1452, https://doi.org/10.1002/we.1929.

[12] J. Counihan, An improved method of simulating an atmospheric boundary layer in a wind tunnel, Atmos. Environ. 3 (1969) 197–214, https://doi.org/10.1016/0004-6981(69)90008-0.

[13] J. Counihan, Simulation of an adiabatic urban boundary layer in a wind tunnel, Atmos. Environ. 7 (1973) 673–689, https://doi.org/10.1016/0004-6981(73)

90150-9.
[14] C. Vanderwel, S. Tavoularis, Coherent structures in uniformly sheared turbulent flow, J. Fluid Mech. 689 (2011) 434–464, https://doi.org/10.1017/jfm.2011.423.
[15] D. Medici, P.H. Alfredsson, Measurements on a wind turbine wake: 3D effects and bluff body vortex shedding, Wind Energy 9 (2006) 219–236, https://doi.org/10.1002/we.156.
[16] Y. Hattori, M. Yamamoto, Y. Eguchi, K. Kondo, H. Suto, N. Tanaka, A Wind Tunnel Experiment on Wake Structure of a Wind Turbine, KAJIM Technical Research Institute, Kajim, 2007, https://doi.org/10.13140/2.1.5141.0727.
[17] H. Makita, Realization of a large-scale turbulence field in a small wind tunnel, Fluid Dyn. Res. 8 (1991) 53–64, https://doi.org/10.1016/0169-5983(91)90030-m.
[18] P. Knebel, A. Kittel, J. Peinke, Atmospheric wind field conditions generated by active grids, Exp. Fluid 51 (2011) 471–481, https://doi.org/10.1007/s00348-011-1056-8.
[19] I. Neunaber, J. Schottler, J. Peinke, M. Hölling, Comparison of the development of a wind turbine wake under different inflow conditions, in: R. Örlü, A. Talamelli, M. Oberlack, J. Peinke (Eds.), Progress in Turbulence VII, Springer International Publishing, Cham, 2017, pp. 177–182, https://doi.org/10.1007/978-3-319-57934-4_25.
[20] X. Shen, Z. Warhaft, The anisotropy of the small scale structure in high Reynolds (R_λ~1000) turbulent shear flow, Phys. Fluids 12 (2000), https://doi.org/10.1063/1.1313552.
[21] H.E. Cekli, W. van de Water, Tailoring turbulence with an active grid, Exp. Fluid 49 (2010) 409–416, https://doi.org/10.1007/s00348-009-0812-5.
[22] J. Schottler, A. Hölling, J. Peinke, M. Hölling, Brief communication: on the influence of vertical wind shear on the combined power output of two model wind turbines in yaw, Wind Energy Sci. 2 (2017) 439–442, https://doi.org/10.5194/wes-2-439-2017.
[23] S. Rockel, J. Peinke, M. Hölling, R.B. Cal, Dynamic wake development of a floating wind turbine in free pitch motion subjected to turbulent inflow generated with an active grid, Renew. Energy 112 (2017) 1–16, https://doi.org/10.1016/j.renene.2017.05.016.
[24] M. Talavera, F. Shu, Experimental study of turbulence intensity influence on wind turbine performance and wake recovery in a low-speed wind tunnel, Renew. Energy 109 (2017) 363–371, https://doi.org/10.1016/j.renene.2017.03.034.
[25] R.J. Hearst, B. Ganapathisubramani, Tailoring incoming shear and turbulence profiles for lab-scale wind turbines, Wind Energy 20 (2017) 2021–2035, https://doi.org/10.1002/we.2138.
[26] E. Dogan, R. Hanson, B. Ganapathisubramani, Interactions of large-scale free-stream turbulence with turbulent boundary layers, J. Fluid Mech. 802 (2016) 79–107, https://doi.org/10.1017/jfm.2016.435.
[27] R.J. Hearst, P. Lavoie, The effect of active grid initial conditions on high Reynolds number turbulence, Exp. Fluid 56 (2015) 1–20, https://doi.org/10.1007/s00348-015-2052-1.
[28] J. Jonkman, S. Butterfield, W. Musial, G. Scott, Definition of a 5-MW Reference Wind Turbine for Offshore System Development, Technical Report, National Renewable Energy Laboratory, 2009, https://www.nrel.gov/docs/fy09osti/38060.pdf.
[29] D.B. Araya, J.O. Dabiri, A comparison of wake measurements in motor-driven and flow-driven turbine experiments, Exp. Fluid 56 (2015), https://doi.org/10.1007/s00348-015-2022-7.
[30] F.D. Bianchi, R.J. Mantz, H.D. Battista, The Wind and Wind Turbines, Springer, 2007.
[31] S. Corrsin, Turbulence: experimental methods, in: S. Flügge, C. Truesdell (Eds.), Handbuch der Physik, Springer, 1963, pp. 524–589.
[32] L.P. Chamorro, F. Porté-Agel, A wind-tunnel investigation of wind-turbine wakes: boundary-layer turbulence effects. Bound, Layer Meteor. 132 (2009) 129–149, https://doi.org/10.1007/s10546-009-9380-8.
[33] Y. Jin, H. Liu, R. Aggarwal, A. Singh, L.P. Chamorro, Effects of freestream turbulence in a model wind turbine wake, Energies 9 (2016), https://doi.org/10.3390/en9100830.
[34] F. Pierella, L. Sætran, Wind tunnel investigation on the effect of the turbine tower on wind turbines wake symmetry, Wind Energy 20 (2017) 1753–1769, https://doi.org/10.1002/we.2120.
[35] L. Li, R. Hearst, B. Ganapathisubramani, The mean velocity of the near-field of a lab-scale wind turbine in tailored turbulent shear flows, in: R. Örlu, A. Talamelli, M. Oberlack, J. Peinke (Eds.), Progress in Turbulence VIII, Springer Proceedings in Physics, 2019, pp. 317–322, https://doi.org/10.1007/978-3-030-22196-6_50.